공학박사 학위논문

Acoustic full waveform inversion with the diffraction-angle-filtering-based nested algorithm: Application to 3D seismic data

회절각 필터링 기반 중첩 알고리듬을 사용한 음향파 완전파형역산: 3차원 탄성파 자료에서의 적용

2023년 2월

서울대학교 대학원
에너지시스템공학부
김 동 건

Acoustic full waveform inversion with the diffraction-angle-filtering-based nested algorithm: Application to 3D seismic data

회절각 필터링 기반 중첩 알고리듬을 사용한 음향파 완전파형역산: 3차원 탄성파 자료에서의 적용

지도교수 민 동 주

이 논문을 공학박사학위논문으로 제출함
2022년 11월

서울대학교 대학원
공과대학 에너지시스템공학부
김 동 건

김동건의 공학박사학위논문을 인준함
2023년 01월

위 원 장	조 용 채	(인)
부위원장	민 동 주	(인)
위 원	정 은 혜	(인)
위 원	오 주 원	(인)
위 원	신 정 균	(인)

Abstract

Acoustic full waveform inversion with the diffraction-angle-filtering-based nested algorithm: Application to 3D seismic data

Donggeon Kim
Department of Energy Systems Engineering
The Graduate School
Seoul National University

Full waveform inversion (FWI), which is a data-fitting approach that aims at building quantitative high-resolution subsurface velocity models, becomes one of the most popular tools to image wide-aperture and broadband seismic data. Considering both the kinematic and dynamic properties of all waves in seismic data makes FWI highly non-linear. However, because FWI is solved in the linearized local optimization framework, it often falls into local minima when initial models deviate from true models. To mitigate its non-linearity, one can preferentially reconstruct low-wavenumber macro velocity structures and then gradually recover higher-wavenumber reflectivity structures. However, in the early stage of conventional FWI, short-spread reflection data hardly contribute to the low-wavenumber update. Contribution of the reflection data to the update of FWI appears in the high-wavenumber reflectivity image. Therefore, contrary to the literal

meaning of “full waveform inversion”, conventional FWI mainly relies on the diving waves to recover the background velocity model, which is crucial to stably converge to the global minimum.

To additionally derive the low-wavenumber update from the reflected waves in the early stage of inversion, reflection waveform inversion (RWI) is proposed incorporating the scale separation of the velocity model into the background velocity and reflectivity models. By explicitly using the reflectivity model, the low-wavenumber update along the reflection wavepaths is available in the early stage of inversion, which are used to update the background velocity model. Once the background velocity model has been newly updated, the reflectivity model is then re-inverted from the new background velocity model. In this manner, the background velocity and reflectivity models are alternately updated.

For a large-scale practical application, the approach to separate the high- and low-wavenumber components of the velocity model should avoid a large increase in computational effort. Meanwhile, to secure wider low-wavenumber update coverage, the contribution of the diving waves to the low-wavenumber update has to be appropriately considered during inversion of the background velocity model.

In this thesis, the FWI gradient in reflection seismology is first analyzed to demonstrate how the diving and reflected waves contribute to the wavenumber components of the FWI gradient. Then, a diffraction-angle filtering technique, which has been proposed to control low-, intermediate- and high-wavenumber components of the FWI gradient in acoustic FWI, is introduced for the scale separation of the velocity model. The effects of the five modes of diffraction-angle filtering on the

FWI gradient are illustrated only to show how diffraction-angle filtering changes the contributions of the diving and reflected waves to the FWI gradient.

Based on the analysis of the FWI gradient and diffraction-angle filtering, I propose a new acoustic FWI technique with the diffraction-angle-filtering-based nested algorithm to build a reliable P-wave background velocity model using both the diving and reflected waves assuming a large-scale seismic data acquisition. In the nested algorithm, diffraction-angle filtering is applied in the framework of RWI, which allows the scale separation of the velocity model with reasonable computational efforts. Among the five modes of diffraction-angle filtering, modes IV and V are applied to the FWI gradient to update the background velocity and reflectivity structures, respectively. The prior reflectivity structures reconstructed by applying mode V provides the low-wavenumber update generated along the reflection wavepaths in addition to the conventional FWI update in the early stage of inversion. Then, mode IV can directly extract the low-wavenumber update generated along the wavepaths of the diving and reflected waves. With the improved low-wavenumber coverage, the background velocity model that accurately describes the kinematic behaviors of the observed diving and reflected waves can be reconstructed.

Applications to the synthetic data for the 3D SEG/EAGE overthrust model and real 3D ocean-bottom cable (OBC) data from the Volve field at the North sea demonstrate that the diffraction-angle-filtering-based nested algorithm builds reliable background velocity models even when the subsurface structures are highly complex, or seismic data are affected by elasticity or anisotropy, which is common

in field data applications. Modes IV and V of diffraction-angle filtering are successfully implemented for the scale separation in the framework of RWI. The background velocity models reconstructed by the nested algorithm can be used as new initial models for the subsequent acoustic or elastic FWI, which allows us to yield more accurate high-resolution subsurface velocity models.

Keyword: Inverse theory, Waveform inversion, Seismic tomography, Body waves, Acoustic properties, Wave scattering and diffraction

Student Number: 2017-21684

Contents

Figures

Tables

Algorithms

Chapter 1. Introduction

1.1. Background of the study

Full waveform inversion (FWI), which is a method of data-fitting to provide subsurface structures of physical properties, became a powerful subsurface imaging tool as the wide-aperture and broadband seismic survey techniques were introduced (Tarantola 1984; Virieux and Operto 2009). Because the computational cost for modeling of realistic wave propagation behavior is generally high, the simple acoustic approximation has commonly been used for inversion of offshore seismic survey data. In FWI, the kinematic and dynamic behaviors of the direct, diving, refracted and reflected waves are simultaneously considered with the limited acquisition geometries and frequency bandwidth. In this case, the relationship between the seismic data misfit and subsurface model is usually non-linear; but conventional FWI is solved by linearized local optimization approaches. Therefore, as discussed in the former studies (Bunks et al. 1995; Sirgue and Pratt 2004; Shen and Symes 2008; Virieux and Operto 2009), FWI is prone to fall into local minima when sufficiently accurate initial models are unavailable. To mitigate the local minima problem, one often preferentially retrieves low-wavenumber background velocity structures from the kinematic information of wide-aperture seismic data (Pratt et al. 1996; Plessix et al. 2010; Alkhalifah 2015b; Brossier et al. 2015). During the reconstruction of the background velocity, kinematic information of short-spread reflection data hardly contributes to the low-wavenumber update because the velocity update associated with the reflected waves is dominated by high-

wavenumber update in the conventional FWI (Mora 1989). Therefore, the low-wavenumber update in the early stage of conventional FWI, which plays an important role in successful applications of FWI, heavily relies on the diving waves.

In reflection seismology, the information carried by the reflected waves is essential to retrieve the structures at the deep part. One of the most robust tools for the estimation of macro velocity models from the reflected waves is migration velocity analysis (MVA). MVA is the process of the velocity model reconstruction in the image domain, which aims to maximize the coherency of the migrated image along the offset or aperture angle axis (Symes and Carazzone 1991; Sava and Fomel 2003; Sava and Biondi 2004; Symes 2008). Based on linearized acoustic modeling with the scale separation and appropriate differential semblance optimization (DSO), MVA guarantees the stable reconstruction of background velocity models. However, MVA requires more computational resources than FWI for extended imaging conditions (Sava and Vasconcelos 2011). To introduce the MVA-like low-wavenumber update from the reflected waves for the reconstruction of background velocity models in FWI, Xu et al. (2012) proposed reflection waveform inversion (RWI) on the basis of migration-based traveltime tomography (Chavent et al. 1994; Clément et al. 2001; MBTT). Similar to MBTT or MVA, RWI uses the scale separation of the velocity model. The velocity model is separated into the high-wavenumber reflectivity and low-wavenumber background models. In RWI, the reflectivity model is first inverted prior to the reconstruction of the background velocity model. By explicitly using the prior reflectivity model, the low-wavenumber update, which occurs along the reflection wavepaths, is available in the early stage

of inversion. The low-wavenumber update from the reflected waves is used to reconstruct the background velocity model. Then, the reflectivity and background velocity models are updated in an alternate way during RWI. Zhou et al. (2015) combined early-arrival waveform inversion and RWI to improve the coverage of low-wavenumber updates for the background velocity model, and Wu & Alkhalifah (2015) simultaneously inverted the reflectivity and background parts by solving a new optimization problem. The scale separation of the velocity model can be achieved by decomposing the wavefields into the incident and scattered wavefields based on the migration/demigration process or up- and down-going decomposition (Wang et al. 2013) and then defining the new formulation of the FWI gradient to exclude the high-wavenumber-related terms.

Gradient filtering can help to extract desired wavenumber components for scale separation of the velocity model update (Albertin et al. 2013; Almomin & Biondi 2013; Tang et al. 2013). Alkhalifah (2015b) proposed scattering-angle filtering based on representation of the gradient in the time-lag normalized domain, which provides low-wavenumber components guided by the scattering angle. Following Alkhalifah (2015b), Wu and Alkhalifah (2017) improved the efficiency of scattering-angle filtering by defining a simplified scattering-angle-enrichment formulation with the cosine function of the scattering angle. Yao et al. (2018) decomposed the waves into the plane waves by applying the spatial Fourier transform to design the opening angle filtering function. These scattering-angle filtering defined in the wavenumber domain requires a high-dimensional Fourier transform, which is difficult to adopt for 3D cases.

As an alternative to extract high- or low-wavenumber components of the FWI gradient by controlling the scattering energy in acoustic imaging, the inverse-scattering imaging condition (ISIC) or energy-norm imaging condition (ENIC) (Whitmore and Crawley 2012; Ramos-Martinez et al. 2016; Rocha et al. 2016) can be adopted. ISIC or ENIC works by combining the Laplacian operator and weighted temporal derivatives of the wavefields, which requires relatively less computational resources compared to filtering in the wavenumber domain. ISIC or ENIC is identical to a combination of the virtual sources (the model parameter perturbation playing a role as a source for the partial derivative wavefields) of the P-wave velocity and impedance, which attenuates either small- or large-scattering angle energy for FWI or reverse time migration (RTM). Motivated by ISIC and ENIC, Oh et al. (2021) proposed diffraction-angle filtering (DAF), which additionally controls intermediate scattering-angle energy by describing the virtual sources of the P-wave velocity and P-wave impedance in elastic FWI with the parameterization comprising the P-wave velocity, P-wave impedance and Poisson's ratio in acoustic media. Kim et al. (2022) applied diffraction-angle filtering in the RWI framework, which successfully reconstructed the background velocity model from both the diving and reflected waves for 2D seismic data.

1.2. Research objective

As mentioned in Section 1.1, the preferential update of the background velocity model using the kinematic information carried by all waves (the diving and reflected waves) mitigates the local minima problem of FWI. To build reliable background velocity models in reflection seismology, one should revisit the framework of RWI. By the scale separation of the velocity model, the background velocity model can be preferentially recovered while exploiting the additional low-wavenumber update from the reflected waves.

For a large-scale practical application, the scale separation of the velocity model should be implemented in a computationally efficient way considering the time-consuming alternate updates of the reflectivity and background velocity model in RWI. Meanwhile, the contribution of the diving waves to the low-wavenumber update is often excluded in RWI. The update from the diving waves provides the low-wavenumber coverage complementary to the update from the reflected waves. Therefore, it is advisable to appropriately consider the contribution of the diving waves to the low-wavenumber update during the reconstruction of the background velocity model.

To design an improved FWI strategy dealing with the large-scale reflection-dominated data, I focus on scattering-angle-based gradient filtering. Scattering-angle-based gradient filtering directly extracts the desired wavenumber components from the FWI gradient guided by the scattering (diffraction) angle between the source and receiver wavefields composing the formulation of FWI. Based on the relationship between the contents of the FWI gradient and scattering angle,

scattering-angle-based gradient filtering can select physically meaningful high-, intermediate- or low-wavenumber components of the FWI gradient.

Among the scattering-angle filtering methods, diffraction-angle filtering is introduced in this thesis. Diffraction-angle filtering modifies the virtual source to control the small, intermediate and large scattering-angle energy by imitating the virtual sources of the P-wave velocity and P-wave impedance in elastic FWI (Oh et al. 2021). Oh et al. (2021) designed the five modes of diffraction-angle filtering to filter out either the large scattering-angle energy for RTM or small scattering-angle energy for FWI. Extended from Oh et al. (2021), I adopt diffraction-angle filtering for the scale separation of the velocity model into the reflectivity and background velocity model like RWI. To apply diffraction-angle filtering in the framework of RWI, I first review the wavenumber characteristics of the FWI gradient in reflection seismology to demonstrate how the diving and reflected waves contribute to the wavenumber contents of the FWI gradient. Next, the FWI gradients filtered by the five modes are illustrated to investigate how diffraction-angle filtering changes the contributions of the diving and reflected waves to the FWI gradient.

In this thesis, I aim to design a new process of FWI for a large-scale practical application in reflection seismology. Based on the investigations of the FWI gradient and five modes of diffraction-angle filtering, the diffraction-angle-filtering-based scale separation is implemented. By incorporating the framework of RWI into FWI, the FWI gradient contains the low-wavenumber update from both the diving and reflected waves, which can be directly extracted by diffraction-angle filtering, in the early stage of inversion. Then, a new acoustic FWI strategy with the diffraction-

angle-filtering-based nested algorithm can be designed to build reliable background velocity model using both the diving and reflected waves. Finally, acoustic FWI with the diffraction-angle-filtering-based nested algorithm is applied to the large-scale complex 3D synthetic data and real 3D data with elasticity and anisotropy to verify the applicability of the algorithm.

1.3. Outline

In Chapter 2, I show the formulations and implementations of acoustic wave modeling and acoustic FWI for applications to 3D data. The numerical schemes to compute the acoustic wavefields and FWI gradient in 3D are described.

In Chapter 3, the contributions of the diving and reflected waves to the FWI gradient is first investigated. From the analysis of the wavenumber components of the FWI gradient from the diving and reflected waves, we can understand why the contribution of the reflected waves to the low-wavenumber update lacks in conventional FWI. Then, I introduce the formulation and mechanism of diffraction-angle filtering. The numerical scheme and computational requirements to implement diffraction-angle filtering is also explained. Next, diffraction-angle filtering is applied to the FWI gradient to see how the contributions of the diving and reflected waves to the FWI gradient can be changed.

Considering some key points of RWI, I design a new nested algorithm, which consists of the alternate updates of the reflectivity and background velocity model. Among the five modes of diffraction-angle filtering, modes IV and V is used to compute the FWI gradient for the background velocity and reflectivity model, respectively. Mode V is first applied to the FWI gradient to invert the reflectivity model from the normal-incidence reflections. By explicitly including the prior reflectivity model, the low-wavenumber update along the wavepaths of the reflected waves is additionally available. Then, Mode IV directly extracts the contributions of the diving and reflected waves to low-wavenumber update from the FWI gradient, which can be used to build reliable background velocity model with wider low-

wavenumber coverage.

In Chapter 4, a synthetic data example for the 3D SEG/EAGE overthrust model is presented to demonstrate that acoustic FWI with the diffraction-angle-filtering-based nested algorithm can provide kinematically reliable background velocity model for an ideal acoustic case, even when the subsurface structures are complex and initial velocity model deviates from the true velocity model.

Chapter 5 shows a real data example for the 3D ocean-bottom cable (OBC) data from the Volve field at the North sea to examine if the proposed algorithm for acoustic FWI can enhance the macro velocity structures in the presence of strong elasticity and anisotropy.

Chapter 2. Implementation of acoustic FWI

2.1. Acoustic wave modeling

2.1.1. Acoustic wave equation

In marine reflection seismology employing a pressure source, wave propagation is commonly described using the acoustic wave equation under the assumption of constant density. The acoustic wave equation with constant density can be derived from the equation of wave motion and generalized Hooke's law written by

$$\mathbf{a}(\mathbf{x}_s, \mathbf{x}, t) = -\nabla P(\mathbf{x}_s, \mathbf{x}, t) + \mathbf{f}(\mathbf{x}_s, t),$$
$$\frac{\partial^2 P(\mathbf{x}_s, \mathbf{x}, t)}{\partial t^2} = -V_{\mathrm{p}}(\mathbf{x})^2 (\nabla \cdot \mathbf{a}(\mathbf{x}_s, \mathbf{x}, t)) + f_P(\mathbf{x}_s, t), \quad (2\text{-}1)$$

where P and $\mathbf{a}$ are the pressure and particle acceleration vector, respectively; $\mathbf{x}$ indicates the spatial coordinates; t indicates time, and V_{p} is the P-wave velocity. The terms f_P and $\mathbf{f}$ represent the pressure and body-force sources, respectively, acting as seismic sources at the position $\mathbf{x}_s$. By combining these equations, the acoustic wave equation can be rewritten as the acoustic wave equation with the second-order derivatives of wavefields in the temporal and spatial coordinates in terms of pressure as follows:

$$\frac{\partial^2 P(\mathbf{x}_s, \mathbf{x}, t)}{\partial t^2} = V_{\mathrm{p}}(\mathbf{x})^2 \nabla^2 P(\mathbf{x}_s, \mathbf{x}, t) + f_P(\mathbf{x}_s, t), \quad (2\text{-}2)$$

or in terms of particle displacement vector as follows:

$$\mathbf{a}(\mathbf{x}_s, \mathbf{x}, t) = \nabla\left[V_p(\mathbf{x})^2(\nabla \cdot \mathbf{u}(\mathbf{x}_s, \mathbf{x}, t))\right] + \mathbf{f}(\mathbf{x}_s, t), \tag{2-3}$$

where $\mathbf{u}$ is the particle displacement vector. The acoustic wave equation can be solved by numerical simulation for a given P-wave velocity model using the staggered-grid finite-difference method (SGFDM) (Virieux 1984; Grave 1996), which will be described in Section 2.1.2.

2.1.2. Staggered-grid finite-difference method

In this thesis, to describe the acoustic wave behavior, equation (2-1) is solved by the high-order SGFDM, which discretizes derivatives of wavefields using centered finite-differences. The finite-difference method (FDM) has been widely adopted to solve a variety of physical problems governed by partial differential equations. The finite-element method (FEM; Marfurt 1984) or spectral-element method (SEM; Komatitsch and Tromp 1999), which can provide stable solutions for complex 3D models even with irregular free-surface topography, can also be used to solve the acoustic wave equation. However, marine seismic survey data are free from the effect of irregular free-surface topography and the FDM can provide accurate numerical solutions with lower computational cost compared to other methods.

The stability and accuracy of FDM are generally enhanced by adopting high-order staggered-grid method (Moczo et al. 2000). The high-order SGFDM uses a more complex operator to solve the first-order derivatives of wavefields in the spatial

coordinates but requires fewer grid points to simulate the acoustic wave propagation without numerical dispersion. By considering the dimension of subsurface models and the frequency band of interest, the fourth-order SGFDM is used in this thesis. Discretization of equation (2-1) leads to a staggered-grid, as shown in Fig. 2.1. Then, the numerical scheme is as follows:

$$\mathrm{a}_x(\mathbf{x}_s, \mathbf{x}_{i+1/2,j,k}, t_n) = -\frac{1}{\Delta x}\left[\frac{9}{8}(P(\mathbf{x}_s, \mathbf{x}_{i+1,j,k}, t_n) - P(\mathbf{x}_s, \mathbf{x}_{i,j,k}, t_n)) - \frac{1}{24}(P(\mathbf{x}_s, \mathbf{x}_{i+2,j,k}, t_n) - P(\mathbf{x}_s, \mathbf{x}_{i-1,j,k}, t_n))\right],$$

$$\mathrm{a}_y(\mathbf{x}_s, \mathbf{x}_{i,j+1/2,k}, t_n) = -\frac{1}{\Delta y}\left[\frac{9}{8}(P(\mathbf{x}_s, \mathbf{x}_{i,j+1,k}, t_n) - P(\mathbf{x}_s, \mathbf{x}_{i,j,k}, t_n)) - \frac{1}{24}(P(\mathbf{x}_s, \mathbf{x}_{i,j+2,k}, t_n) - P(\mathbf{x}_s, \mathbf{x}_{i,j-1,k}, t_n))\right],$$

$$\mathrm{a}_z(\mathbf{x}_s, \mathbf{x}_{i,j,k+1/2}, t_n) = -\frac{1}{\Delta z}\left[\frac{9}{8}(P(\mathbf{x}_s, \mathbf{x}_{i,j,k+1}, t_n) - P(\mathbf{x}_s, \mathbf{x}_{i,j,k}, t_n)) - \frac{1}{24}(P(\mathbf{x}_s, \mathbf{x}_{i,j,k+2}, t_n) - P(\mathbf{x}_s, \mathbf{x}_{i,j,k-1}, t_n))\right],$$

$$\begin{aligned} P(\mathbf{x}_s, \mathbf{x}_{i,j,k}, t_{n+1}) = {} & 2P(\mathbf{x}_s, \mathbf{x}_{i,j,k}, t_n) - P(\mathbf{x}_s, \mathbf{x}_{i,j,k}, t_{n-1}) \\ & - \frac{\Delta t^2}{\Delta x} V_{\mathrm{p}}(\mathbf{x}_{i,j,k})^2 \left[\frac{9}{8}(\mathrm{a}_x(\mathbf{x}_s, \mathbf{x}_{i+1/2,j,k}, t_n) - \mathrm{a}_x(\mathbf{x}_s, \mathbf{x}_{i-1/2,j,k}, t_n)) \right. \\ & \left. - \frac{1}{24}(\mathrm{a}_x(\mathbf{x}_s, \mathbf{x}_{i+3/2,j,k}, t_n) - \mathrm{a}_x(\mathbf{x}_s, \mathbf{x}_{i-3/2,j,k}, t_n))\right] \\ & - \frac{\Delta t^2}{\Delta y} V_{\mathrm{p}}(\mathbf{x}_{i,j,k})^2 \left[\frac{9}{8}(\mathrm{a}_y(\mathbf{x}_s, \mathbf{x}_{i,j+1/2,k}, t_n) - \mathrm{a}_y(\mathbf{x}_s, \mathbf{x}_{i,j-1/2,k}, t_n)) \right. \\ & \left. - \frac{1}{24}(\mathrm{a}_y(\mathbf{x}_s, \mathbf{x}_{i,j+3/2,k}, t_n) - \mathrm{a}_y(\mathbf{x}_s, \mathbf{x}_{i,j-3/2,k}, t_n))\right] \\ & - \frac{\Delta t^2}{\Delta z} V_{\mathrm{p}}(\mathbf{x}_{i,j,k})^2 \left[\frac{9}{8}(\mathrm{a}_z(\mathbf{x}_s, \mathbf{x}_{i,j,k+1/2}, t_n) - \mathrm{a}_z(\mathbf{x}_s, \mathbf{x}_{i,j,k-1/2}, t_n)) \right. \\ & \left. - \frac{1}{24}(\mathrm{a}_z(\mathbf{x}_s, \mathbf{x}_{i,j,k+3/2}, t_n) - \mathrm{a}_z(\mathbf{x}_s, \mathbf{x}_{i,j,k-3/2}, t_n))\right], \end{aligned} \tag{2-4}$$

where i, j, k and n are the indices for x-axis, y-axis, z-axis and time discretization, respectively; Δx, Δy, Δz are the grid steps for the x-axis, y-axis, z-axis, respectively; and Δt is the grid step in time. Note that the first-order derivatives in the spatial coordinates are approximated by a centralized fourth-order scheme, which is derived from the linear combination of different Taylor expansions (Fornberg 1988), and the first-order derivative in time is approximated by a second-order scheme.

2.1.3. Boundaries

In general, the acoustic wave equation does not require additional explicit boundary conditions, because internal interfaces and acoustic sources are represented by changes of the P-wave velocity and the source terms in equation (2-1), respectively. To describe acoustic wave propagation in an inhomogeneous half-space, stress-free conditions (by setting the pressure field to zero on the boundary for acoustic cases) are implemented for the upper boundary, which represent the free-surface boundary conditions and absorbing boundary conditions are implemented for five other boundaries to remove artificial reflections occurring at the outer boundaries of the computational grid. In this thesis, the perfectly matched layer (PML; Berenger 1994; Collino and Tsogka 2001) is used to suppress these artificial reflections.

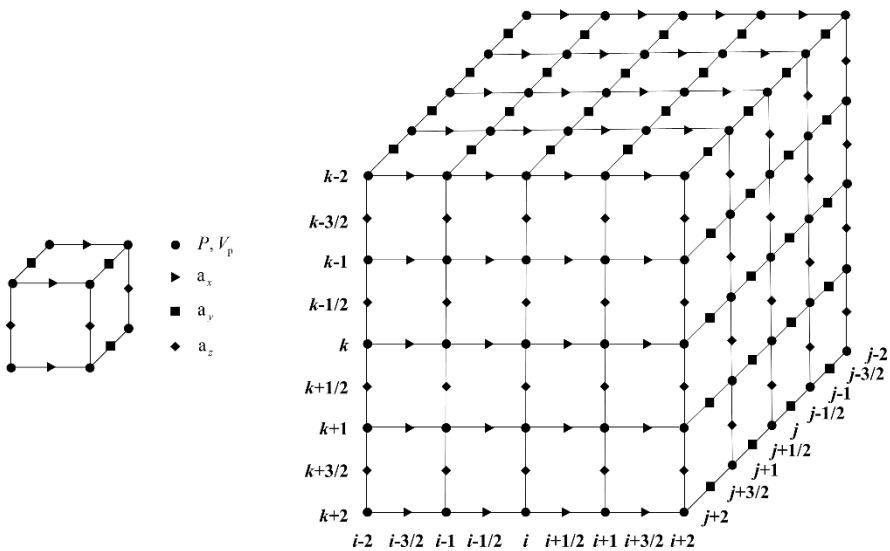

Fig. 2.1. Discretization of the acoustic wave equation on a 3D staggered grid set. The black circles are for pressures and velocities. The black triangles, squares and diamonds are for particle accelerations in x, y and z directions, respectively. Note that pressure and particle accelerations are defined at the same time step.

PML introduces the stretched-coordinate space in the frequency domain expressed by

$$x = x - \frac{i}{\omega}\int_0^x d_x(s)\,ds\,,$$

$$y = y - \frac{i}{\omega}\int_0^y d_y(s)\,ds\,,$$

$$\tilde{z} = z - \frac{i}{\omega}\int_0^z d_z(s)\,ds\,, \tag{2-5}$$

where x, y and $\tilde{z}$ are the new space variables stretched into the complex domain; ω is the angular frequency and d_x, d_y and d_z are the damping profiles that gradually increase toward the outer boundaries of the computational grid in the PML regions (Fig. 2.2). Assuming a plane wave propagation along the x-axis with the new space variable,

$$A\exp(-i(k_x x - \omega t)) = A\exp(-i(k_x x - \omega t))\exp(-\frac{k_x}{\omega}\int_0^x d_x(s)\,ds)\,, \tag{2-6}$$

it is noticed that a wave becomes attenuative in the stretched-coordinate space. To implement the PML, the spatial derivatives are changed as:

$$\frac{\partial}{\partial x} = \frac{i\omega}{i\omega + d_x}\frac{\partial}{\partial x} = \frac{1}{s_x}\frac{\partial}{\partial x}\,,$$

$$\frac{\partial}{\partial y} = \frac{i\omega}{i\omega + d_y}\frac{\partial}{\partial y} = \frac{1}{s_y}\frac{\partial}{\partial y}\,,$$

$$\frac{\partial}{\partial \tilde{z}} = \frac{i\omega}{i\omega + d_z}\frac{\partial}{\partial z} = \frac{1}{s_z}\frac{\partial}{\partial z}\,. \tag{2-7}$$

In the time domain, the spatial derivatives of the wavefield P following equation (2-7) are rewritten as follows:

$$\begin{aligned}
\frac{\partial P(\mathbf{x},t_n)}{\partial x} &= F^{-1}\left(\frac{1}{s_x}\right) * \frac{\partial P(\mathbf{x},t_n)}{\partial x} = \frac{\partial P(\mathbf{x},t_n)}{\partial x} - d_x H(t)\exp(-d_x t) * \frac{\partial P(\mathbf{x},t_n)}{\partial x} \\
&= \frac{\partial P(\mathbf{x},t_n)}{\partial x} + \varphi_x(\mathbf{x},t_n)
\end{aligned},$$

$$\begin{aligned}
\frac{\partial P(\mathbf{x},t_n)}{\partial y} &= F^{-1}\left(\frac{1}{s_y}\right) * \frac{\partial P(\mathbf{x},t_n)}{\partial y} = \frac{\partial P(\mathbf{x},t_n)}{\partial y} - d_y H(t)\exp(-d_y t) * \frac{\partial P(\mathbf{x},t_n)}{\partial y} \\
&= \frac{\partial P(\mathbf{x},t_n)}{\partial y} + \varphi_y(\mathbf{x},t_n)
\end{aligned},$$

$$\begin{aligned}
\frac{\partial P(\mathbf{x},t_n)}{\partial \tilde{z}} &= F^{-1}\left(\frac{1}{s_z}\right) * \frac{\partial P(\mathbf{x},t_n)}{\partial z} = \frac{\partial P(\mathbf{x},t_n)}{\partial z} - d_z H(t)\exp(-d_z t) * \frac{\partial P(\mathbf{x},t_n)}{\partial z} \\
&= \frac{\partial P(\mathbf{x},t_n)}{\partial z} + \varphi_z(\mathbf{x},t_n)
\end{aligned}, \quad (2\text{-}8)$$

where H is the Heaviside unit step function and * represents the convolution operator in time. Then, there are recursive relationships for φ_x, φ_y and φ_z (Komatitsch and Martin 2007) to compute the spatial derivatives of the wavefield P as:

$$\begin{aligned}
\varphi_x(\mathbf{x},t_n) &= \exp(-d_x\Delta t)\varphi_x(\mathbf{x},t_{n-1}) + (\exp(-d_x\Delta t)-1)\frac{\partial P(\mathbf{x},t_n)}{\partial x}, \\
\varphi_y(\mathbf{x},t_n) &= \exp(-d_y\Delta t)\varphi_y(\mathbf{x},t_{n-1}) + (\exp(-d_y\Delta t)-1)\frac{\partial P(\mathbf{x},t_n)}{\partial y}, \\
\varphi_z(\mathbf{x},t_n) &= \exp(-d_z\Delta t)\varphi_z(\mathbf{x},t_{n-1}) + (\exp(-d_z\Delta t)-1)\frac{\partial P(\mathbf{x},t_n)}{\partial z}. \qquad (2\text{-}9)
\end{aligned}$$

The convolutional perfectly matched layer (CPML) can be easily implemented with SGFDM by introducing memory variables for φ_x, φ_y and φ_z to be updated by

equation (2-9) at each time step.

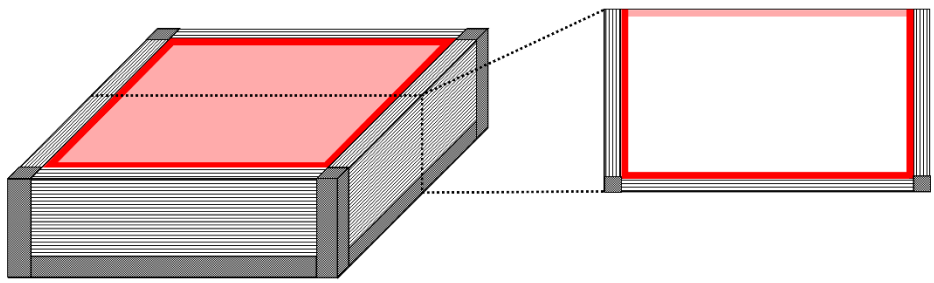

Fig. 2.2. A schematic diagram illustrating the modeling and PML regions. The area with the black solid lines indicates the PML region where damping profiles d_x, d_y and d_z gradually increase toward the outer boundaries of the computational grid. The red area denotes the boundaries of the modeling region (the white area), which will be saved and injected during boundary saving.

2.2. Acoustic FWI

2.2.1. Formulation of acoustic FWI

In the time domain, conventional acoustic FWI using the least-squares-norm-based local optimization minimizes the following objective function:

$$E(V_{\mathrm{p}}(\mathbf{x})) = \sum_{s}\sum_{r}\sum_{t}\frac{1}{2}\left[P^{c}(\mathbf{x}_{s}, \mathbf{x}_{r}, t, V_{\mathrm{p}}(\mathbf{x})) - P^{o}(\mathbf{x}_{s}, \mathbf{x}_{r}, t)\right]^{2}, \qquad (2\text{-}10)$$

where P^{c} and P^{o} are the numerically computed and observed pressure data, respectively; and s, r and t denote the source, receiver and time, respectively. The computed pressure data P^{c} are numerically obtained by SGFDM satisfying equation (2-4). Then, the gradient with respect to the P-wave velocity at the nodal point (i, j, k) for acoustic FWI can be directly expressed by the zero-lag cross-correlations between the partial derivative wavefield and the pressure data residual as follows:

$$\frac{\partial E(V_{\mathrm{p}}(\mathbf{x}))}{\partial V_{\mathrm{p}}(\mathbf{x}_{i,j,k})} = \sum_{s}\sum_{r}\sum_{t}\left[\frac{\partial P^{c}(\mathbf{x}_{s}, \mathbf{x}_{r}, t, V_{\mathrm{p}}(\mathbf{x}))}{\partial V_{\mathrm{p}}(\mathbf{x}_{i,j,k})} \cdot (P^{c}(\mathbf{x}_{s}, \mathbf{x}_{r}, t, V_{\mathrm{p}}(\mathbf{x})) - P^{o}(\mathbf{x}_{s}, \mathbf{x}_{r}, t))\right]. \qquad (2\text{-}11)$$

The partial derivative pressure wavefield with respect to V_{p} at the nodal point (i, j, k) can be computed by solving equation (2-2) with the source term substituted by the virtual pressure source $f^{v}_{s,i,j,k}$ (Pratt et al. 1998), which can be derived by

differentiating equation (2-2) with respect to V_{p} at the nodal point (i, j, k). To avoid the direct computation of the partial derivative wavefields for the P-wave velocities at all the nodal points, which requires high computational efforts, the gradient is computed using the adjoint-state method (Plessix 2006) as follows (refer to Appendix A):

$$\frac{\partial E(V_{\mathrm{p}}(\mathbf{x}))}{\partial V_{\mathrm{p}}(\mathbf{x}_{i,j,k})} = \sum_{s}\sum_{r}\sum_{t}\left[f^{v}_{s,i,j,k}(\mathbf{x}_{i,j,k}, t, V_{\mathrm{p}}(\mathbf{x})) \cdot P^{b}_{s}(\mathbf{x}_{r}, \mathbf{x}_{i,j,k}, T-t, V_{\mathrm{p}}(\mathbf{x}))\right],$$

where

$$f^{v}_{s,i,j,k}(\mathbf{x}_{i,j,k}, t, V_{\mathrm{p}}(\mathbf{x})) = 2V_{\mathrm{p}}(\mathbf{x}_{i,j,k})\nabla^{2}P(\mathbf{x}_{s}, \mathbf{x}_{i,j,k}, t, V_{\mathrm{p}}(\mathbf{x})) \quad . \qquad (2\text{-}12)$$

P^{b}_{s} indicates the adjoint pressure wavefield computed by back-propagating the pressure data residuals between P^{c} and P^{o}. Then, the gradient is computed by the zero-lag cross-correlation between the source (P) and receiver (P^{b}_{s}) wavefields.

The gradient can be reformulated in terms of the virtual body-force source and the back-propagated adjoint particle acceleration wavefield. By taking the partial derivatives of equation (2-1) with respect to V_{p} at the nodal point (i, j, k) and assuming the equivalent body-force source instead of the pressure source, the partial derivative pressure wavefield can be expressed by

$$\frac{\partial \mathbf{a}^{c}(\mathbf{x}_{s}, \mathbf{x}, t, V_{\mathrm{p}}(\mathbf{x}))}{\partial V_{\mathrm{p}}(\mathbf{x}_{i,j,k})} = -\nabla\left(\frac{\partial P^{c}(\mathbf{x}_{s}, \mathbf{x}, t, V_{\mathrm{p}}(\mathbf{x}))}{\partial V_{\mathrm{p}}(\mathbf{x}_{i,j,k})}\right) + \mathbf{f}^{v}_{s,i,j,k}(\mathbf{x}_{i,j,k}, t, V_{\mathrm{p}}(\mathbf{x})),$$

$$\frac{\partial^{2}}{\partial t^{2}}\left(\frac{\partial P^{c}(\mathbf{x}_{s}, \mathbf{x}, t, V_{\mathrm{p}}(\mathbf{x}))}{\partial V_{\mathrm{p}}(\mathbf{x}_{i,j,k})}\right) = -V_{p}(\mathbf{x})^{2}\left(\nabla\cdot\left(\frac{\partial \mathbf{a}^{c}(\mathbf{x}_{s}, \mathbf{x}, t, V_{\mathrm{p}}(\mathbf{x}))}{\partial V_{\mathrm{p}}(\mathbf{x}_{i,j,k})}\right)\right). \qquad (2\text{-}13)$$

Combining these equations, the acoustic wave equation for the partial derivative pressure wavefield with the equivalent virtual body-force source is obtained in second-order derivative form as follows:

$$\frac{\partial^2}{\partial t^2}\left(\frac{\partial P^c(\mathbf{x}_s,\,\mathbf{x},\,t,\,V_{\mathrm{p}}(\mathbf{x}))}{\partial V_{\mathrm{p}}(\mathbf{x}_{i,j,k})}\right)=V_p(\mathbf{x})^2\nabla^2\left(\frac{\partial P^c(\mathbf{x}_s,\,\mathbf{x},\,t,\,V_{\mathrm{p}}(\mathbf{x}))}{\partial V_{\mathrm{p}}(\mathbf{x}_{i,j,k})}\right),$$
$$+\,f^{v}_{s,i,j,k}(\mathbf{x}_{i,j,k},\,t,\,V_{\mathrm{p}}(\mathbf{x}))$$

where

$$f^{v}_{s,i,j,k}(\mathbf{x}_{i,j,k},\,t,\,V_{\mathrm{p}}(\mathbf{x}))=-V_{\mathrm{p}}(\mathbf{x})^2\nabla\cdot\mathbf{f}^{v}_{s,i,j,k}(\mathbf{x}_{i,j,k},\,t,\,V_{\mathrm{p}}(\mathbf{x})),$$

and

$$\mathbf{f}^{v}_{s,i,j,k}(\mathbf{x}_{i,j,k},\,t,\,V_{\mathrm{p}}(\mathbf{x}))=\nabla\left[2V_{\mathrm{p}}(\mathbf{x}_{i,j,k})\nabla\cdot\mathbf{u}(\mathbf{x}_s,\,\mathbf{x}_{i,j,k},\,t,\,V_{\mathrm{p}}(\mathbf{x}))\right]. \qquad (2\text{-}14)$$

The virtual body-force source of equation (2-14) can be computed by differentiating equation (2-3) with respect to V_{p} at the nodal point (i, j, k) following the definition of the virtual source given by Pratt et al. (1998). Based on the adjoint method and equation (2-14), the gradient of equation (2-12) can be rewritten by

$$\frac{\partial E(V_{\mathrm{p}}(\mathbf{x}))}{\partial V_{\mathrm{p}}(\mathbf{x}_{i,j,k})}=\sum_s\sum_r\sum_t\left[\mathbf{f}^{v}_{s,i,j,k}(\mathbf{x}_{i,j,k},\,t,\,V_{\mathrm{p}}(\mathbf{x}))\cdot\mathbf{a}^{b}_{s}(\mathbf{x}_r,\,\mathbf{x}_{i,j,k},\,T-t,\,V_{\mathrm{p}}(\mathbf{x}))\right],$$

where

$$\mathbf{a}^{b}_{s}(\mathbf{x}_r,\,\mathbf{x},\,T-t,\,V_p(\mathbf{x}))=V_p(\mathbf{x})^2\nabla P^{b}_{s}(\mathbf{x}_r,\,\mathbf{x},\,T-t,\,V_p(\mathbf{x})). \qquad (2\text{-}15)$$

Note that the adjoint of divergence is the negative gradient (Oh et al. 2021). The particle acceleration wavefield can be numerically obtained by using the simple finite-difference formulae (equation 2-4). Oh et al. (2021) modified the virtual source for acoustic FWI to imitate the PP diffraction patterns of the P-wave velocity and P-wave impedance in elastic FWI with the V_{p}-I_{p}-σ parameterization, where V_{p},

I_p and σ are the P-wave velocity, P-wave impedance and Poisson's ratio, respectively (Oh and Min 2017). The details will be discussed in Section 3.2.

2.2.2. Other techniques for acoustic FWI

In this section, some techniques to improve the efficiency and quality of inversion for 3D data are described. Two-level message passing interface-based parallelization, boundary saving, gradient preconditioning and source estimation are explained in Sections 2.2.2.1 to 2.2.2.4, respectively.

2.2.2.1. Two-level message passing interface-based parallelization

3D acoustic FWI implementation has no choice but to rely on two-level message passing interface-based parallelization to solve large-scale problem to avoid the enormous storage requirements or computational load per core (Bohlen 2002; Trinh et al. 2019). In the inner level, the model is subdivided into sub-models along each spatial direction. Each sub-model is assigned to an individual processor, and the wavefields for each sub-model are computed simultaneously on each assigned processor. To compute the spatial derivatives adjacent to the sub-model boundaries, the layers including the wavefield values at the boundaries are exchanged by processor-to-processor communication via message passing interface (Fig. 2.3). The depth of these layers depends on the order of the finite-difference method used. In the case of the fourth-order SGFDM, the depth of the layers is two grid points. In the

outer level, the wavefields from different seismic shots are computed parallelly. In this level, processor-to-processor communication only involves the summation of the objective functions and gradients from each seismic shot. The computational cost of communication between processors is negligible compared with that of the wavefield computation on each processor.

2.2.2.2. Boundary saving

For 3D acoustic FWI in the time domain, the source and receiver wavefields should be available at the same time step to compute the gradient (equations 2-12 or 2-15). In equations (2-12) or (2-15), unlike the source wavefield computed in the forward time order, the receiver wavefield should be computed in the reverse time order. The source wavefield at time step t_n can be re-computed from time step 0 for each receiver wavefield at time step $t_N - t_n$ (where $n = 0,1,...,N$), or stored from time step 0 to t_N. However, these approaches require extremely high computational cost or extensive storage, therefore they are not suitable for large-scale 3D FWI. Another approach is boundary saving, which uses the reversibility property of the wave equation. Boundary saving computes the source wavefield backwards in time. The source wavefield at time step t_N and t_{N-1} will be the initial condition. Then, the numerical scheme for source wavefield is as follows:

$$\mathrm{a}_x(\mathbf{x}_s, \mathbf{x}_{i+1/2,j,k}, t_n) = -\frac{1}{\Delta x}\left[\frac{9}{8}(P(\mathbf{x}_s, \mathbf{x}_{i+1,j,k}, t_n) - P(\mathbf{x}_s, \mathbf{x}_{i,j,k}, t_n)) - \frac{1}{24}(P(\mathbf{x}_s, \mathbf{x}_{i+2,j,k}, t_n) - P(\mathbf{x}_s, \mathbf{x}_{i-1,j,k}, t_n))\right],$$

$$\mathrm{a}_y(\mathbf{x}_s, \mathbf{x}_{i,j+1/2,k}, t_n) = -\frac{1}{\Delta y}\left[\frac{9}{8}(P(\mathbf{x}_s, \mathbf{x}_{i,j+1,k}, t_n) - P(\mathbf{x}_s, \mathbf{x}_{i,j,k}, t_n)) - \frac{1}{24}(P(\mathbf{x}_s, \mathbf{x}_{i,j+2,k}, t_n) - P(\mathbf{x}_s, \mathbf{x}_{i,j-1,k}, t_n))\right],$$

$$\mathrm{a}_z(\mathbf{x}_s, \mathbf{x}_{i,j,k+1/2}, t_n) = -\frac{1}{\Delta z}\left[\frac{9}{8}(P(\mathbf{x}_s, \mathbf{x}_{i,j,k+1}, t_n) - P(\mathbf{x}_s, \mathbf{x}_{i,j,k}, t_n)) - \frac{1}{24}(P(\mathbf{x}_s, \mathbf{x}_{i,j,k+2}, t_n) - P(\mathbf{x}_s, \mathbf{x}_{i,j,k-1}, t_n))\right],$$

$$\begin{aligned} P(\mathbf{x}_s, \mathbf{x}_{i,j,k}, t_{n-1}) = {} & 2P(\mathbf{x}_s, \mathbf{x}_{i,j,k}, t_n) - P(\mathbf{x}_s, \mathbf{x}_{i,j,k}, t_{n+1}) \\ & - \frac{\Delta t^2}{\Delta x} V_{\mathrm{p}}(\mathbf{x}_{i,j,k})^2 \left[\frac{9}{8}(\mathrm{a}_x(\mathbf{x}_s, \mathbf{x}_{i+1/2,j,k}, t_n) - \mathrm{a}_x(\mathbf{x}_s, \mathbf{x}_{i-1/2,j,k}, t_n)) \right. \\ & \left. - \frac{1}{24}(\mathrm{a}_x(\mathbf{x}_s, \mathbf{x}_{i+3/2,j,k}, t_n) - \mathrm{a}_x(\mathbf{x}_s, \mathbf{x}_{i-3/2,j,k}, t_n))\right] \\ & - \frac{\Delta t^2}{\Delta y} V_{\mathrm{p}}(\mathbf{x}_{i,j,k})^2 \left[\frac{9}{8}(\mathrm{a}_y(\mathbf{x}_s, \mathbf{x}_{i,j+1/2,k}, t_n) - \mathrm{a}_y(\mathbf{x}_s, \mathbf{x}_{i,j-1/2,k}, t_n)) \right. \\ & \left. - \frac{1}{24}(\mathrm{a}_y(\mathbf{x}_s, \mathbf{x}_{i,j+3/2,k}, t_n) - \mathrm{a}_y(\mathbf{x}_s, \mathbf{x}_{i,j-3/2,k}, t_n))\right] \\ & - \frac{\Delta t^2}{\Delta z} V_{\mathrm{p}}(\mathbf{x}_{i,j,k})^2 \left[\frac{9}{8}(\mathrm{a}_z(\mathbf{x}_s, \mathbf{x}_{i,j,k+1/2}, t_n) - \mathrm{a}_z(\mathbf{x}_s, \mathbf{x}_{i,j,k-1/2}, t_n)) \right. \\ & \left. - \frac{1}{24}(\mathrm{a}_z(\mathbf{x}_s, \mathbf{x}_{i,j,k+3/2}, t_n) - \mathrm{a}_z(\mathbf{x}_s, \mathbf{x}_{i,j,k-3/2}, t_n))\right] \end{aligned} \quad .(2\text{-}16)$$

In this case, the source wavefield at time step t_{n-1} is computed from the source wavefield at time step t_n and t_{n+1} during the back-propagation of the receiver wavefield. Note that this reversibility property is not valid in the case that a dissipative mechanism is applied (for example, application of PML) to simulate wave propagation in unbounded media. To circumvent this problem, the layers including the wavefield values at all time steps just inside the dissipative region should be stored (Fig. 2.2). Note that the depth of the layers depends on the order of finite-difference method. In the case of the fourth-order SGFDM, the depth of the layers is two grid points.

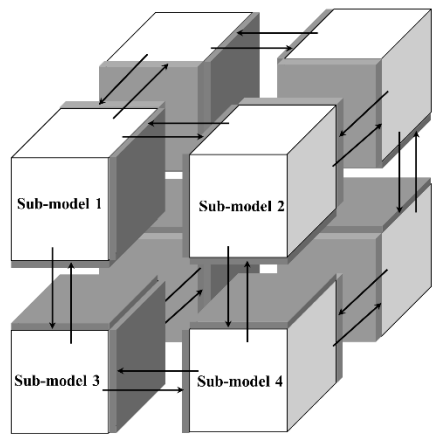

Fig. 2.3. A schematic diagram illustrating the model subdivided into sub-model along each spatial direction. The black arrows indicate communication between processors which is performed in the end of each time step. The grey layers, which include the wavefield values adjacent to the surrounding sub-models, are exchanged by processor-to-processor communication.

Saving the wavefield values at the boundaries, instead of saving the whole wavefield values, can considerably reduce the storage requirement for large-scale 3D FWI problem (Dussaud et al. 2008).

2.2.2.3. Gradient preconditioning

As FWI generally relies on the least-squares-norm-based local optimization technique, the estimation of inverse Hessian can significantly enhance the convergence of FWI. The Gauss-Newton, or Quasi-Newton methods are widely used for FWI, but the preconditioned steepest-descent method is applied in this thesis to directly examine the contribution of diffraction-angle filtering of the gradient. During FWI, the gradient is first preconditioned by the pseudo-hessian matrix (Shin et al. 2001), which can compensate for amplitude loss of the gradient at deep parts caused by the geometrical spreading effect. Still, FWI suffers from non-linearity and ill-posedness because of artifacts caused by too-coarse grids for the seismic structure update, too-few shots/receivers or noise in the recorded data. To mitigate these artifacts, a preconditioning strategy, which can be easily implemented without computation of a derivative stencil, is additionally applied to enforce smoothness (Guitton et al. 2012; Wellington et al. 2019). The preconditioning strategy can be implemented by simply multiplying a preconditioning operator to the gradient. In this thesis, 3D Gaussian filter is used as the preconditioning operator to attenuate high-wavenumber artifacts.

2.2.2.4. Source estimation

Robust source estimation is crucial for FWI so as to ensure that the data residual is only dependent on the subsurface model parameters. Source estimation can be performed by using only the direct waves at near offsets (Wellington et al. 2015), stacking the direct waves at common-offset gathers (Huang and Schuster 2018) or solving the inverse problem with respect to the source wavelet (Jeong et al. 2017; Thiel et al. 2019). In this thesis, the direct waves are used for source estimation. All shot gathers from observed and computed data are time-shifted to align the direct waves and then stack the traces at near offsets so that direct wave is constructively stacked and other waves are canceled out. By taking the stacked traces from observed and computed data as the input and output, the Wiener filter can be designed to estimate the true source wavelet from an initial guess of source wavelet.

Chapter 3. Acoustic FWI with the diffraction-angle-filtering-based nested algorithm

FWI tries to retrieve subsurface velocity structures from the information carried by the diving and reflected waves. As mentioned in Section 1.1, in the early stage of FWI, the diving waves mainly contribute to the low-wavenumber update, while the contribution of the reflected waves to the update consists of the high-wavenumber components. The maximum penetration depth of the diving waves is about a 1/5~1/3 of the maximum offset (Zhou et al. 2015; Yao et al. 2020), therefore it is often difficult to recover macro structures of deep target areas.

To examine how the diving and reflected waves contribute to the high- and low-wavenumber components of the FWI gradient, I first review the wavenumber characteristics of the FWI gradient in reflection seismology. The analysis of the wavenumber characteristics of the FWI gradient demonstrate why the low-wavenumber update from the reflected waves lacks in the early stage of FWI and how the explicit use of the prior reflectivity model derives the low-wavenumber update along the wavepaths of the reflected waves.

Then, diffraction-angle filtering is introduced to control the wavenumber contents of the FWI gradient guided by the diffraction (scattering) angle. From the illustration of the FWI gradient filtered by the five modes of diffraction-angle filtering, I can pick modes IV and V of diffraction-angle filtering for the scale separation of the velocity model.

Based on the analysis, I design a new process of FWI for the reflection data by

incorporating the framework of RWI into FWI with diffraction-angle filtering. Like RWI (Xu et al. 2012; Wu and Alkhalifa 2015; Zhou et al. 2015) or the nested inversion technique (Biondi and Almomin 2014; Wang et al. 2016), I separate the velocity model into the background velocity and reflectivity models. Modes IV and V of diffraction-angle filtering are applied for the reconstruction of the background velocity model and reflectivity model, respectively. The near-zero-offset reflectivity built by using Mode V provides additional low-wavenumber components of the FWI gradient along the wavepaths of the reflected waves. Then, Mode IV extracts low-wavenumber components of the FWI gradient incorporating the contributions of both the diving and reflected waves for the reconstruction of the background velocity model. Modes IV and V of diffraction-angle filtering control the intermediate scattering-angle energy, which prevents the leakage between the low-wavenumber background velocity and high-wavenumber reflectivity models. In addition, the computational efforts of diffraction-angle filtering are reasonable compared with other scale separation methods. The details are described in Sections 3.1 to 3.5.

3.1. Wavenumber characteristics of acoustic FWI gradient

The wavenumber of the FWI gradient at a model point can be illustrated by diffraction tomography, which is governed by the scattering angle and local wavelength (Miller et al. 1987; Mora 1989; Fig. 3.1) as follows:

$$\mathbf{k} = \mathbf{k}_s + \mathbf{k}_r = \frac{2}{\lambda}\cos\left(\frac{\theta}{2}\right)\mathbf{n} \quad , \tag{3-1}$$

where $\mathbf{k}_S$ and $\mathbf{k}_R$ denote the wavenumber vectors of the source and receiver wavefields, respectively; λ is the local wavelength at a potential scatterer; θ is the scattering angle between the source and receiver wavefields; and $\mathbf{n}$ is the normalization of the wavenumber vector $\mathbf{k}$. Equation (3-1) demonstrates that low frequencies and large scattering angles contribute to the low-wavenumber update of FWI.

To examine the wavenumber properties of the acoustic FWI gradient for reflection-dominated data, an acoustic FWI example of synthetic data recorded by one source-receiver pair in a 1D P-wave velocity model with a single reflector is presented in Fig. 3.2. It is assumed that an initial P-wave velocity model is inaccurate and no prior information of subsurface reflectors is known, which is a general assumption for conventional FWI. As mentioned in Section 2.2.1, the gradient is formed the by zero-lag cross-correlation between the source and receiver wavefields. Then, the receiver wavefield is generated by back-propagating the data residual, which is mainly associated with diving (direct) wave residual and reflected wave residual in this case.

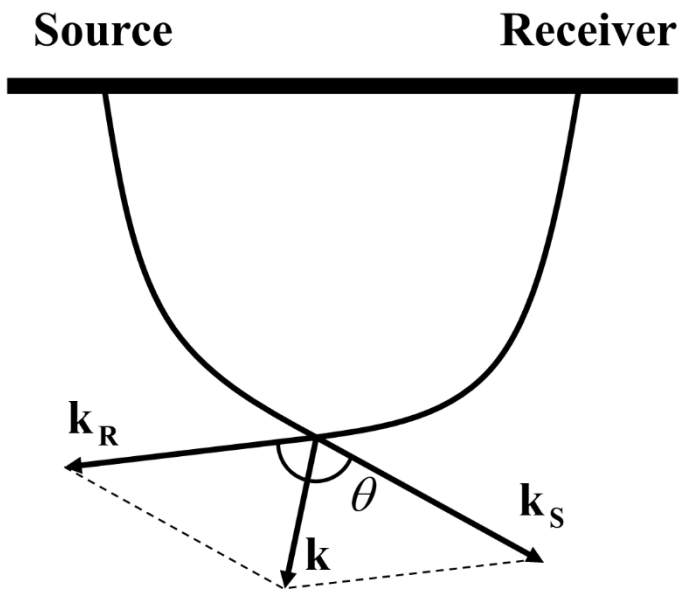

Fig. 3.1. The wavenumber of diffraction tomography with respect to a potential scatterer in a subsurface model. The wavenumber vectors of the source and receiver wavefields are denoted by $\mathbf{k}_S$ and $\mathbf{k}_R$, respectively. θ denotes the scattering angle between the source and receiver wavefields. Then, the wavenumber vector $\mathbf{k}$ is plotted by the source-receiver pair at the potential scatterer during FWI.

Because the initial P-wave velocity model is a smooth background velocity with no reflectors, only downgoing (incident) source and receiver wavefields exist. The downgoing wavefront of the receiver wavefield excited by the diving (direct) wave residual interferes with the downgoing wavefront of the source wavefield. The aperture angle of their wavenumber vectors (θ^d) is nearly 180°, which derives ellipsoidal low-wavenumber gradient component along the wavepath of the diving (direct) wave (the so-called first Fresnel zone; Woodward 1992; Virieux and Operto 2009). On the other hand, the interference of the downgoing wavefront of the receiver wavefield excited by the reflected wave residual and the source wavefield derives ellipsoidal high-wavenumber gradient component whose focal points are the source and receiver (the so-called migration isochrone; Tarantola 1984; Lailly 1983). The aperture angle of their wavenumber vectors (θ^m) is nearly 0° in this case. Fig. 3.3 illustrates the gradient computation mentioned above. The stack of the first Fresnel zones over all source-receiver pairs composes the low-wavenumber components of the gradient that mainly contribute to fitting kinematic errors of the diving waves, while the stack of the migration isochrones over all source-receiver pairs composes the high-wavenumber components of the gradient that mainly contribute to fitting amplitude errors of the reflected waves.

Next, it is assumed that the reflectivity model is reconstructed from the initial velocity model (Fig. 3.4). In this case, as the initial velocity model is slower (faster) than the true velocity model, the reflector is built at slightly shallower (deeper) depth. Then, both the source and receiver wavefields generate upgoing (scattered) components. The interference of the upgoing wavefront of the receiver wavefield

excited by the reflected wave residual and the downgoing wavefront of the source wavefield generates the first Fresnel zone where the aperture angle of their wavenumber vectors (θ^r) is nearly 180°. Likewise, the interference of the upgoing wavefront of the source wavefield and the downgoing wavefront of the receiver wavefield of the reflected wave residual generates another first Fresnel zone (Xu et al. 2012; Brossier et al. 2015). This pair of first Fresnel zones appear in a rabbit-ear shape, which can reach the deeper parts of the subsurface with a short-spread acquisition geometry. The detail is illustrated in Fig. 3.5. The first Fresnel zone derived by the diving (direct) wave mainly recovers the low-vertical-wavenumber structures along the horizontal wavepath of the diving wave, while the pair of the first Fresnel zones recovers the low-horizontal-wavenumber structures along the vertical wavepath of the reflected wave (Mora 1989; Alkhalifah 2015a; Zhou et al. 2018).

To recover the low-wavenumber variations of deep targets by using the diving waves, wide-aperture seismic data acquisition is essential. On the other hand, the reflected waves can retrieve the deep low-wavenumber structures with relatively short offsets. In such a complementary manner, the velocity model update with wider low-wavenumber coverage derived by kinematic information of the diving and reflected waves can be provided. However, the prior reflectivity information lacks in the early stage of conventional FWI. If the initial velocity models deviate from the true models, low-wavenumber structures of the deep targets are not properly recovered, but high-wavenumber structures are dominantly reconstructed by the migration isochrones at wrong positions in conventional FWI (Mora 1989).

Coupling of the high- and low-wavenumber components of the gradient causes strong non-linearity when initial velocity models are not accurate enough to image reflectors at their correct positions. To mitigate non-linearity of conventional FWI, efficient schemes of separating the high- and low-wavenumber components of the gradient need to be introduced for a large-scale problem like 3D FWI.

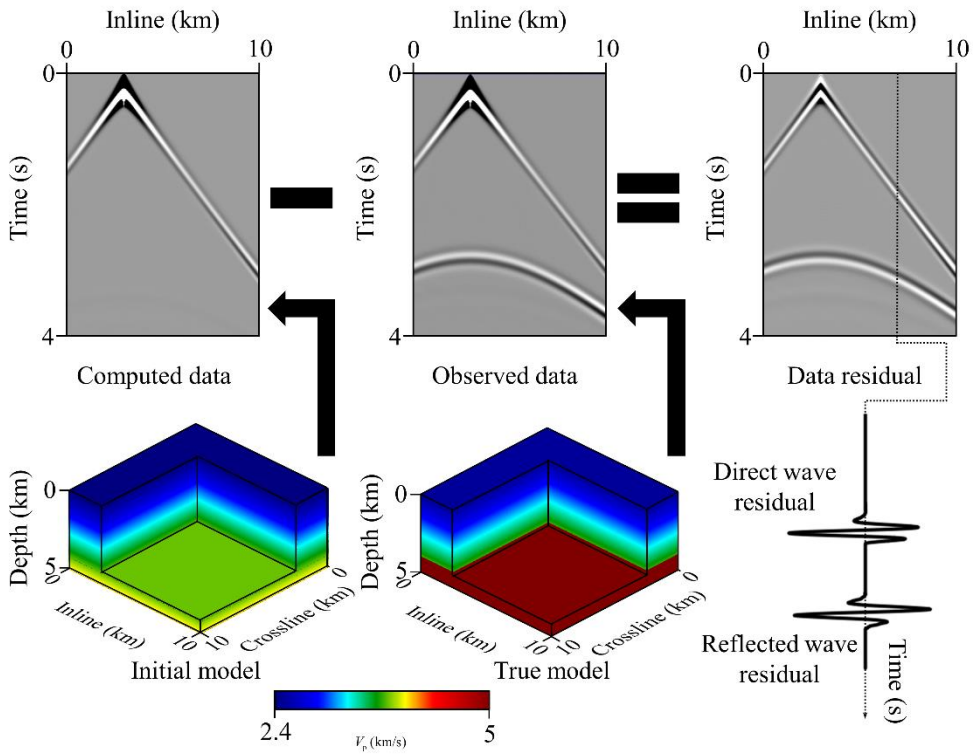

Fig. 3.2. The residual between the numerically computed and observed pressure data. The observed pressure data are generated for an 1D P-wave velocity model with a single reflector, which consist of the direct and reflected waves. Assuming a kinematically inaccurate initial P-wave velocity model which has no prior information of subsurface reflectors, the data residual consists of the direct and reflected wave residuals. The data residual then plays a role as the adjoint source of the adjoint wavefield. In this case, the reflected wave residuals are mainly related to amplitude errors.

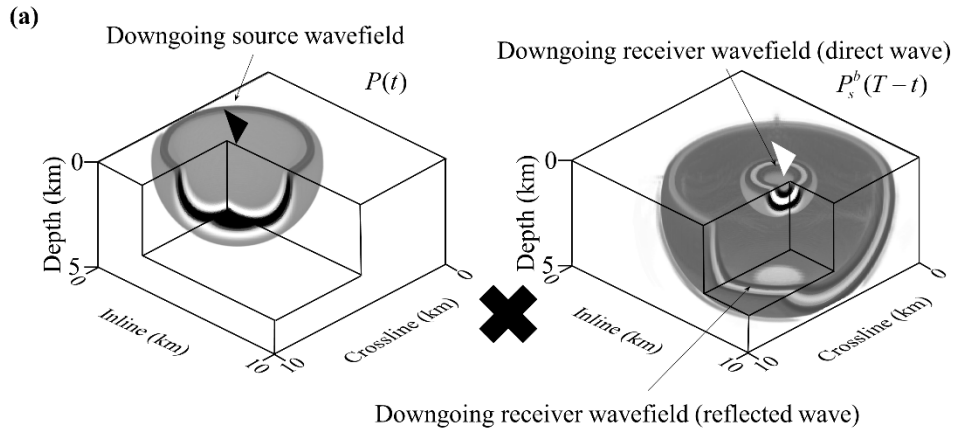

Fig. 3.3. Diagram of computing the gradient with no prior reflector for 3D acoustic FWI in the time domain. The background parts are transparent for visibility. (a) The downgoing spherical wavefronts are centered at the source or receiver position. Note that the receiver wavefield is computed in the reverse time order. The black and white triangles denote the source and receiver positions, respectively. (b) The red arrows indicate the wavenumber vectors of the downgoing source wavefield and diving-wave-related downgoing receiver wavefield, which make the aperture angle nearly 180°. It derives ellipsoidal low-wavenumber gradient components. The blue arrows indicate the wavenumber vectors of the downgoing source wavefield and reflected-wave-related downgoing receiver wavefield, which make the aperture angle nearly 0°. It derives ellipsoidal high-wavenumber gradient components. (c) The inline vertical slice is also extracted and displayed.

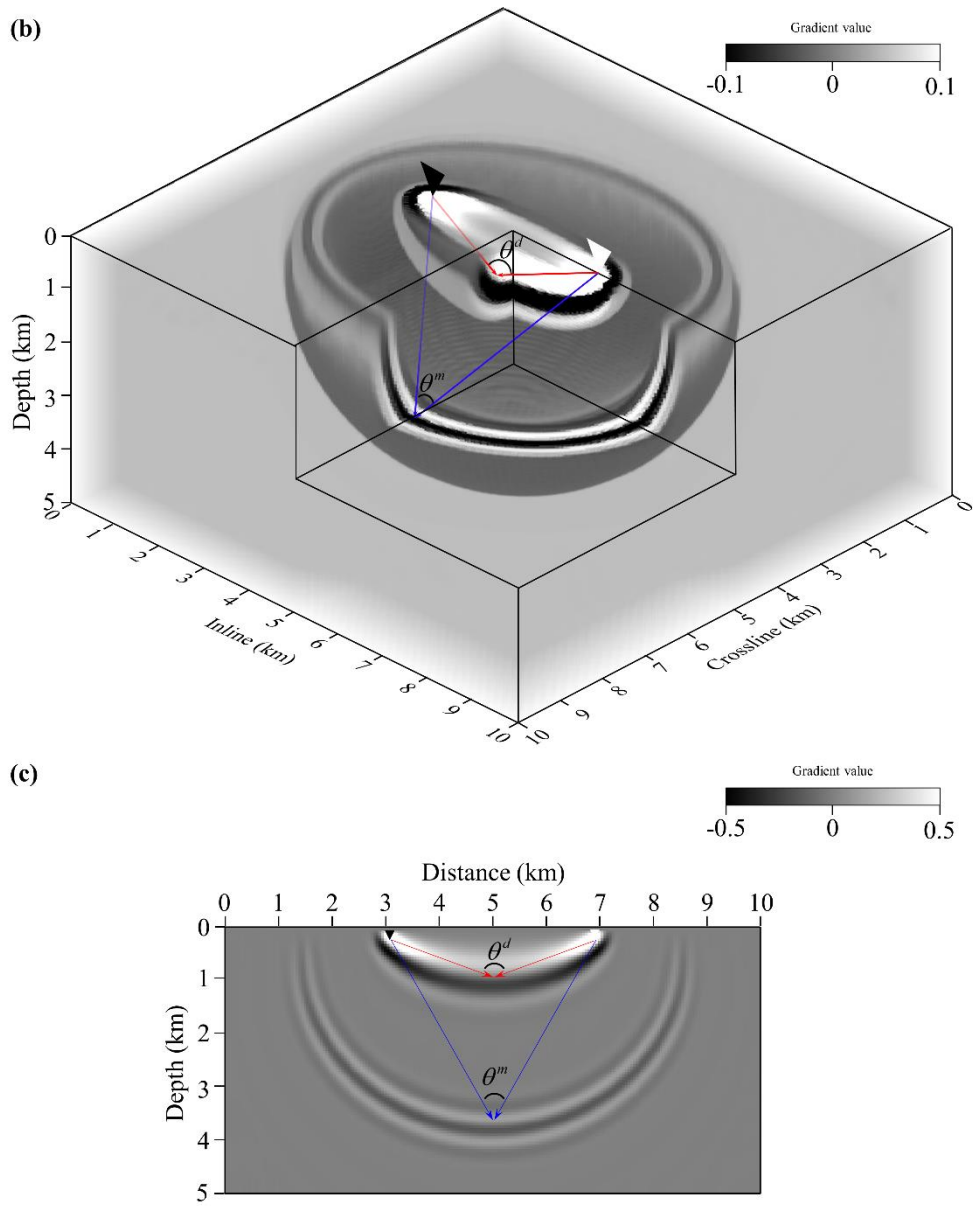

Fig. 3.3. (Continued)

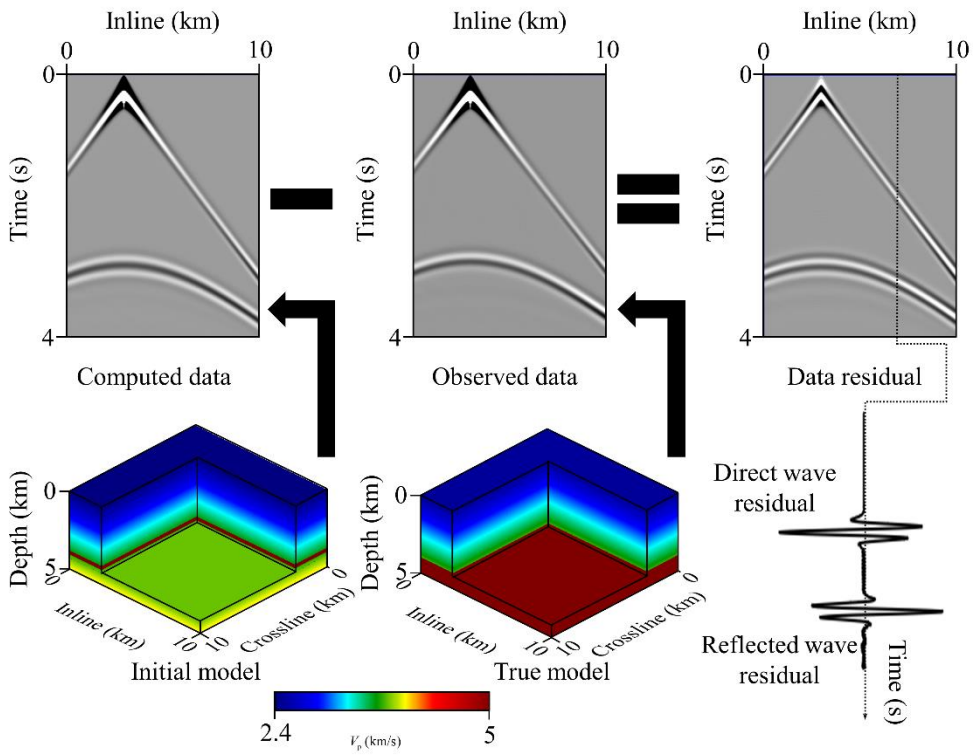

Fig. 3.4. The residual between the numerically computed and observed pressure data when the initial model includes the prior reflector that generates reflection in the computed data. The data residual consists of the direct and reflected wave residuals. However, unlike Fig. 3.2, the reflected wave residual is now related to both amplitude and kinematic errors.

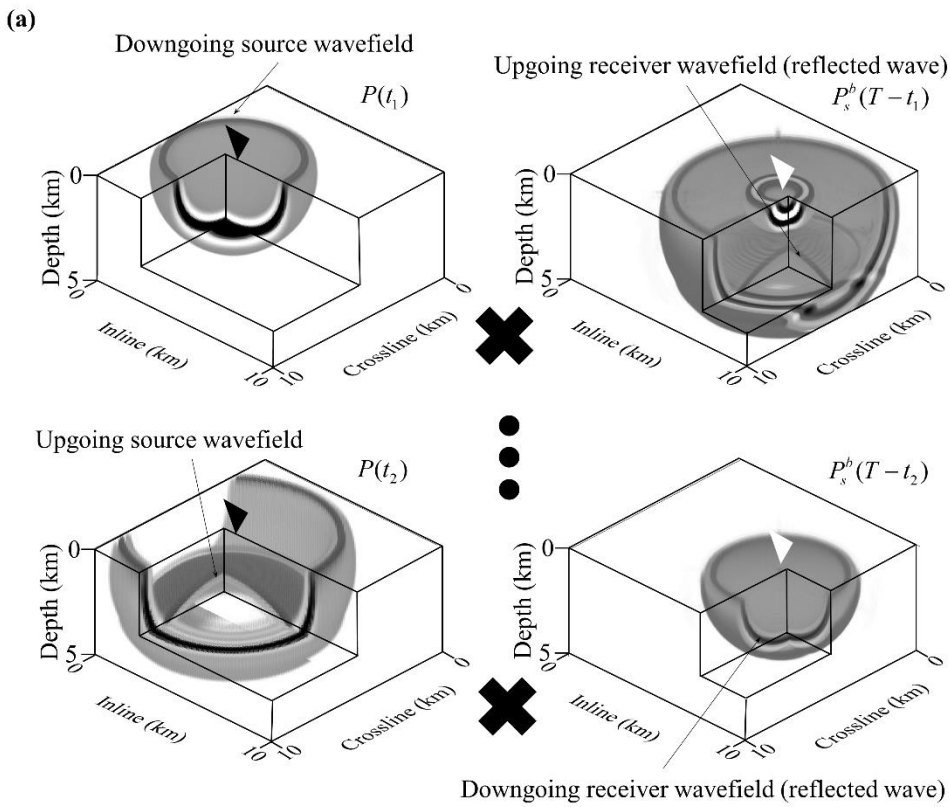

Fig. 3.5. Diagram of computing the gradient with the prior reflector for 3D acoustic FWI in the time domain. (a) When the downgoing wavefronts meet the reflector, reflected upgoing wavefronts are generated. (b) The cyan arrows indicate the wavenumber vectors of the upgoing source wavefield and reflected-wave-related downgoing receiver wavefield, which make the aperture angle nearly 180°. Likewise, the wavenumber vectors of the downgoing source wavefield and reflected-wave-related upgoing receiver wavefield make the aperture angle nearly 180°. They derive a pair of ellipsoidal low-wavenumber gradient components. (c) The inline vertical slice is extracted and displayed.

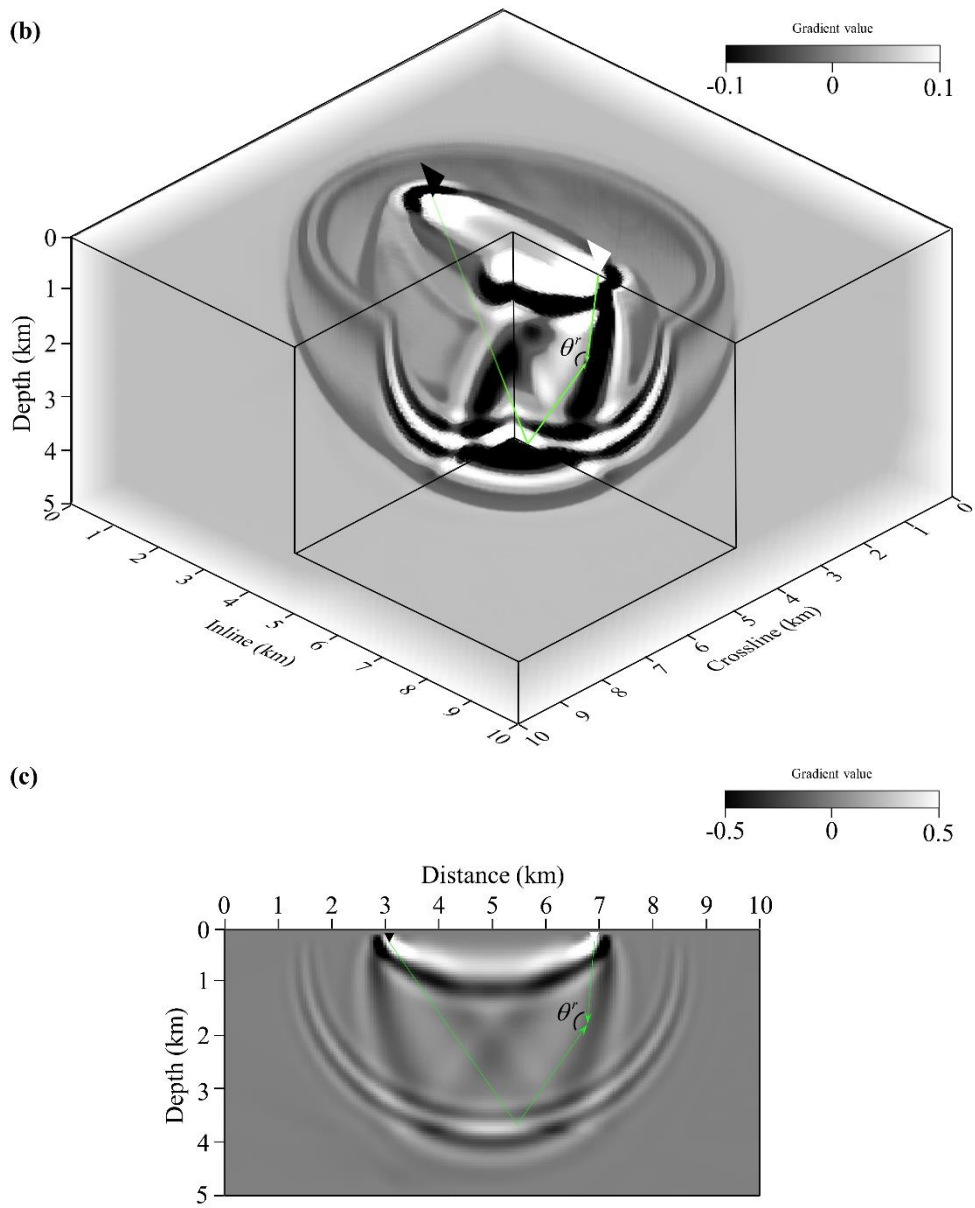

Fig. 3.5. (Continued)

3.2. Diffraction-angle filtering for acoustic FWI

The preferential low-wavenumber update can mitigate the non-linearity of FWI. Therefore, separation of the high- and low-wavenumber components of the gradient becomes one of the key issues for successful FWI. In this thesis, diffraction-angle filtering (Oh et al. 2021) is introduced to control the wavenumber components of update with respect to the P-wave velocity while avoiding a large increase in computational effort. Formulation and mechanism of diffraction-angle filtering, implementation of diffraction-angle filtering on a staggered grid set and computational requirements are described in Sections 3.2.1 to 3.2.3.

3.2.1. Formulation and mechanism of diffraction-angle filtering

The main idea of diffraction-angle filtering is to modify the virtual source term to control the diffraction patterns of the partial derivative wavefields. Based on the expression of the virtual body-force source represented in equation (2-14), diffraction-angle filtering modifies the conventional virtual source of the P-wave velocity as follows (Oh et al. 2021):

$$\begin{aligned}\mathbf{f}_{s,i,j,k}^{v,\mathrm{DAF}}(\mathbf{x}_{i,j,k},\, t,\, V_{\mathrm{p}}(\mathbf{x})) = a_1 \nabla\left[V_{\mathrm{p}}(\mathbf{x}_{i,j,k})\nabla\cdot\mathbf{u}(\mathbf{x}_s,\, \mathbf{x}_{i,j,k},\, t,\, V_{\mathrm{p}}(\mathbf{x}))\right] \\ + a_2\left[\frac{1}{V_{\mathrm{p}}(\mathbf{x}_{i,j,k})}\mathbf{a}(\mathbf{x}_s,\, \mathbf{x}_{i,j,k},\, t,\, V_{\mathrm{p}}(\mathbf{x}))\right] \\ + a_1\left(\frac{1-2\sigma}{2-2\sigma}\right)\left[\frac{\partial \mathrm{s}(\mathbf{x}_s,\, \mathbf{x},\, t,\, V_{\mathrm{p}}(\mathbf{x}))}{\partial V_{\mathrm{p}}(\mathbf{x}_{i,j,k})}\right]\end{aligned}, \tag{3-1}$$

where

$$
\begin{aligned}
&\frac{\partial s(\mathbf{x}_s, \mathbf{x}, t, V_p(\mathbf{x}))}{\partial V_p(\mathbf{x}_{i,j,k})} \\
&= -2\nabla\left(V_p(\mathbf{x}_{i,j,k})\right)\left[\nabla\cdot\mathbf{u}(\mathbf{x}_s, \mathbf{x}_{i,j,k}, t, V_p(\mathbf{x}))\right] \\
&\quad + \nabla\left(V_p(\mathbf{x}_{i,j,k})\right)\cdot\left[\nabla\mathbf{u}(\mathbf{x}_s, \mathbf{x}_{i,j,k}, t, V_p(\mathbf{x})) + \left(\nabla\mathbf{u}(\mathbf{x}_s, \mathbf{x}_{i,j,k}, t, V_p(\mathbf{x}))\right)^T\right] \\
&\quad - V_p(\mathbf{x}_{i,j,k})\left[\nabla\times\left(\nabla\times\mathbf{u}(\mathbf{x}_s, \mathbf{x}_{i,j,k}, t, V_p(\mathbf{x}))\right)\right]
\end{aligned}
\quad . \quad (3\text{-}2)
$$

The last term in equation (3-2) is zero in acoustic cases, because the curl of the P-wave is zero. In equation (3-2), there are three weighting factors (represented by a_1, a_2 and artificially-defined Poisson's ratio σ), which control the influences of the three terms (i.e., three square brackets). The first term is the conventional virtual source of the P-wave velocity as shown in equation (2-14). The second term controls energy at either small or large diffraction angles as ISIC or ENIC does. The last term additionally suppresses energy at intermediate diffraction angles, which can cause the coupling of high- and low-wavenumber components of the gradient during FWI. The second and last terms can be activated by changing a set of weighting factors (a_1, a_2 and σ) as shown in Table 3.1. The virtual source obtained by applying mode I is identical to the conventional virtual source of the P-wave velocity. The virtual sources resulting from applying modes II and III are the same as the virtual sources of the P-wave velocity and P-wave impedance obtained from the acoustic wave equation with the V_p - I_p parameterization, respectively. Modes IV and V describe the virtual sources identical to those of the P-wave velocity and P-wave impedance in the elastic equations with the V_p - I_p - σ parameterization, respectively. I set artificial Poisson's ratio (σ) to be 0.25 to activate the last term without generating artificial backscattering energy (Oh et al. 2021).

Table 3.1. Five diffraction-angle filtering modes and their weighting factors.

DAF mode	Weighting factors (a_1, a_2 and σ)	Corresponding PP diffraction pattern
Mode I	(2, 0, 0.5)	V_p in acoustic FWI with V_p parameterization
Mode II	(1, 1, 0.5)	V_p in acoustic FWI with V_p - I_p parameterization
Mode III	(1, -1, 0.5)	I_p in acoustic FWI with V_p - I_p parameterization
Mode IV	(1, 1, 0.25)	V_p in elastic FWI with V_p - I_p - σ parameterization
Mode V	(1, -1, 0.25)	I_p in elastic FWI with V_p - I_p - σ parameterization

Fig. 3.6 shows the diffraction patterns generated by the virtual sources resulting from applying five diffraction-angle filtering modes. Mode I yields an isotropic diffraction pattern (Fig. 3.6b). The diffraction patterns of mode II (Fig. 3.6c) and mode III (Fig. 3.6d) isolate energy at either large or small diffraction angles to some extent, but still diffract energy over intermediate diffraction angles, which causes cross-talk effects between high- and low-wavenumber components of the gradient. On the other hand, the energy at intermediate diffraction angles of mode IV (Fig. 3.6e) and mode V (Fig. 3.6f) are suppressed by mimicking the diffraction patterns of the P-wave velocity and P-wave impedance in elastic FWI with V_{p} - I_{p} - σ parameterization. Note that the diffraction pattern of the P-wave velocity and its filtered versions are independent of the azimuth.

Fig. 3.7(a) shows a schematic diagram illustrating numerical generation of the partial derivative wavefields derived by the three terms of equation (3-2) with respect to different incidence angles. Fig. 3.7(b) shows that the diffraction patterns from the virtual source corresponds to the first term in equation (3-2), which is identical to the conventional virtual source of the P-wave velocity. The explosive virtual source of the P-wave velocity generates isotropic wavefront and therefore particles have bidirectional motion. The second term in equation (3-2) shows the diffraction pattern similar to that of the density obtained using the parameterization of the Lamé constants and density (Fig. 3.7c), and the last term describes the diffraction pattern of the S-wave velocity obtained using the V_{p} - V_{s} -density parameterization (Fig. 3.7d; Tarantola, 1986; Oh et al. 2021). Considering the

dispersion relation ($\omega^2 = V_p^2 k^2$), the first and second terms have identical amplitudes if a_1 is equal to a_2 .

As the second term generates unidirectional particle motions, it cancels either the backscattering or forward-scattering energy and doubles the counterparts. The last term emits the main PP diffraction energy at intermediate diffraction angles. By changing the Poisson's ratio from 0.5 to 0, the diffraction energy at intermediate diffraction angles is gradually suppressed. When the Poisson's ratio is less than 0.25, backscattering energy is artificially generated. Its particle motions are opposite of the original motions, which cause incorrect update. Therefore, the Poisson's ratio should be 0.25 to yield more isolated diffraction patterns at large and small diffraction angles while preserving correct update.

The partial derivative wavefields computed numerically from the virtual sources with modes II, III, IV and V are shown in Fig. 3.8. Modes II and III provide the diffraction patterns isolated at large and small diffraction angles, respectively, and modes IV and V additionally filter out energy at intermediate diffraction angles as expected. Then, the filtered partial derivative wavefields, which only include energy at large or small diffraction angles (which are identical to the aperture angles in equation 3-1), will lead to low- or high-wavenumber updates following equation (3-1). Compared to the previously-proposed scattering-angle filtering methods, diffraction-angle filtering controls the diffraction pattern by modifying the virtual source. Modification of the virtual source is done by combining the spatial and temporal derivatives of the wavefields.

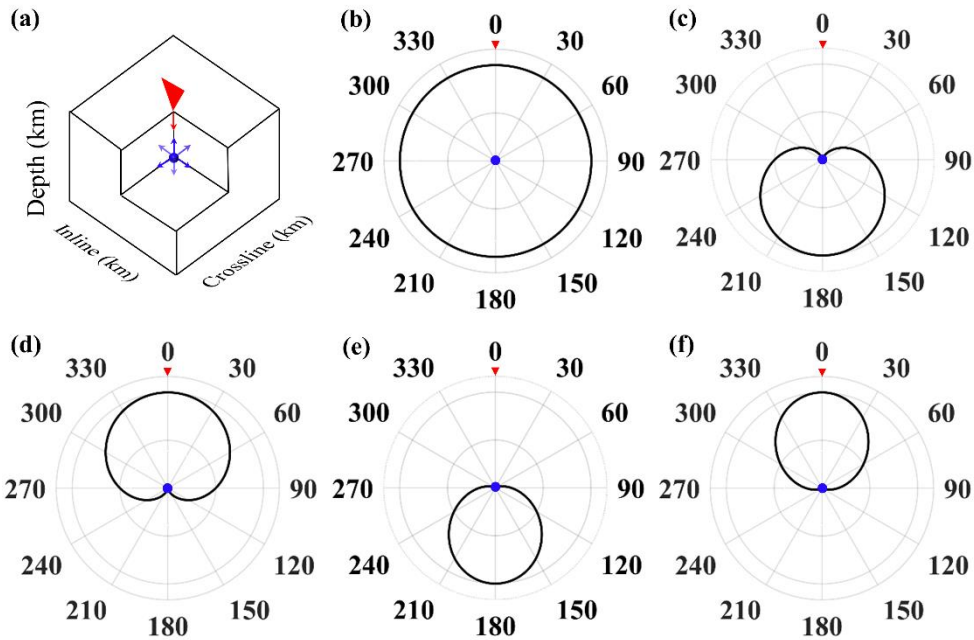

Fig. 3.6. (a) A schematic diagram illustrating generation of the partial derivative wavefield derived by a single diffractor in an isotropic homogeneous background media. Diffraction patterns of the P-wave velocity filtered by (b) mode I, (c) mode II, (d) mode III, (e) mode IV, and (f) mode V. The red triangles and blue dots indicate the locations of seismic source and virtual source of the P-wave velocity, respectively. Note that filtered diffraction patterns of the P-wave velocity are independent of the azimuth angles.

Because no transforms are required across the data domains, diffraction-angle filtering can be easily applied to a large-scale problem like 3D FWI. While scattering-angle filtering suggested by Alkhalifah (2015b) or Yao et al. (2018) can design a more sophisticated filter, modes IV and V of diffraction-angle filtering can effectively separate the migration and tomographic components with lower computational efforts.

3.2.2. Implementation on a staggered grid set

The computation of the virtual source in equation (3-2) depends on the specific details of the finite approximation method. The virtual source is derived by differentiating wave equation with respect to the model parameter at the nodal point (i, j, k), and thus consists of local non-zero values near the nodal point (i, j, k). The virtual source modified by diffraction-angle filtering consists of the spatial derivatives of the particle displacement and pressure wavefields. The spatial derivatives of the particle displacement wavefield, which are identical to the normal and shear strain wavefields, are computed on the staggered-grid set as shown in Fig. 3.9. Averaging method is applied (Levander 1988; Mittet 2002) as follows:

$$\begin{aligned}
\frac{1}{V_{\mathrm{p}}(\mathbf{x}_{i+1/2,j,k})} &= \left(\frac{2}{V_{\mathrm{p}}(\mathbf{x}_{i,j,k}) + V_{\mathrm{p}}(\mathbf{x}_{i+1,j,k})} \right) \\
\frac{1}{V_{\mathrm{p}}(\mathbf{x}_{i,j+1/2,k})} &= \left(\frac{2}{V_{\mathrm{p}}(\mathbf{x}_{i,j,k}) + V_{\mathrm{p}}(\mathbf{x}_{i,j+1,k})} \right), \\
\frac{1}{V_{\mathrm{p}}(\mathbf{x}_{i,j,k+1/2})} &= \left(\frac{2}{V_{\mathrm{p}}(\mathbf{x}_{i,j,k}) + V_{\mathrm{p}}(\mathbf{x}_{i,j,k+1})} \right)
\end{aligned}$$

and

$$V_{\mathrm{p}}(\mathbf{x}_{i+1/2,\,j+1/2,k}) = \frac{1}{4}\Big(V_{\mathrm{p}}(\mathbf{x}_{i,\,j,k}) + V_{\mathrm{p}}(\mathbf{x}_{i+1,\,j,k}) + V_{\mathrm{p}}(\mathbf{x}_{i,\,j+1,k}) + V_{\mathrm{p}}(\mathbf{x}_{i+1,\,j+1,k})\Big)$$
$$V_{\mathrm{p}}(\mathbf{x}_{i+1/2,\,j,k+1/2}) = \frac{1}{4}\Big(V_{\mathrm{p}}(\mathbf{x}_{i,\,j,k}) + V_{\mathrm{p}}(\mathbf{x}_{i+1,\,j,k}) + V_{\mathrm{p}}(\mathbf{x}_{i,\,j,k+1}) + V_{\mathrm{p}}(\mathbf{x}_{i+1,\,j,k+1})\Big). \quad (3\text{-}3)$$
$$V_{\mathrm{p}}(\mathbf{x}_{i,\,j+1/2,k+1/2}) = \frac{1}{4}\Big(V_{\mathrm{p}}(\mathbf{x}_{i,\,j,k}) + V_{\mathrm{p}}(\mathbf{x}_{i,\,j+1,k}) + V_{\mathrm{p}}(\mathbf{x}_{i,\,j,k+1}) + V_{\mathrm{p}}(\mathbf{x}_{i,\,j+1,k+1})\Big)$$

Note that the P-wave velocity should be always assigned at the locations of the quantities it scales. The virtual source of the P-wave velocity at the nodal point (i, j, k) is derived by differentiating the wave equation with respect to V_{p} at the nodal point (i, j, k) and the P-wave velocities at the other nodal points are treated as constant. Based on the aforementioned averaging method, the numerical scheme for the modified virtual source derived by V_{p} at the nodal point (i, j, k) can be written as follows (Fig. 3.10):

$$\begin{aligned}
\mathrm{f}^{v,\mathrm{DAF}}_{s,i,j,k,x}(\mathbf{x}_{i+1/2,\,j,k},t_n) = {} & -a_1\frac{V_{\mathrm{p}}(\mathbf{x}_{i,\,j,k})}{dx}e_{nn}(\mathbf{x}_s,\mathbf{x}_{i,\,j,k},t_n) + a_2\frac{1}{2}\frac{1}{V_{\mathrm{p}}(\mathbf{x}_{i+1/2,\,j,k})}\mathrm{a}_x(\mathbf{x}_s,\mathbf{x}_{i+1/2,\,j,k},t_n) \\
& + 2a_1\left(\frac{1-2\sigma}{2-2\sigma}\right)\frac{V_{\mathrm{p}}(\mathbf{x}_{i,\,j,k})}{dx}\Bigg[e_{nn}(\mathbf{x}_s,\mathbf{x}_{i,\,j,k},t_n) - e_{xx}(\mathbf{x}_s,\mathbf{x}_{i,\,j,k},t_n) \\
& - \frac{1}{4}\Big(e_{xy}(\mathbf{x}_s,\mathbf{x}_{i+1/2,\,j+1/2,k},t_n) - e_{xy}(\mathbf{x}_s,\mathbf{x}_{i+1/2,\,j-1/2,k},t_n)\Big) \\
& - \frac{1}{4}\Big(e_{xz}(\mathbf{x}_s,\mathbf{x}_{i+1/2,\,j,k+1/2},t_n) - e_{xz}(\mathbf{x}_s,\mathbf{x}_{i+1/2,\,j,k-1/2},t_n)\Big)\Bigg]
\end{aligned},$$

$$\begin{aligned}
\mathrm{f}^{v,\mathrm{DAF}}_{s,i,j,k,x}(\mathbf{x}_{i-1/2,\,j,k},t_n) = {} & a_1\frac{V_{\mathrm{p}}(\mathbf{x}_{i,\,j,k})}{dx}e_{nn}(\mathbf{x}_s,\mathbf{x}_{i,\,j,k},t_n) + a_2\frac{1}{2}\frac{1}{V_{\mathrm{p}}(\mathbf{x}_{i-1/2,\,j,k})}\mathrm{a}_x(\mathbf{x}_s,\mathbf{x}_{i-1/2,\,j,k},t_n) \\
& - 2a_1\left(\frac{1-2\sigma}{2-2\sigma}\right)\frac{V_{\mathrm{p}}(\mathbf{x}_{i,\,j,k})}{dx}\Bigg[e_{nn}(\mathbf{x}_s,\mathbf{x}_{i,\,j,k},t_n) - e_{xx}(\mathbf{x}_s,\mathbf{x}_{i,\,j,k},t_n) \\
& - \frac{1}{4}\Big(e_{xy}(\mathbf{x}_s,\mathbf{x}_{i-1/2,\,j+1/2,k},t_n) - e_{xy}(\mathbf{x}_s,\mathbf{x}_{i-1/2,\,j-1/2,k},t_n)\Big) \\
& - \frac{1}{4}\Big(e_{xz}(\mathbf{x}_s,\mathbf{x}_{i-1/2,\,j,k+1/2},t_n) - e_{xz}(\mathbf{x}_s,\mathbf{x}_{i-1/2,\,j,k-1/2},t_n)\Big)\Bigg]
\end{aligned},$$

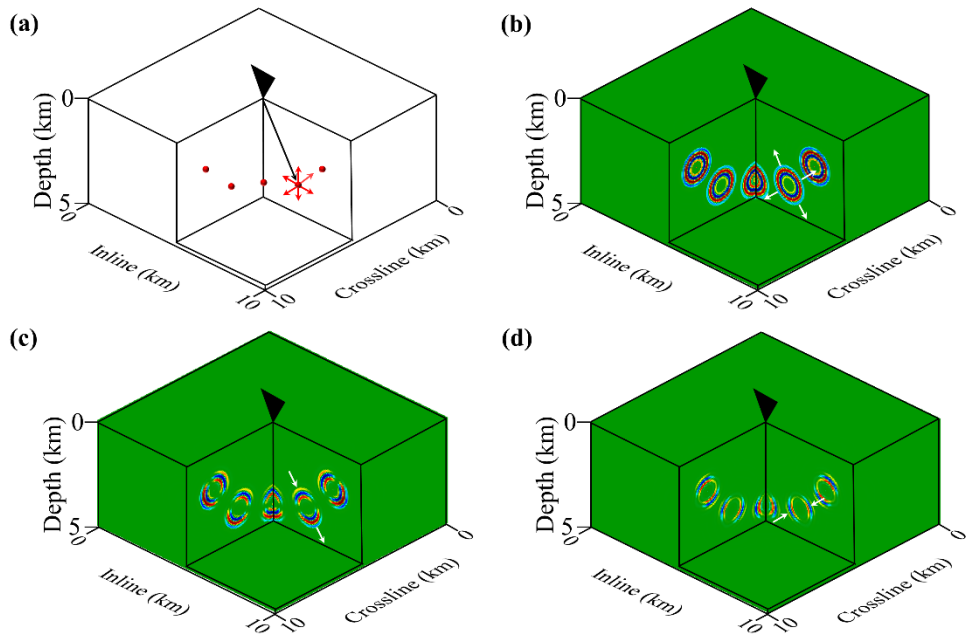

Fig. 3.7. (a) A schematic diagram illustrating generation of the partial derivative wavefield derived by diffractors in an isotropic homogeneous background media with different incidence angles. The black triangles and red dots indicate the locations of seismic source and virtual sources in equation (3-2). The partial derivative wavefields excited by the (b) first term (the virtual source with mode I), (c) second term and (d) last term in equation (3-2). The white arrows denote particle motions derived by the partial derivative wavefields.

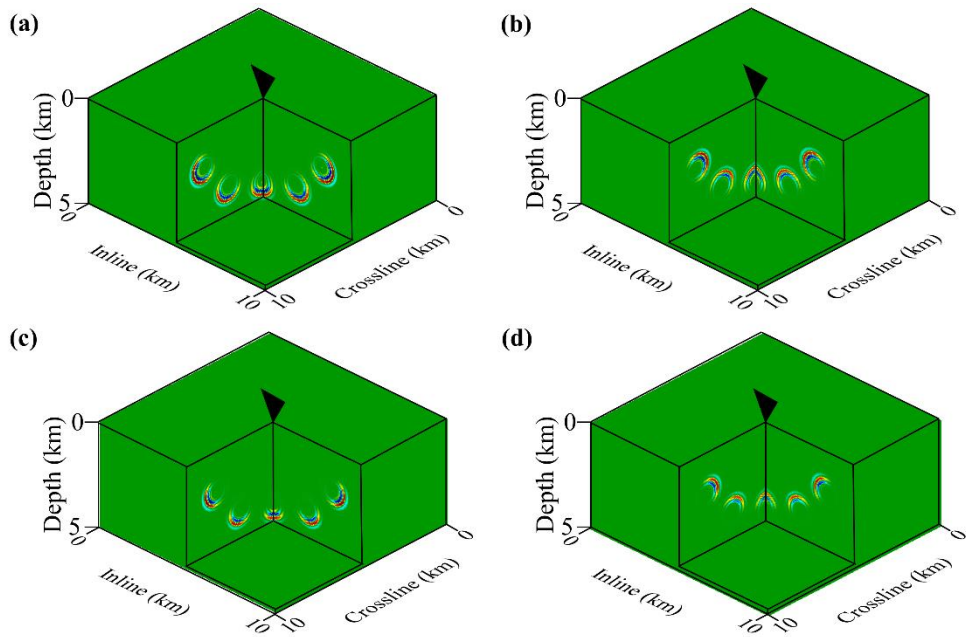

Fig. 3.8. The partial derivative wavefields excited by the virtual sources with modes (a) II, (b) III, (c) IV and (d) V.

$$\mathrm{f}^{v,\mathrm{DAF}}_{s,i,j,k,x}(\mathbf{x}_{i-1/2,j-1/2,k},t_n)=2a_1\left(\frac{1-2\sigma}{2-2\sigma}\right)\frac{V_\mathrm{p}(\mathbf{x}_{i,j,k})}{4dx}e_{xy}(\mathbf{x}_s,\mathbf{x}_{i-1/2,j-1/2,k},t_n)\,,$$

$$\mathrm{f}^{v,\mathrm{DAF}}_{s,i,j,k,x}(\mathbf{x}_{i+1/2,j-1/2,k},t_n)=2a_1\left(\frac{1-2\sigma}{2-2\sigma}\right)\frac{V_\mathrm{p}(\mathbf{x}_{i,j,k})}{4dx}e_{xy}(\mathbf{x}_s,\mathbf{x}_{i+1/2,j-1/2,k},t_n)\,,$$

$$\mathrm{f}^{v,\mathrm{DAF}}_{s,i,j,k,x}(\mathbf{x}_{i-1/2,j+1/2,k},t_n)=-2a_1\left(\frac{1-2\sigma}{2-2\sigma}\right)\frac{V_\mathrm{p}(\mathbf{x}_{i,j,k})}{4dx}e_{xy}(\mathbf{x}_s,\mathbf{x}_{i-1/2,j+1/2,k},t_n)\,,$$

$$\mathrm{f}^{v,\mathrm{DAF}}_{s,i,j,k,x}(\mathbf{x}_{i+1/2,j+1/2,k},t_n)=-2a_1\left(\frac{1-2\sigma}{2-2\sigma}\right)\frac{V_\mathrm{p}(\mathbf{x}_{i,j,k})}{4dx}e_{xy}(\mathbf{x}_s,\mathbf{x}_{i+1/2,j+1/2,k},t_n)\,,$$

$$\mathrm{f}^{v,\mathrm{DAF}}_{s,i,j,k,x}(\mathbf{x}_{i-1/2,j,k-1/2},t_n)=2a_1\left(\frac{1-2\sigma}{2-2\sigma}\right)\frac{V_\mathrm{p}(\mathbf{x}_{i,j,k})}{4dx}e_{xz}(\mathbf{x}_s,\mathbf{x}_{i-1/2,j,k-1/2},t_n)\,,$$

$$\mathrm{f}^{v,\mathrm{DAF}}_{s,i,j,k,x}(\mathbf{x}_{i+1/2,j,k-1/2},t_n)=2a_1\left(\frac{1-2\sigma}{2-2\sigma}\right)\frac{V_\mathrm{p}(\mathbf{x}_{i,j,k})}{4dx}e_{xz}(\mathbf{x}_s,\mathbf{x}_{i+1/2,j,k-1/2},t_n)\,,$$

$$\mathrm{f}^{v,\mathrm{DAF}}_{s,i,j,k,x}(\mathbf{x}_{i-1/2,j,k+1/2},t_n)=-2a_1\left(\frac{1-2\sigma}{2-2\sigma}\right)\frac{V_\mathrm{p}(\mathbf{x}_{i,j,k})}{4dx}e_{xz}(\mathbf{x}_s,\mathbf{x}_{i-1/2,j,k+1/2},t_n)\,,$$

$$\mathrm{f}^{v,\mathrm{DAF}}_{s,i,j,k,x}(\mathbf{x}_{i+1/2,j,k+1/2},t_n)=-2a_1\left(\frac{1-2\sigma}{2-2\sigma}\right)\frac{V_\mathrm{p}(\mathbf{x}_{i,j,k})}{4dx}e_{xz}(\mathbf{x}_s,\mathbf{x}_{i+1/2,j,k+1/2},t_n)\,,$$

$$\begin{aligned}\mathrm{f}^{v,\mathrm{DAF}}_{s,i,j,k,y}(\mathbf{x}_{i,j+1/2,k},t_n)=&-a_1\frac{V_\mathrm{p}(\mathbf{x}_{i,j,k})}{dy}e_{nn}(\mathbf{x}_s,\mathbf{x}_{i,j,k},t_n)+a_2\frac{1}{2}\frac{1}{V_\mathrm{p}(\mathbf{x}_{i,j+1/2,k})}\mathrm{a}_y(\mathbf{x}_s,\mathbf{x}_{i,j+1/2,k},t_n)\\&+2a_1\left(\frac{1-2\sigma}{2-2\sigma}\right)\frac{V_\mathrm{p}(\mathbf{x}_{i,j,k})}{dy}\Big[e_{nn}(\mathbf{x}_s,\mathbf{x}_{i,j,k},t_n)-e_{yy}(\mathbf{x}_s,\mathbf{x}_{i,j,k},t_n)\\&-\frac{1}{4}\Big(e_{xy}(\mathbf{x}_s,\mathbf{x}_{i+1/2,j+1/2,k},t_n)-e_{xy}(\mathbf{x}_s,\mathbf{x}_{i-1/2,j+1/2,k},t_n)\Big)\\&-\frac{1}{4}\Big(e_{yz}(\mathbf{x}_s,\mathbf{x}_{i,j+1/2,k+1/2},t_n)-e_{yz}(\mathbf{x}_s,\mathbf{x}_{i,j+1/2,k-1/2},t_n)\Big)\Big]\end{aligned}\,,$$

$$\begin{aligned}\mathrm{f}^{v,\mathrm{DAF}}_{s,i,j,k,y}(\mathbf{x}_{i,j-1/2,k},t_n)=&\,a_1\frac{V_\mathrm{p}(\mathbf{x}_{i,j,k})}{dy}e_{nn}(\mathbf{x}_s,\mathbf{x}_{i,j,k},t_n)+a_2\frac{1}{2}\frac{1}{V_\mathrm{p}(\mathbf{x}_{i,j-1/2,k})}\mathrm{a}_y(\mathbf{x}_s,\mathbf{x}_{i,j-1/2,k},t_n)\\&-2a_1\left(\frac{1-2\sigma}{2-2\sigma}\right)\frac{V_\mathrm{p}(\mathbf{x}_{i,j,k})}{dy}\Big[e_{nn}(\mathbf{x}_s,\mathbf{x}_{i,j,k},t_n)-e_{yy}(\mathbf{x}_s,\mathbf{x}_{i,j,k},t_n)\\&-\frac{1}{4}\Big(e_{xy}(\mathbf{x}_s,\mathbf{x}_{i+1/2,j-1/2,k},t_n)-e_{xy}(\mathbf{x}_s,\mathbf{x}_{i-1/2,j-1/2,k},t_n)\Big)\\&-\frac{1}{4}\Big(e_{yz}(\mathbf{x}_s,\mathbf{x}_{i,j-1/2,k+1/2},t_n)-e_{yz}(\mathbf{x}_s,\mathbf{x}_{i,j-1/2,k-1/2},t_n)\Big)\Big]\end{aligned}\,,$$

$$\mathrm{f}^{v,\mathrm{DAF}}_{s,i,j,k,y}(\mathbf{x}_{i-1/2,\,j-1/2,k},t_n)=2a_1\left(\frac{1-2\sigma}{2-2\sigma}\right)\frac{V_{\mathrm{p}}(\mathbf{x}_{i,j,k})}{4dy}e_{xy}(\mathbf{x}_s,\mathbf{x}_{i-1/2,\,j-1/2,k},t_n)\,,$$

$$\mathrm{f}^{v,\mathrm{DAF}}_{s,i,j,k,y}(\mathbf{x}_{i-1/2,\,j+1/2,k},t_n)=2a_1\left(\frac{1-2\sigma}{2-2\sigma}\right)\frac{V_{\mathrm{p}}(\mathbf{x}_{i,j,k})}{4dy}e_{xy}(\mathbf{x}_s,\mathbf{x}_{i-1/2,\,j+1/2,k},t_n)\,,$$

$$\mathrm{f}^{v,\mathrm{DAF}}_{s,i,j,k,y}(\mathbf{x}_{i+1/2,\,j-1/2,k},t_n)=-2a_1\left(\frac{1-2\sigma}{2-2\sigma}\right)\frac{V_{\mathrm{p}}(\mathbf{x}_{i,j,k})}{4dy}e_{xy}(\mathbf{x}_s,\mathbf{x}_{i+1/2,\,j-1/2,k},t_n)\,,$$

$$\mathrm{f}^{v,\mathrm{DAF}}_{s,i,j,k,y}(\mathbf{x}_{i+1/2,\,j+1/2,k},t_n)=-2a_1\left(\frac{1-2\sigma}{2-2\sigma}\right)\frac{V_{\mathrm{p}}(\mathbf{x}_{i,j,k})}{4dy}e_{xy}(\mathbf{x}_s,\mathbf{x}_{i+1/2,\,j+1/2,k},t_n)\,,$$

$$\mathrm{f}^{v,\mathrm{DAF}}_{s,i,j,k,y}(\mathbf{x}_{i,\,j-1/2,k-1/2},t_n)=2a_1\left(\frac{1-2\sigma}{2-2\sigma}\right)\frac{V_{\mathrm{p}}(\mathbf{x}_{i,j,k})}{4dy}e_{yz}(\mathbf{x}_s,\mathbf{x}_{i,\,j-1/2,k-1/2},t_n)\,,$$

$$\mathrm{f}^{v,\mathrm{DAF}}_{s,i,j,k,y}(\mathbf{x}_{i,\,j+1/2,k-1/2},t_n)=2a_1\left(\frac{1-2\sigma}{2-2\sigma}\right)\frac{V_{\mathrm{p}}(\mathbf{x}_{i,j,k})}{4dy}e_{yz}(\mathbf{x}_s,\mathbf{x}_{i,\,j+1/2,k-1/2},t_n)\,,$$

$$\mathrm{f}^{v,\mathrm{DAF}}_{s,i,j,k,y}(\mathbf{x}_{i,\,j-1/2,k+1/2},t_n)=-2a_1\left(\frac{1-2\sigma}{2-2\sigma}\right)\frac{V_{\mathrm{p}}(\mathbf{x}_{i,j,k})}{4dy}e_{yz}(\mathbf{x}_s,\mathbf{x}_{i,\,j-1/2,k+1/2},t_n)\,,$$

$$\mathrm{f}^{v,\mathrm{DAF}}_{s,i,j,k,y}(\mathbf{x}_{i,\,j+1/2,k+1/2},t_n)=-2a_1\left(\frac{1-2\sigma}{2-2\sigma}\right)\frac{V_{\mathrm{p}}(\mathbf{x}_{i,j,k})}{4dy}e_{yz}(\mathbf{x}_s,\mathbf{x}_{i,\,j+1/2,k+1/2},t_n)\,,$$

and

$$\begin{aligned}\mathrm{f}^{v,\mathrm{DAF}}_{s,i,j,k,z}(\mathbf{x}_{i,\,j,k+1/2},t_n)=&-a_1\frac{V_{\mathrm{p}}(\mathbf{x}_{i,j,k})}{dz}e_{nn}(\mathbf{x}_s,\mathbf{x}_{i,j,k},t_n)+a_2\frac{1}{2}\frac{1}{V_{\mathrm{p}}(\mathbf{x}_{i,j,k+1/2})}\mathrm{a}_z(\mathbf{x}_s,\mathbf{x}_{i,j,k+1/2},t_n)\\&+2a_1\left(\frac{1-2\sigma}{2-2\sigma}\right)\frac{V_{\mathrm{p}}(\mathbf{x}_{i,j,k})}{dz}\Big[e_{nn}(\mathbf{x}_s,\mathbf{x}_{i,j,k},t_n)-e_{zz}(\mathbf{x}_s,\mathbf{x}_{i,j,k},t_n)\\&-\frac{1}{4}\Big(e_{xz}(\mathbf{x}_s,\mathbf{x}_{i+1/2,\,j+1/2,k},t_n)-e_{xz}(\mathbf{x}_s,\mathbf{x}_{i-1/2,\,j+1/2,k},t_n)\Big)\\&-\frac{1}{4}\Big(e_{yz}(\mathbf{x}_s,\mathbf{x}_{i,\,j+1/2,k+1/2},t_n)-e_{yz}(\mathbf{x}_s,\mathbf{x}_{i,\,j-1/2,k+1/2},t_n)\Big)\Big]\end{aligned}\,,$$

$$\begin{aligned}\mathrm{f}^{v,\mathrm{DAF}}_{s,i,j,k,z}(\mathbf{x}_{i,\,j,k-1/2},t_n)=&\,a_1\frac{V_{\mathrm{p}}(\mathbf{x}_{i,j,k})}{dz}e_{nn}(\mathbf{x}_s,\mathbf{x}_{i,j,k},t_n)+a_2\frac{1}{2}\frac{1}{V_{\mathrm{p}}(\mathbf{x}_{i,j,k-1/2})}\mathrm{a}_z(\mathbf{x}_s,\mathbf{x}_{i,j,k-1/2},t_n)\\&-2a_1\left(\frac{1-2\sigma}{2-2\sigma}\right)\frac{V_{\mathrm{p}}(\mathbf{x}_{i,j,k})}{dz}\Big[e_{nn}(\mathbf{x}_s,\mathbf{x}_{i,j,k},t_n)-e_{zz}(\mathbf{x}_s,\mathbf{x}_{i,j,k},t_n)\\&-\frac{1}{4}\Big(e_{xz}(\mathbf{x}_s,\mathbf{x}_{i,\,j+1/2,k-1/2},t_n)-e_{xz}(\mathbf{x}_s,\mathbf{x}_{i,\,j-1/2,k-1/2},t_n)\Big)\\&-\frac{1}{4}\Big(e_{yz}(\mathbf{x}_s,\mathbf{x}_{i,\,j+1/2,k-1/2},t_n)-e_{yz}(\mathbf{x}_s,\mathbf{x}_{i,\,j-1/2,k-1/2},t_n)\Big)\Big]\end{aligned}\,,$$

$$\mathrm{f}^{v,\mathrm{DAF}}_{s,i,j,k,z}(\mathbf{x}_{i-1/2,j,k-1/2},t_n)=2a_1\left(\frac{1-2\sigma}{2-2\sigma}\right)\frac{V_\mathrm{p}(\mathbf{x}_{i,j,k})}{4dz}e_{xz}(\mathbf{x}_s,\mathbf{x}_{i-1/2,j,k-1/2},t_n),$$

$$\mathrm{f}^{v,\mathrm{DAF}}_{s,i,j,k,z}(\mathbf{x}_{i-1/2,j,k+1/2},t_n)=2a_1\left(\frac{1-2\sigma}{2-2\sigma}\right)\frac{V_\mathrm{p}(\mathbf{x}_{i,j,k})}{4dz}e_{xz}(\mathbf{x}_s,\mathbf{x}_{i-1/2,j,k+1/2},t_n),$$

$$\mathrm{f}^{v,\mathrm{DAF}}_{s,i,j,k,z}(\mathbf{x}_{i+1/2,j,k-1/2},t_n)=-2a_1\left(\frac{1-2\sigma}{2-2\sigma}\right)\frac{V_\mathrm{p}(\mathbf{x}_{i,j,k})}{4dz}e_{xz}(\mathbf{x}_s,\mathbf{x}_{i+1/2,j,k-1/2},t_n),$$

$$\mathrm{f}^{v,\mathrm{DAF}}_{s,i,j,k,z}(\mathbf{x}_{i+1/2,j,k+1/2},t_n)=-2a_1\left(\frac{1-2\sigma}{2-2\sigma}\right)\frac{V_\mathrm{p}(\mathbf{x}_{i,j,k})}{4dz}e_{xz}(\mathbf{x}_s,\mathbf{x}_{i+1/2,j,k+1/2},t_n),$$

$$\mathrm{f}^{v,\mathrm{DAF}}_{s,i,j,k,z}(\mathbf{x}_{i,j-1/2,k-1/2},t_n)=2a_1\left(\frac{1-2\sigma}{2-2\sigma}\right)\frac{V_\mathrm{p}(\mathbf{x}_{i,j,k})}{4dz}e_{yz}(\mathbf{x}_s,\mathbf{x}_{i,j-1/2,k-1/2},t_n),$$

$$\mathrm{f}^{v,\mathrm{DAF}}_{s,i,j,k,z}(\mathbf{x}_{i,j-1/2,k+1/2},t_n)=2a_1\left(\frac{1-2\sigma}{2-2\sigma}\right)\frac{V_\mathrm{p}(\mathbf{x}_{i,j,k})}{4dz}e_{yz}(\mathbf{x}_s,\mathbf{x}_{i,j-1/2,k+1/2},t_n),$$

$$\mathrm{f}^{v,\mathrm{DAF}}_{s,i,j,k,z}(\mathbf{x}_{i,j+1/2,k-1/2},t_n)=-2a_1\left(\frac{1-2\sigma}{2-2\sigma}\right)\frac{V_\mathrm{p}(\mathbf{x}_{i,j,k})}{4dz}e_{yz}(\mathbf{x}_s,\mathbf{x}_{i,j+1/2,k-1/2},t_n),$$

$$\mathrm{f}^{v,\mathrm{DAF}}_{s,i,j,k,z}(\mathbf{x}_{i,j+1/2,k+1/2},t_n)=-2a_1\left(\frac{1-2\sigma}{2-2\sigma}\right)\frac{V_\mathrm{p}(\mathbf{x}_{i,j,k})}{4dz}e_{yz}(\mathbf{x}_s,\mathbf{x}_{i,j+1/2,k+1/2},t_n),$$

where

$$e_{xx}(\mathbf{x}_s,\mathbf{x}_{i,j,k},t_n)=\frac{u_x(\mathbf{x}_s,\mathbf{x}_{i+1/2,j,k},t_n)-u_x(\mathbf{x}_s,\mathbf{x}_{i-1/2,j,k},t_n)}{dx},$$

$$e_{yy}(\mathbf{x}_s,\mathbf{x}_{i,j,k},t_n)=\frac{u_y(\mathbf{x}_s,\mathbf{x}_{i,j+1/2,k},t_n)-u_y(\mathbf{x}_s,\mathbf{x}_{i,j-1/2,k},t_n)}{dy},$$

$$e_{zz}(\mathbf{x}_s,\mathbf{x}_{i,j,k},t_n)=\frac{u_z(\mathbf{x}_s,\mathbf{x}_{i,j,k+1/2},t_n)-u_z(\mathbf{x}_s,\mathbf{x}_{i,j,k-1/2},t_n)}{dz},$$

$$e_{xy}(\mathbf{x}_s,\mathbf{x}_{i+1/2,j+1/2,k},t_n)=\frac{1}{2}\left(\frac{u_x(\mathbf{x}_s,\mathbf{x}_{i+1/2,j+1,k},t_n)-u_x(\mathbf{x}_s,\mathbf{x}_{i+1/2,j,k},t_n)}{dy}+\frac{u_y(\mathbf{x}_s,\mathbf{x}_{i+1,j+1/2,k},t_n)-u_y(\mathbf{x}_s,\mathbf{x}_{i,j+1/2,k},t_n)}{dx}\right),$$

$$e_{xz}(\mathbf{x}_s,\mathbf{x}_{i+1/2,j,k+1/2},t_n)=\frac{1}{2}\left(\frac{u_x(\mathbf{x}_s,\mathbf{x}_{i+1/2,j,k+1},t_n)-u_x(\mathbf{x}_s,\mathbf{x}_{i+1/2,j,k},t_n)}{dz}+\frac{u_z(\mathbf{x}_s,\mathbf{x}_{i+1,j,k+1/2},t_n)-u_z(\mathbf{x}_s,\mathbf{x}_{i,j,k+1/2},t_n)}{dx}\right),$$

$$e_{yz}(\mathbf{x}_s,\mathbf{x}_{i,j+1/2,k+1/2},t_n)=\frac{1}{2}\left(\frac{u_y(\mathbf{x}_s,\mathbf{x}_{i,j+1/2,k+1},t_n)-u_y(\mathbf{x}_s,\mathbf{x}_{i,j+1/2,k},t_n)}{dz}+\frac{u_z(\mathbf{x}_s,\mathbf{x}_{i,j+1,k+1/2},t_n)-u_z(\mathbf{x}_s,\mathbf{x}_{i,j,k+1/2},t_n)}{dy}\right),$$

and

$$e_{nn}(\mathbf{x}_s,\mathbf{x}_{i,j,k},t_n)=e_{xx}(\mathbf{x}_s,\mathbf{x}_{i,j,k},t_n)+e_{yy}(\mathbf{x}_s,\mathbf{x}_{i,j,k},t_n)+e_{zz}(\mathbf{x}_s,\mathbf{x}_{i,j,k},t_n). \quad (3\text{-}4)$$

Note that the strain wavefields are computed by a centralized second-order scheme.

3.2.3. Computational requirements

Diffraction-angle filtering requires additional computational efforts to compute the spatial derivatives of the particle displacement and pressure wavefields. The computation of the modified virtual source for acoustic FWI is similar to that of the virtual source for elastic FWI. Table 3.2 shows the computational efforts to compute the gradient for one shot gather of the examples with different model dimensions. Implementation of diffraction-angle filtering requires about 1.5 times longer computational time compared with conventional FWI regardless of model dimension or data size. Implementation of diffraction-angle filtering leads to a significant increase in computational efforts. But still, it is obvious that diffraction-angle filtering is computationally attractive while sufficiently separating high- and low-wavenumber updates compared with other scattering-angle filtering techniques, which require transforms across the data and space domains, or the migration/demigration process for scale separation (which doubles the computational cost compared to conventional FWI).

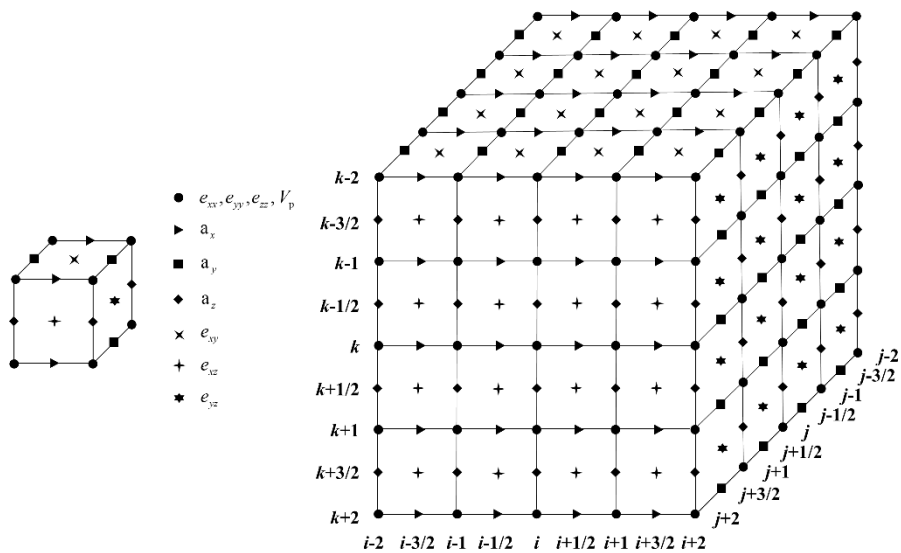

Fig. 3.9. Discretization of the 3D strain and particle acceleration wavefields on a staggered grid set to compute the modified virtual source in equation (3-2). The black circles are for the normal strains and velocities. The black triangles, squares and diamonds are for the particle accelerations in the x, y and z directions, respectively. The black crosses and stars are for the shear strains. Note that the strains and particle accelerations are defined at the same time step.

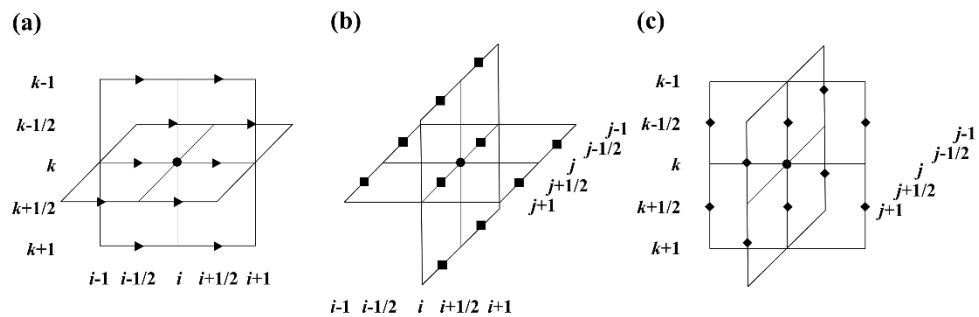

Fig. 3.10. Schematic diagram illustrating the location of the virtual source in equation (3-2) generated by the P-wave velocity at the nodal point (i, j, k) on a staggered grid set. The black circles indicate the P-wave velocity at the nodal point (i, j, k). The black triangles, squares and diamonds are for the virtual body-force sources in the (a) x, (b) y and (c) z directions, respectively.

Memory requirements for implementation of diffraction-angle filtering are slightly higher than those for conventional FWI. However, these additional requirements for diffraction-angle filtering is acceptable even in large 3D problems.

Table 3.2. Computational time and memory required to compute the gradient.

FWI			
Model dimension	Shot gather size	Time (s)	Memory (GB)
100 x 100 x 50	500 x 10000	144	2.2
200 x 200 x 100	1000 x 40000	954	7.3
300 x 300 x 150	1500 x 90000	2330	27.1

FWI with DAF			
Model dimension	Shot gather size	Time (s)	Memory (GB)
100 x 100 x 50	500 x 10000	216	2.3
200 x 200 x 100	1000 x 40000	1480	8.4
300 x 300 x 150	1500 x 90000	3629	32.2

3.3. Wavenumber characteristics of acoustic FWI gradient with diffraction-angle filtering

To investigate the wavenumber characteristics of the acoustic FWI gradient with diffraction-angle filtering, the acoustic FWI example in Section 3.1 is recalled. Fig. 3.11 shows the filtered versions of the gradients displayed in Figs. 3.3(b) and 3.5(b). In Figs. 3.11(a) and 3.11(b), modes II and III of diffraction-angle filtering emphasize the contributions of the low- and high-wavenumber components to the gradient, respectively. In Figs. 3.11(c) and 3.11(d), modes IV and V of diffraction-angle filtering additionally boost the low-wavenumber first Fresnel zone and high-wavenumber migration isochrone, respectively, with suppression of energy at intermediate diffraction angles. In particular, mode IV of diffraction-angle filtering in Fig. 3.11(c) suppresses most of the high-wavenumber components of the gradient and the first Fresnel zone is exclusively extracted, which enables the scale separation of the velocity into the macro velocity and reflectivity. In the case of the filtered gradients computed with the prior reflectivity information (Fig. 3.5b), mode IV of diffraction-angle filtering can extract not only the first Fresnel zone related to the diving wave, but also the pair of the first Fresnel zones related to the reflected wave, which is relatively weaker than the diving-wave-related first Fresnel zone or migration isochrone. Note that as the offset between the source and receiver increases, leakage of some parts of the migration isochrones related to large diffraction angles might occur.

The wavepaths of the reflected waves are different from those of the diving waves, which can provide the velocity update with complementary wavenumber

coverages that cannot be recovered by the diving waves alone. Note that the reflected waves can reach the deep target area with relatively short wavepaths compared with the diving waves, which are often vulnerable to cycle-skipping. Therefore, the use of the reflected waves can partially mitigate the cycle-skipping problem when reconstructing the targets in deep areas.

Next, a model with two reflectors in a linearly increasing background velocity is used to investigate the effect of diffraction-angle filtering on the gradient for a shot gather with the reflected waves (Fig. 3.12a). The initial model is the exact background velocity, and 40000 hydrophones are regularly deployed at the surface. In Fig. 3.12(b), as the reflection angle becomes larger (as the offset between the source and receiver increases or the depth of the reflector becomes shallower), the migration isochrone contains smoother low-wavenumber components. Note that modes II (Fig. 3.12c) and IV (Fig. 3.12e) boost the migration isochrones with large reflection angles, while modes III (Fig. 3.12d) and V (Fig. 3.12f) extract the migration isochrones related to reflection angles nearly 0°. In summary, diffraction-angle filtering not only extracts either the first Fresnel zones or migration isochrones, but also controls the contribution of the migration isochrones with reflection angles to the gradient. Based on these results, the nested algorithm with the diffraction-angle-filtering-based scale separation is designed, which will be described in the next Section.

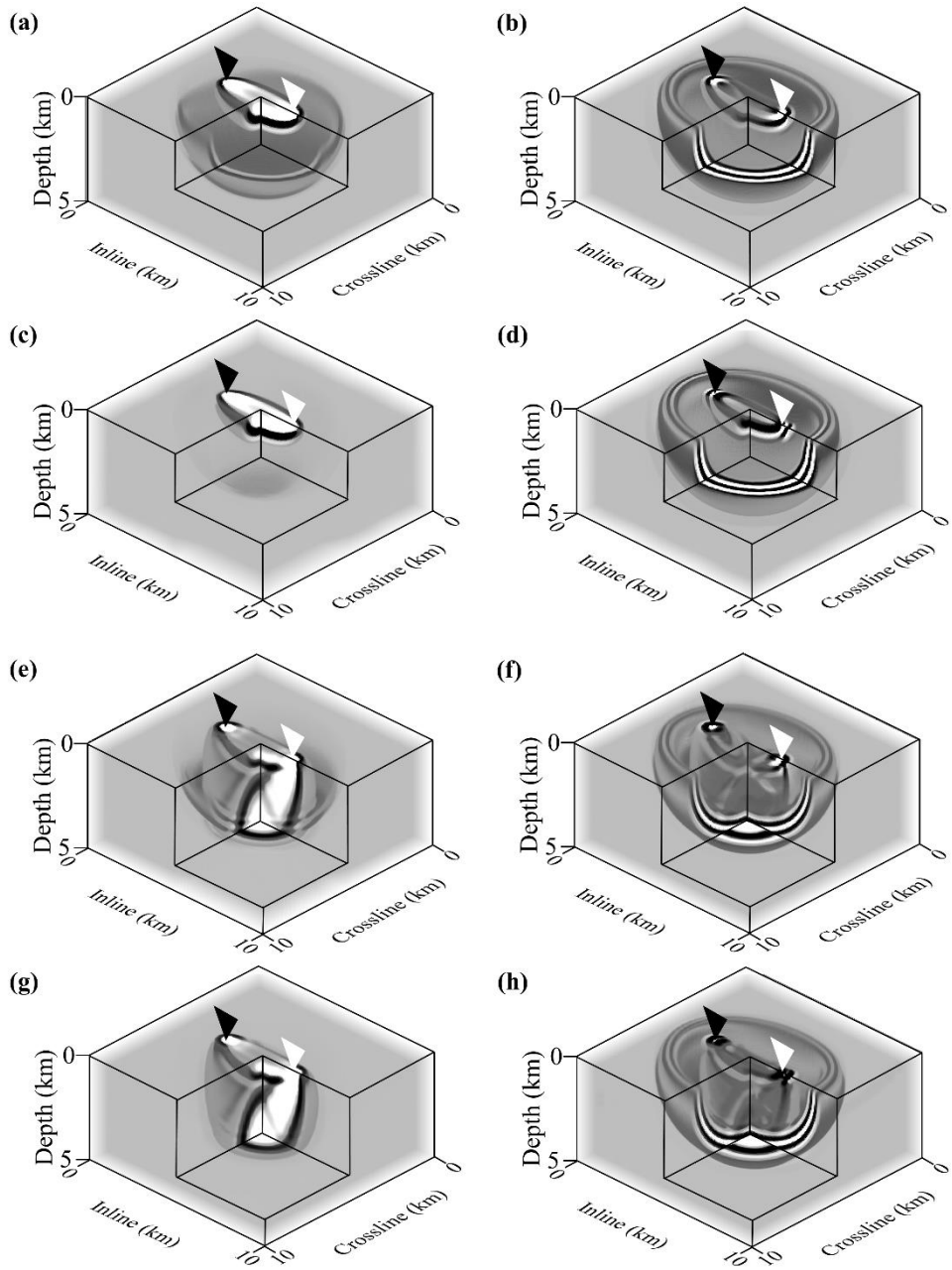

Fig. 3.11. Filtered versions of the gradients of Figs. 3.3(b) and 3.5(b) obtained by (a, e) mode II, (b, f) mode III, (c, g) mode IV and (d, h) mode V of diffraction-angle filtering.

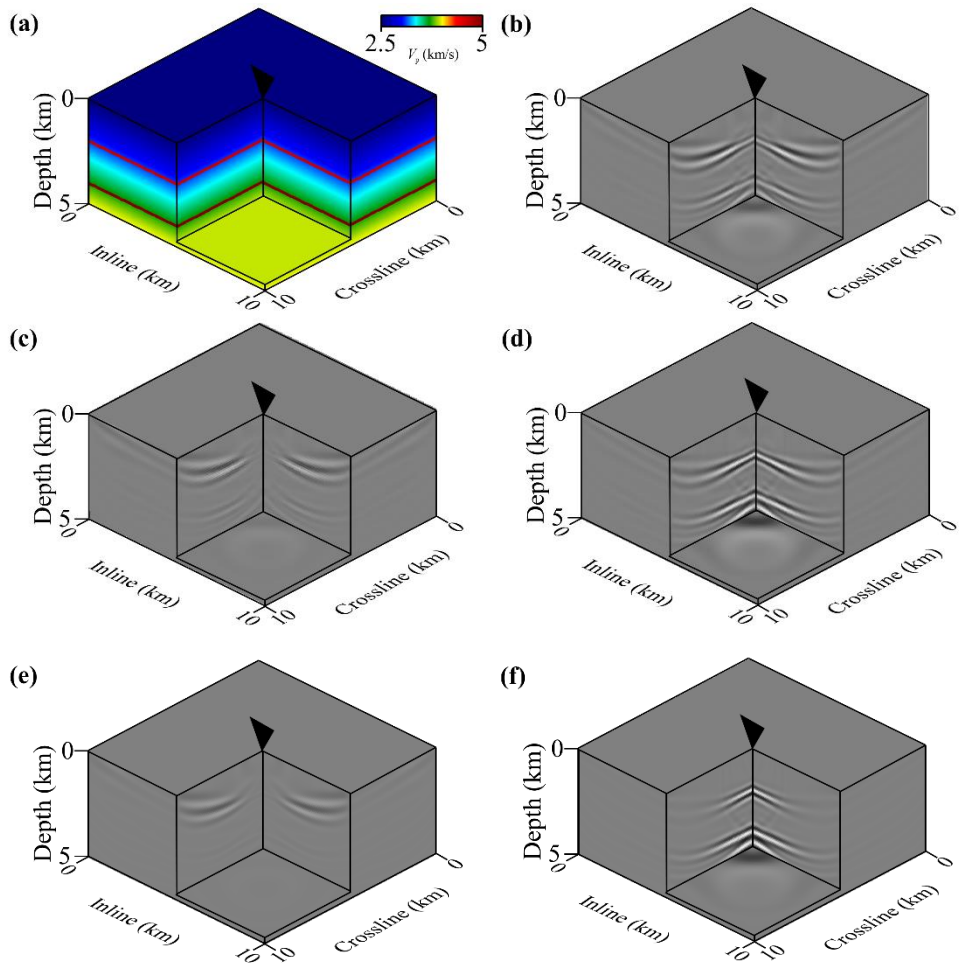

Fig. 3.12. (a) A two-reflector model. The gradients for a single shot gather filtered by (b) mode I, (c) mode II, (d) mode III, (e) mode IV and (f) mode V of diffraction-angle filtering. The black triangles indicate the location of seismic source.

3.4. Design of the diffraction-angle-filtering-based nested algorithm

The nested algorithm to mitigate non-linearity of acoustic FWI starts from the scale-separation of the P-wave velocity model into the background velocity and reflectivity models. The reflectivity model is first inverted starting from the given background velocity model. The prior reflectivity model is built at shallower (deeper) depths if the given background velocity model is slower (faster) than the true background velocity model. The prior reflectivity model generates reflections in the source and receiver wavefields, which leads to the additional low-wavenumber components of the FWI gradient along the wavepaths of the reflected waves. This low-wavenumber update from the reflected waves guides FWI to fit the mismatches of reflection moveout due to the inaccurate background velocity model so that the re-inverted reflectors starting from the updated background velocity model can be shifted to the correct positions. Then, the background velocity model can be reconstructed by the low-wavenumber components of the gradient along the wavepaths of both the diving and reflected waves. Gradual update of the P-wave velocity model from the background velocity model to the reflectivity model can partially mitigate the non-linearity of acoustic FWI. In the nested algorithm, the scale-separation of the velocity model update is performed by modes IV and V of diffraction-angle filtering instead of other techniques (e.g., the migration/demigration, up-/down-going wavefield separation, etc.), which can directly extract the low-wavenumber update along the full wavepaths.

During inversion of the prior reflectivity model, it is crucial to first invert

reflectivity by fitting the near-zero-offset (near-normal-incidence) data to preserve the zero-offset traveltimes and then subsequently match traveltimes at far-offset data (Brossier et al. 2015; Zhou et al. 2015; Wang et al. 2016; Chen et al. 2020; Yao et al. 2020). If the reflected waves were fitted over the entire offsets at the same time in a least-square sense starting from an inaccurate initial model, which is faster (slower) than the true velocity model, the two-way traveltimes of the reconstructed reflected waves at near offsets would be underestimated (overestimated) compared to those of the observed reflected waves like in Fig. 3.13(a) (Chen et al. 2020; Yao et al. 2020). In this case, the update direction related to the traveltime errors at near offsets is opposite to that related to the traveltime errors at far offsets, which makes FWI fall into local minima. On the other hand, if the reflected waves are preferentially fitted at the near offsets, then the update directions related to the traveltime errors at near offsets and far offsets are consistent. As mentioned in Section 3.3, mode V of diffraction-angle filtering boosts the contribution of near-normal-incidence reflection to the gradient (Fig. 3.12f). Therefore, mode V of diffraction-angle filtering is used to invert the reflectivity model to ensure the preferential updates related to normal-incidence reflection. Note that the direct waves are muted during reflectivity inversion to reject the secondary Fresnel zones related to the direct waves, and the post-critical reflections are excluded by using only near-to-intermediate offsets. Once the prior reflectivity model is reconstructed, mode IV of diffraction-angle filtering is used to extract the low-wavenumber components of the gradient along the wavepaths of the diving and reflected waves (Fig. 3.11g).

Then, the new gradients for the reflectivity (δV_{p}) and macro velocity (V_{p0})

model updates are defined as follows:

$$\frac{\partial E(V_{\mathrm{p0}}(\mathbf{x})+\delta V_{\mathrm{p}}(\mathbf{x}))}{\partial \delta V_{\mathrm{p}}(\mathbf{x}_{i,j,k})} = \sum_{s}\sum_{r}\sum_{t}\left[\mathbf{f}_{s,i,j,k}^{v,\mathrm{Mode\,V}}(\mathbf{x}_{i,j,k},\, t,\, V_{\mathrm{p0}}(\mathbf{x})+\delta V_{\mathrm{p}}(\mathbf{x}))\cdot \mathbf{a}_{s}^{b}(\mathbf{x}_{r},\, \mathbf{x}_{i,j,k},\, T-t,\, V_{\mathrm{p0}}(\mathbf{x})+\delta V_{\mathrm{p}}(\mathbf{x}))\right], \quad (3\text{-}5)$$

and

$$\frac{\partial E(V_{\mathrm{p0}}(\mathbf{x})+\delta V_{\mathrm{p}}(\mathbf{x}))}{\partial V_{\mathrm{p0}}(\mathbf{x}_{i,j,k})} = \sum_{s}\sum_{r}\sum_{t}\left[\mathbf{f}_{s,i,j,k}^{v,\mathrm{Mode\,IV}}(\mathbf{x}_{i,j,k},\, t,\, V_{\mathrm{p0}}(\mathbf{x})+\delta V_{\mathrm{p}}(\mathbf{x}))\cdot \mathbf{a}_{s}^{b}(\mathbf{x}_{r},\, \mathbf{x}_{i,j,k},\, T-t,\, V_{\mathrm{p0}}(\mathbf{x})+\delta V_{\mathrm{p}}(\mathbf{x}))\right], \quad (3\text{-}6)$$

where the superscripts “Mode IV” and “Mode V” indicate the virtual sources filtered by modes IV and V, respectively. Note that the only difference between equations (3-5) and (3-6) is the virtual source, which controls the diffraction patterns of the partial derivative wavefields as shown in Fig. 3.11.

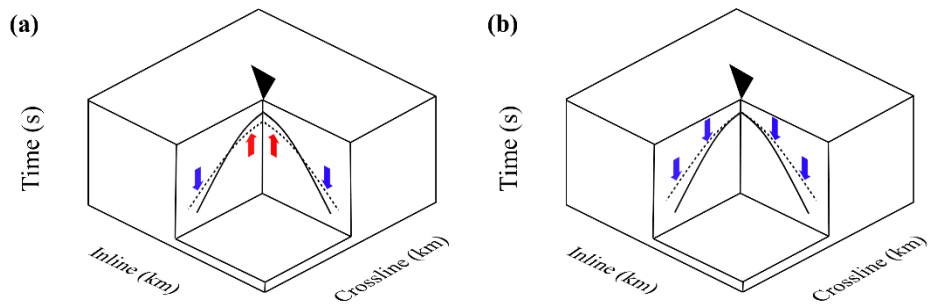

Fig. 3.13. Schematic diagrams illustrating the inverted reflected waves fitted (a) over the entire offsets at the same time and (b) at the near offsets intentionally. The black triangles indicate the location of the seismic source. The black bold and dotted hyperbolic lines indicate the 2D sections of the observed and computed reflected waves, respectively. The red and blue arrows denote the update directions that make the background velocity model faster and slower, respectively.

3.5. Workflow of the diffraction-angle-filtering-based nested algorithm

Workflow of the diffraction-angle-filtering-based nested algorithm consists of two inner loop and one outer loop as shown in Algorithm 3.1. Starting from the smooth background velocity V_{p0}^{i} in the ith iteration of the outer loop, the workflow begins with the first inner loop where δV_{p}^{i} is updated in the given background velocity V_{p0}^{i} by using equation (3-5). Inversion of δV_{p}^{i} can converge in a few iterations because it only needs to fit the amplitude errors. After δV_{p}^{i} is recovered, the gradient to update the background velocity V_{p0}^{i} is computed in the velocity model $V_{p0}^{i}+\delta V_{p}^{i}$ by using equation (3-6) in the second inner loop. Note that δV_{p}^{i} should provide accurate amplitude information of the reflected waves to avoid contribution of the high-wavenumber leakage caused by remaining amplitude errors in the reflected waves to the gradient during inversion of the background velocity. As the background velocity V_{p0}^{i} is updated by the gradients computed with equation (3-6), the two-way traveltimes of the normal-incidence reflection data must be adjusted for the newly updated background velocity so as to keep the consistency of the two-way traveltimes of the normal-incidence reflection data like in Fig. 3.13(b). Therefore, only a few iterations of the second inner loop are performed in the velocity model $V_{p0}^{i}+\delta V_{p}^{i}$. Note that the optimal number of iterations of the second inner loop is found empirically, which can make the significant low-wavenumber update. Then, the outer loop restarts from the smooth background velocity V_{p0}^{i+1}. In this manner, the nested algorithm is performed until the background velocity V_{p0}^{i} converges to the true background velocity.

Algorithm 3.1. Workflow of acoustic FWI with the DAF-based nested algorithm.

Input: Observed data P^o, initial background velocity model V_{p0}^0

Outer loop

First inner loop

Solve min $\delta V_p^i \quad E(V_{p0}^i + \delta V_p^i)$

Use velocity V_{p0}^i

Get gradient $\partial E(V_{p0}^i + \delta V_p^i)/\partial \delta V_p^i$ with mode V of DAF

Update δV_p^i

End first inner loop

Second inner loop

Solve min $V_{p0}^i \quad E(V_{p0}^i + \delta V_p^i)$

Use velocity $V_{p0}^i + \delta V_p^i$

Get gradient $\partial E(V_{p0}^i + \delta V_p^i)/\partial V_{p0}^i$ with mode IV of DAF

Update V_{p0}^i

End second inner loop

Substitute $V_{p0}^i \leftarrow V_{p0}^{i+1}$ for next **outer loop**

Initialize $\delta V_p^i \leftarrow 0$

End outer loop

Output: Updated background velocity V_{p0}^N

Chapter 4. Application to synthetic data: 3D SEG/EAGE overthrust model

Kim et al. (2022) applied acoustic FWI with the diffraction-angle-filtering-based nested algorithm to the synthetic 2D pressure data to assess its performance (refer to Appendix B). In Chapter 4, the proposed nested algorithm is investigated for acoustic FWI of the 3D synthetic pressure data computed for the 3D SEG/EAGE overthrust model shown in Fig. 4.1 (Aminzadeh et al. 1997). While the dimension of the original model is 20 x 20 x 4.65 km^3, only a portion of the model, whose dimension is 10 x 10 x 5 km^3, is used for the test to avoid computational overburden. The water layer is added to describe marine seismic survey with ocean-bottom cable on the top of the extracted model. The extracted model includes the thrust faults, anticlines, monoclines and flat zones. A channel also exists at a depth of 3.25 km. The model has strong lateral and vertical velocity variations, and thus FWI of the synthetic pressure data computed for the model might fall into local minima without a kinematically accurate initial background velocity model. 3D acoustic FWI with the proposed nested algorithm can recover the low-wavenumber structures of the model along the wavepaths of the diving and reflected waves even for highly complex velocity structures. The reconstructed background velocity by the proposed algorithm can be used as a new initial background velocity model for the subsequent FWI stage. The modeling and inversion parameters for the synthetic pressure data are provided in Section 4.1. Inversion results are described in Section 4.2. The inverted models are displayed by the Voxler of Golden Software Inc.

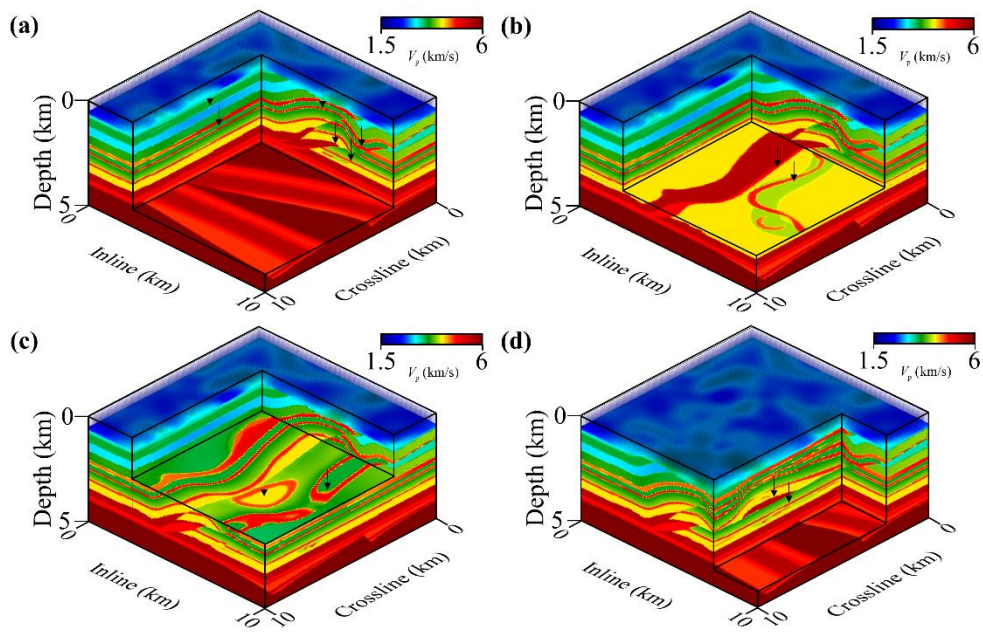

Fig. 4.1. The true 3D SEG/EAGE overthrust P-wave velocity model. The inline and crossline vertical slices and the horizontal slices are extracted at (inline, crossline, depth) = (a) (2.5, 2.5, 4.25) km, (b) (2.5, 2.5, 3.25) km, (c) (2.5, 2.5, 2) km and (d) (7.5, 2.5, 4.25) km. The black arrows indicate the part that we should pay attention to when comparing inversion results.

4.1. Modeling and inversion parameters

The model is discretized by 200 x 200 x 100 grid points with a grid interval of 50 m. A total of 40000 pressure sources are assumed to be excited at a depth of 50 m; and 180 receivers are deployed with an inline interval of 500 m and a crossline interval of 1 km over the whole area. The source-receiver reciprocity theorem is used to reduce computational efforts (i.e., the receiver gathers are regarded as the shot gathers during modeling and inversion). For the source wavelet function, the Ricker wavelet with a peak frequency of 5 Hz is used. The total recording length is 5 s. Then, the Butterworth filter with a bandwidth of 3 – 9 Hz is applied to the synthetic observed data. Note that unrealistic low-frequency components in the source wavelet is excluded during inversion. Fig. 4.2 shows a representative receiver gather at a distance of 1.75 km along the inline direction, and a distance of 2 km along the crossline direction. In the receiver gather, the refracted waves are observed at far offsets (outside the yellow dotted box) due to the wide-aperture/long-offset acquisition geometry, and thus the contribution of the refracted and diving waves to the low-wavenumber updates dominates that of the reflected waves to the low-wavenumber updates during inversion with the nested algorithm without the data scaling techniques. One can design the time-offset window to intentionally emphasize the short-spread reflection data (Zhou et al. 2015). However, in this thesis, a simple offset-selection strategy is used to balance the contribution of the reflected waves to the low-wavenumber updates. In this synthetic case, the nested algorithm is applied to the near-to-intermediate-offset data (<6 km; inside the yellow dotted box). It is assumed that the source wavelet function is known. The initial velocity

model is a linearly-increasing 1D P-wave velocity model as shown in Fig. 4.3(a), which cannot describe the macro variations of the model. Following the workflow described in Algorithm 3.1, the reflectivity model δV_{p} is updated in the first inner loop starting from the given background velocity model V_{p0} using the near-to-intermediate-offset data. The first inner loop is performed by 5 times for each background velocity model to ensure that the zero-offset reflectivity is completely inverted. Then, in the second inner loop, the low-wavenumber updates are computed in the velocity model $\delta V_{\mathrm{p}} + V_{\mathrm{p0}}$ using the intermediate-offset data (<6 km), which provides the wavepaths of the reflected waves. The second inner loop is performed by 5 times until the zero-offset reflectivity is re-inverted for the newly updated background velocity. A fixed step-length of 0.05 km/s is used during inversion for simplicity.

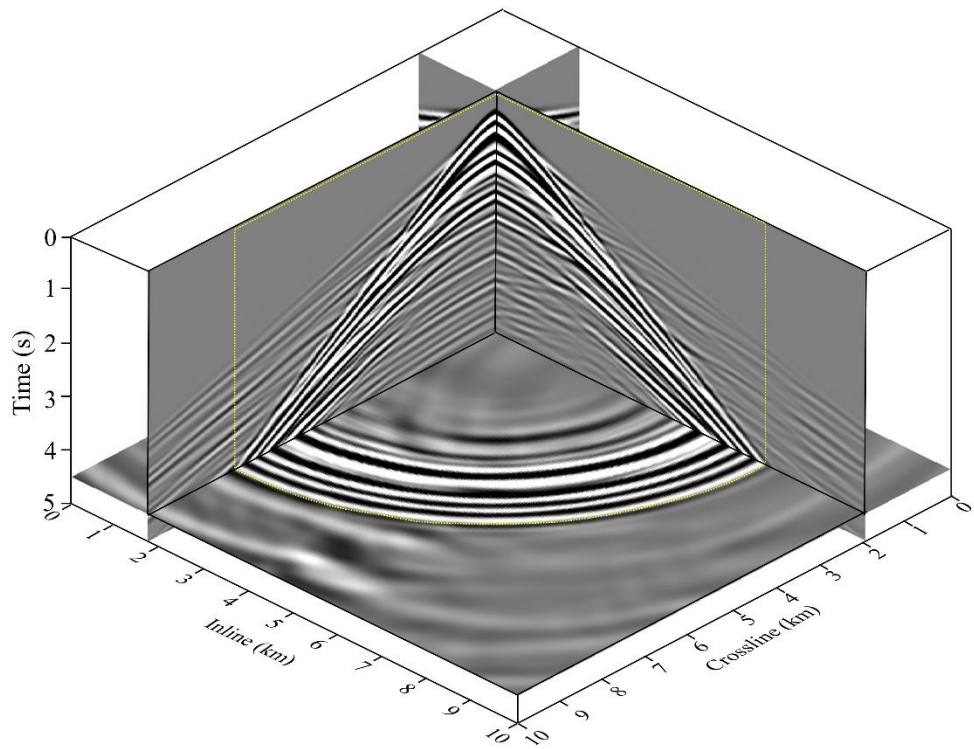

Fig. 4.2. A representative receiver gather at a distance of 1.75 km along the inline direction, and a distance of 2 km along the crossline direction. The time slice is extracted at 4.5 s. The yellow dotted box is used to indicate the near-to-intermediate-offset data (<6 km) used in the nested inversion algorithm.

4.2. Inversion results

In the first iteration of the outer loop, the reflectivity model $\delta V_{\mathrm{p}} + V_{\mathrm{p0}}$ is reconstructed starting from the initial velocity model shown in Fig. 4.3(a). Fig. 4.3(b) shows the reflectivity model $\delta V_{\mathrm{p}} + V_{\mathrm{p0}}$ inverted by using the near-normal-incidence reflections by mode V of diffraction-angle filtering. Note that the model is so complicated, that it cannot be completely described only with zero-offset reflectivity and inaccurate initial background velocity models. However, the reflectivity model can provide sufficient wavepaths of the reflected waves, which lead to the velocity update with wide wavenumber coverages. Figs. 4.3(c) and 4.3(d) show the background velocity models reconstructed by using conventional FWI filtered by mode IV after 40 iterations and FWI with the diffraction-angle-filtering-based nested algorithm after 8 iterations of the outer loop. Compared with the initial velocity model, the reconstructed background velocity models can briefly describe lateral and vertical velocity variations caused by heavily folded overthrust structures of sedimentary succession. However, the low-wavenumber update in conventional FWI filtered by mode IV is mainly derived by the diving waves, in which case the low-wavenumber update from the reflected waves is excluded. Figs. 4.4(a) and 4.4(b) show the velocity perturbations of the background velocity models in Figs. 4.3(c) and 4.3(d) from the initial velocity model, respectively. We can see that the update of FWI with the nested algorithm (Fig. 4.4b) is different from that of conventional FWI filtered by mode IV (Fig. 4.4a) because of the additional update along the wavepaths of the reflected waves.

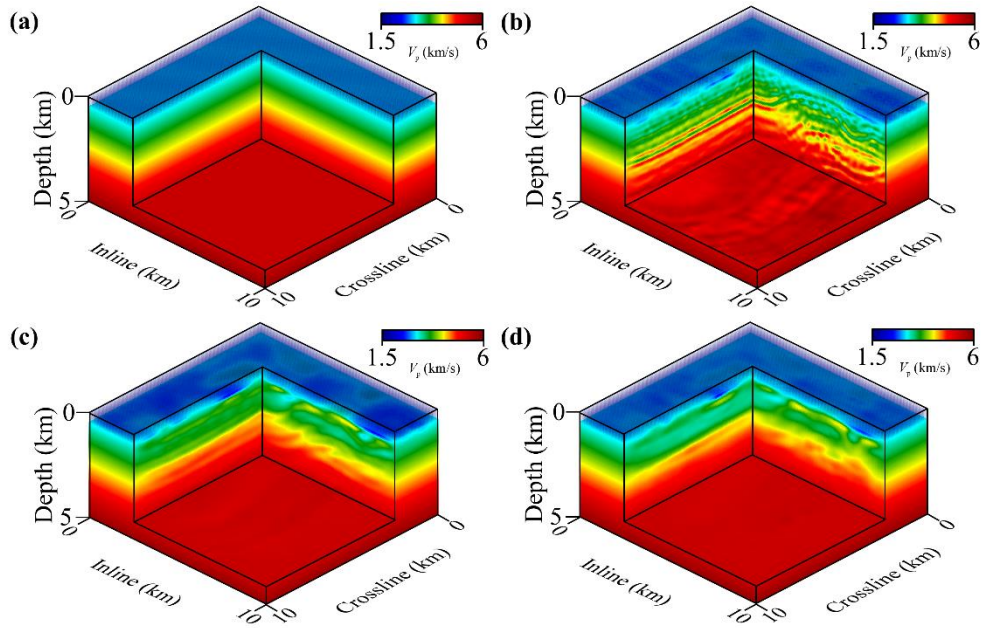

Fig. 4.3. (a) The linearly-increasing background velocity model used as an initial guess and (b) the reflectivity model $\delta V_{\mathrm{p}} + V_{\mathrm{p0}}$ recovered by using near-normal-incidence reflections by mode V of diffraction-angle filtering starting from the initial background velocity model. The background velocity models built by using (c) conventional FWI filtered by mode IV and (d) FWI with the diffraction-angle-filtering-based nested algorithm. The inline and crossline vertical slices and the horizontal slice are extracted at (inline, crossline, depth) = (2.5, 2.5, 4.25) km.

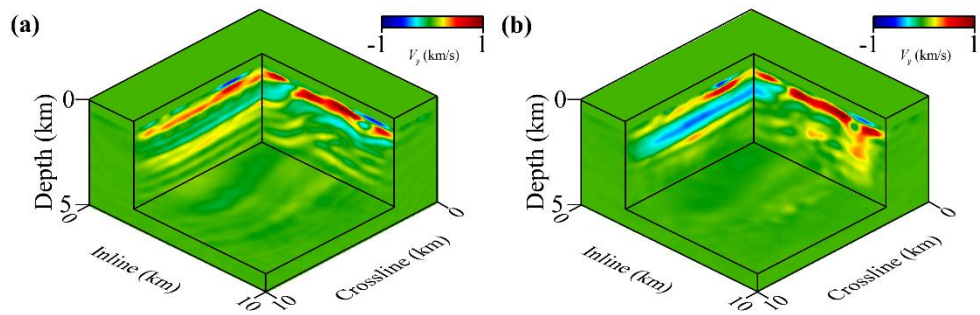

Fig. 4.4. The velocity perturbations of the background velocity models built by using (a) conventional FWI filtered by mode IV and (b) FWI with the diffraction-angle-filtering-based nested algorithm from the initial velocity model. The inline and crossline vertical slices and the horizontal slices are extracted at (inline, crossline, depth) = (2.5, 2.5, 4.25) km.

Next, I apply subsequent FWI starting from the reconstructed background velocity models. The results of subsequent FWI will demonstrate that the complementary low-wavenumber update along the reflection wavepaths not only updates the parts where the diving waves cannot reach, but also provides enhanced low-wavenumber update at the shallow parts, which allows subsequent FWI to converge toward the global minimum while recovering the intermediate-to-high-wavenumber subsurface structures.

The finally inverted velocity models starting from the background velocity models reconstructed by using conventional FWI with mode IV and FWI with the nested algorithm are shown in Fig. 4.5. For comparison, the true velocity model and conventional FWI result starting from the linearly-increasing initial velocity model are also displayed in Fig. 4.5. The inline and crossline vertical slices and the horizontal slices are extracted like in Fig. 4.1. Referring to the black arrows depicted in Fig. 4.1, the sediment layers at the flat zone (refer to the crossline vertical slices) and fault block generated by the two thrust faults (refer to the inline and crossline vertical slices) are clearly reconstructed at correct depths in the inverted velocity model starting from the background velocity built by using FWI with the nested algorithm. Syncline at a depth of 2 km and deep reflectors (at depths of 2.5 – 3.5 km) are well delineated (Figs. 4.5d, 4.5l and 4.5p). Compared with the result starting from the linearly-increasing initial velocity model, the interfaces corresponding to the sediment layers at the flat zone (refer to the crossline vertical slices in Fig. 4.5b) appear at deeper depths, because of the incomplete reconstruction of the thick low-velocity sediment layer at a depth of 1.5 km.

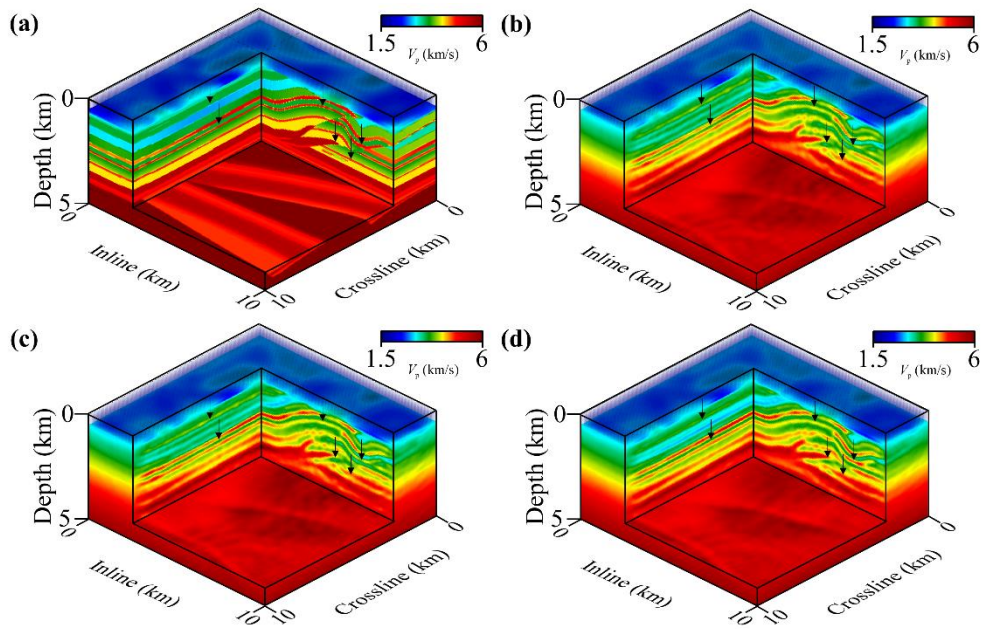

Fig. 4.5. (a, e, i, m) The true velocity model is displayed for comparison. The inverted velocity models starting from (b, f, j, n) the linearly-increasing velocity model and background velocity models reconstructed by using (c, g, k, o) conventional FWI filtered by mode IV and (d, h, l, p) FWI with the nested algorithm. The inline and crossline vertical slices and the horizontal slices are extracted at (inline, crossline, depth) = (a, b, c, d) (2.5, 2.5, 4.25) km, (e, f, g, h) (2.5, 2.5, 3.25) km, (i, j, k, l) (2.5, 2.5, 2) km and (g, h) (7.5, 2.5, 4.25) km.

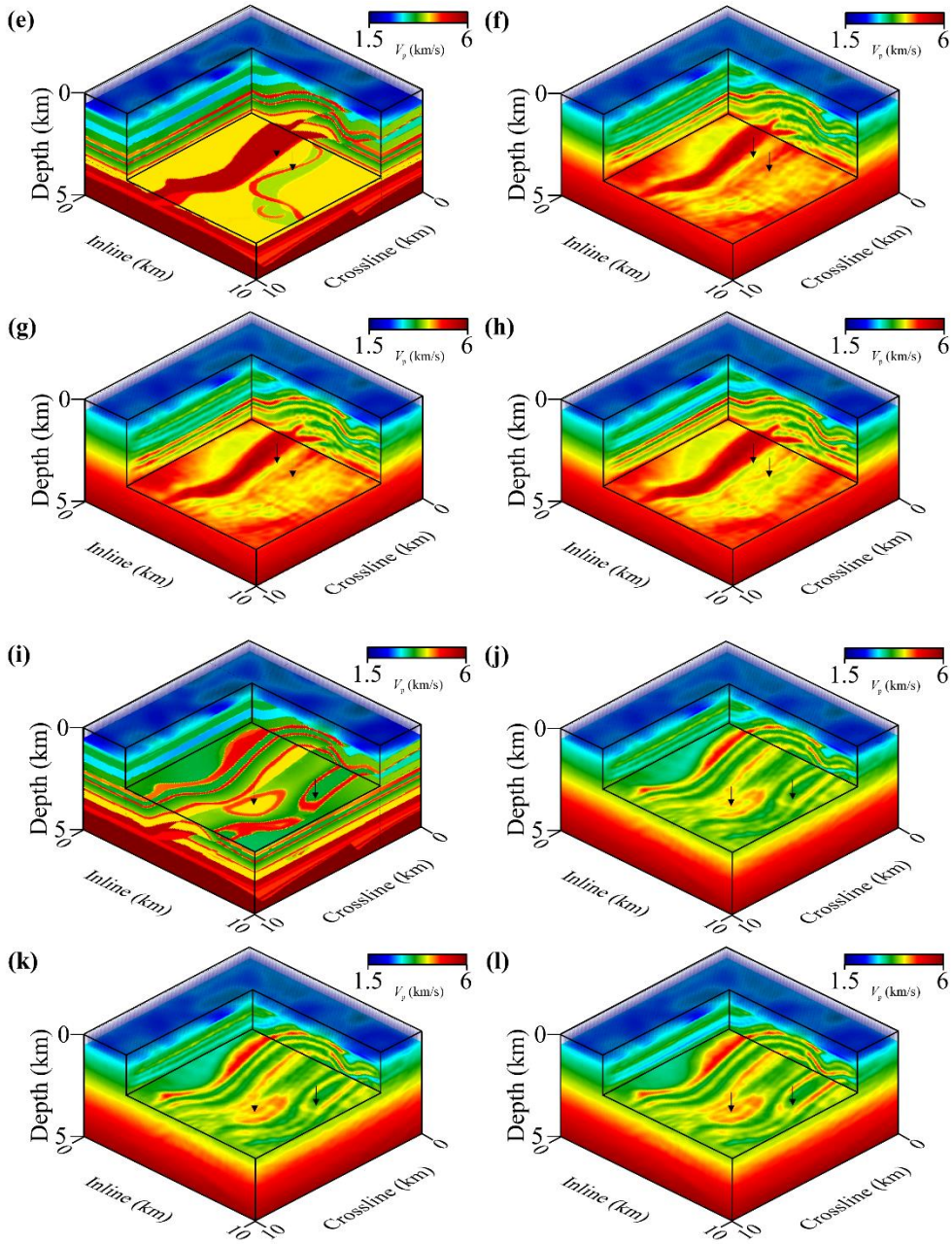

Fig. 4.5. (Continued)

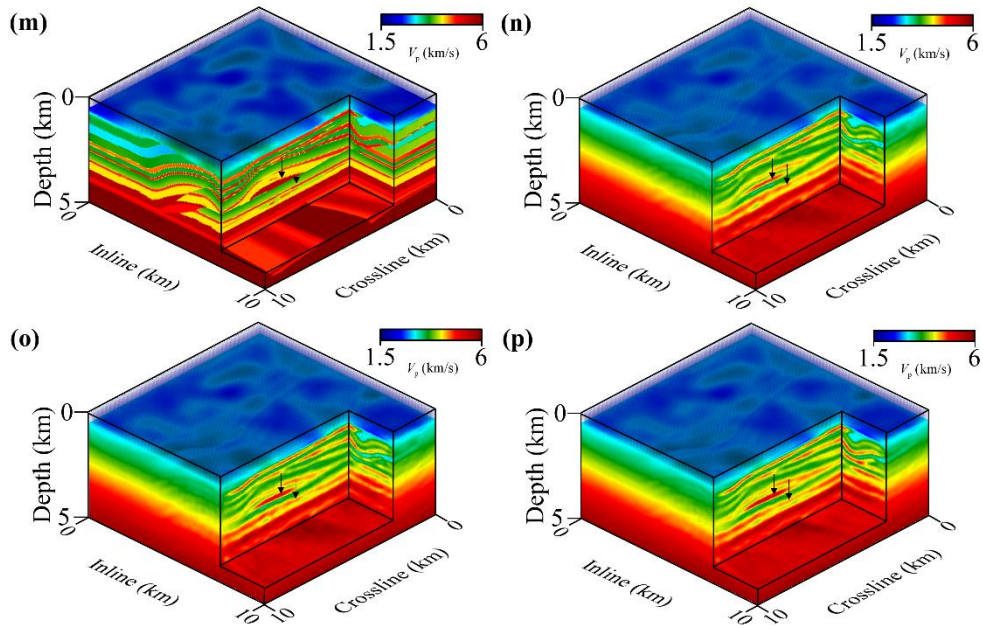

Fig. 4.5. (Continued)

Note that the reflectors are less focused and their amplitudes are also incompletely estimated if the macro velocity model cannot provide sufficiently accurate kinematic information (Figs. 4.5b, 4.5j and 4.5n). The fault block between the two thrust faults (refer to the inline vertical slices in Fig. 4.5b) appears slightly shallower than that in the result with the nested algorithm. The dipping angles of the two thrust faults are overestimated and the fault block is distorted due to the inaccurate background velocity information at depths of 1.5 – 3 km. Likewise, the imaged syncline and reflectors at depths of 2 – 3.5 km are hardly focused and located at slightly shallower depths than those in the true velocity model (Fig. 4.5b). The anticline and thrust faults can be a potential closed petroleum trap, and distortion of the fault block and folds caused by the thrust faults can lead to inaccurate evaluation of the reservoir. The depth errors caused by the inaccurate macro velocity model are more obvious in the horizontal slices than in the vertical slices. Compared with the conventional FWI result, 3D structures bounded by the folds and faults are clearly imaged at their correct positions, and the channel-related low-velocity zone appears broad in the result of FWI with the nested algorithm (Figs. 4.5f and 4.5h).

In the inverted velocity model starting from the background velocity model built by conventional FWI with mode IV, the reflectors are well focused at the shallow parts (Figs. 4.5k and 4.5o). However, the fault block is still distorted and reflectors at depths of 2 – 4 km are mispositioned (Figs. 4.5c, 4.5g and 4.5o) because of the incompletely reconstructed macro velocity structures. This implies that conventional FWI, which mainly relies on the diving waves and post-critical reflections to recover low-wavenumber structures, often fails to build a background

velocity model with full low-wavenumber coverage, while FWI with the nested algorithm, which allows the additional low-wavenumber update from the short-spread reflections, recovers a reliable background velocity model.

Fig. 4.6 shows the comparisons among the velocity profiles of the true velocity model and inverted velocity models in Fig. 4.5 for different locations. At all locations, the velocity profiles of FWI with the nested algorithm reasonably describe the vertical variations of the true velocity model. The comparisons among the data and model misfits of the inverted velocity models in Fig. 4.5 also demonstrate that FWI with the nested algorithm provides the most accurate velocity model (Fig. 4.7 and Table 4.1). Fig. 4.8 shows receiver gathers of the observed and computed data for the initial background velocity model and inverted velocity models in Fig. 4.5. The comparisons of the receiver gathers ensure that the velocity model reconstructed by FWI with the nested algorithm provides accurate amplitude and traveltime information of refractions and reflections, while conventional FWI, which mainly relies on the diving waves alone to build macro velocity structures, fails to fit traveltimes at the far offsets.

The results for the synthetic data convinces us that FWI with inaccurate initial background velocity might get stuck in local minima even for an ideal acoustic case (note that elastic effects are not considered in this synthetic case). However, the diffraction-angle-filtering-based nested algorithm can reconstruct the background velocity model that provides accurate traveltime information, which partially linearize FWI and enables subsequent FWI to converge to the global minimum even when the subsurface velocity model is highly complex.

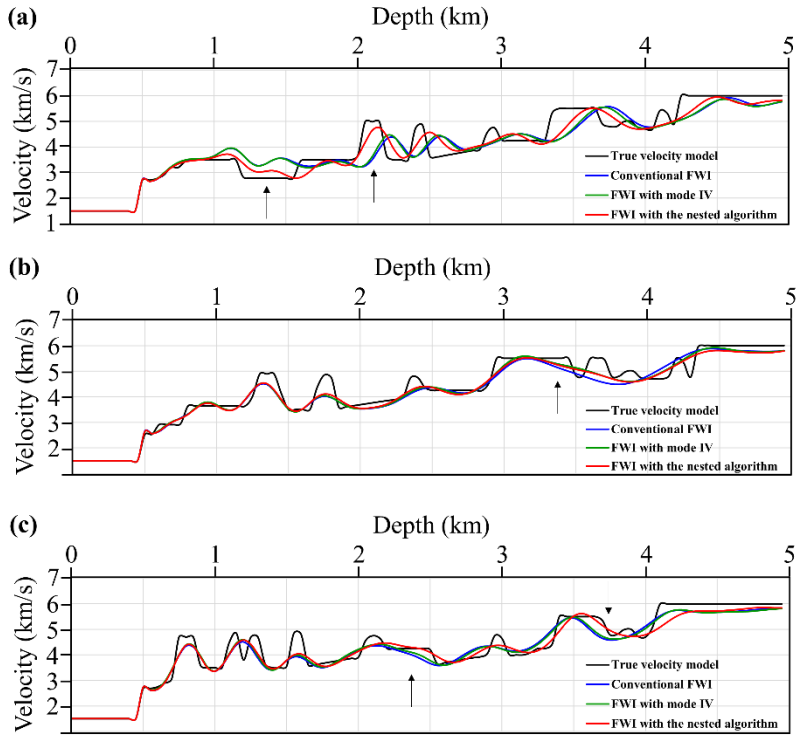

Fig. 4.6. Depth profiles of the true velocity model (the black lines) and inverted velocity models starting from the initial velocity model (the blue lines) and background velocity models reconstructed by using conventional FWI with mode IV (the green lines) and FWI with the nested algorithm (the red lines) at (inline, crossline) = (a) (2.5, 5) km, (b) (5, 5) km, (c) (7.5, 5) km.

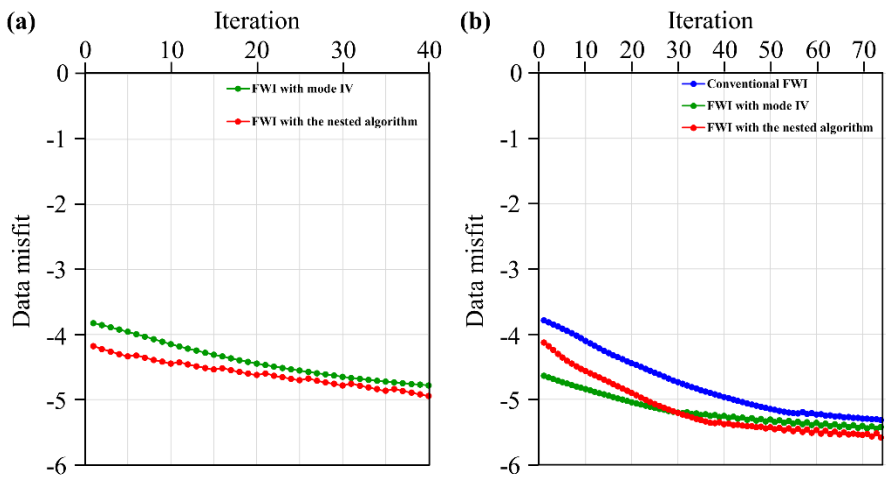

Fig. 4.7. (a) Data misfits for the background velocity models reconstructed by using conventional FWI with mode IV (the green line) and FWI with the nested algorithm (the red line). (b) Data misfits for the subsequently inverted velocity models starting from the initial velocity model (the blue line) and background velocity models reconstructed by using conventional FWI with mode IV (the green line) and FWI with the nested algorithm (the red line). The data misfits are plotted in a logarithm scale.

Table 4.1. Model misfits for the subsequently inverted velocity models starting from the initial velocity model and background velocity models reconstructed by using conventional FWI with mode IV and FWI with the nested algorithm.

	Model misfits
Velocity model	$\left\|\Delta V_{\mathrm{p}}\right\|^2$
Initial velocity model	1.286E+06
Conventional FWI	1.224E+06
FWI with mode IV	1.174E+06
FWI with the nested algorithm	1.013E+06

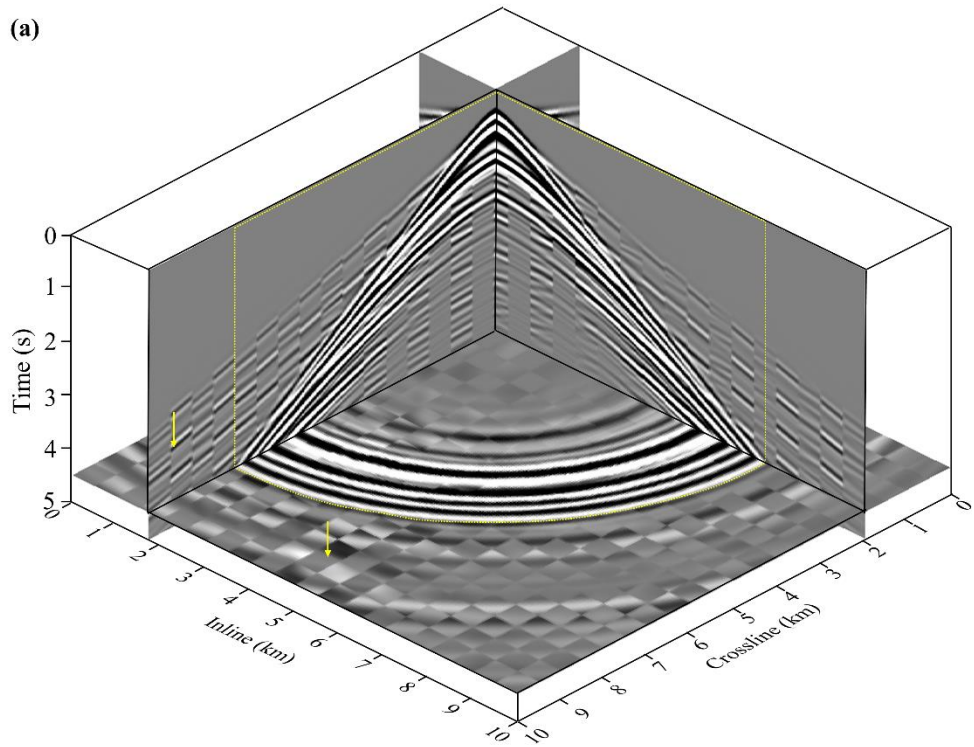

Fig. 4.8. Representative receiver gathers at a distance of 1.75 km along the inline direction, and a distance of 2 km along the crossline direction displayed by interweaving the observed data with the computed data for the (a) initial velocity model and inverted velocity models starting from the (b) initial velocity model and background velocity models reconstructed by using (c) conventional FWI with mode IV and (d) FWI with the nested algorithm every 10 x 10 traces. At the origin, the observed data are first shown followed by the computed data.

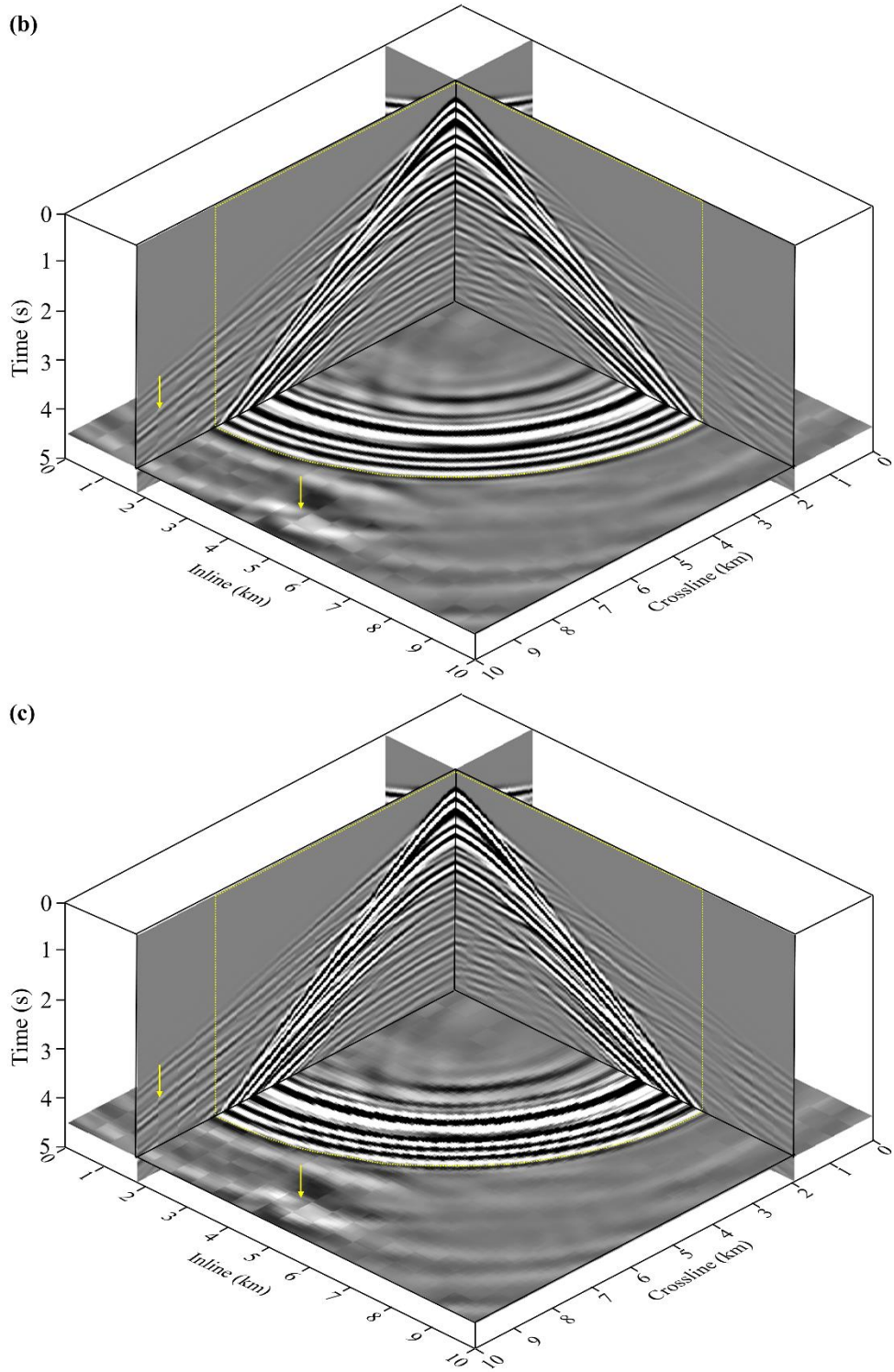

Fig. 4.8. (Continued)

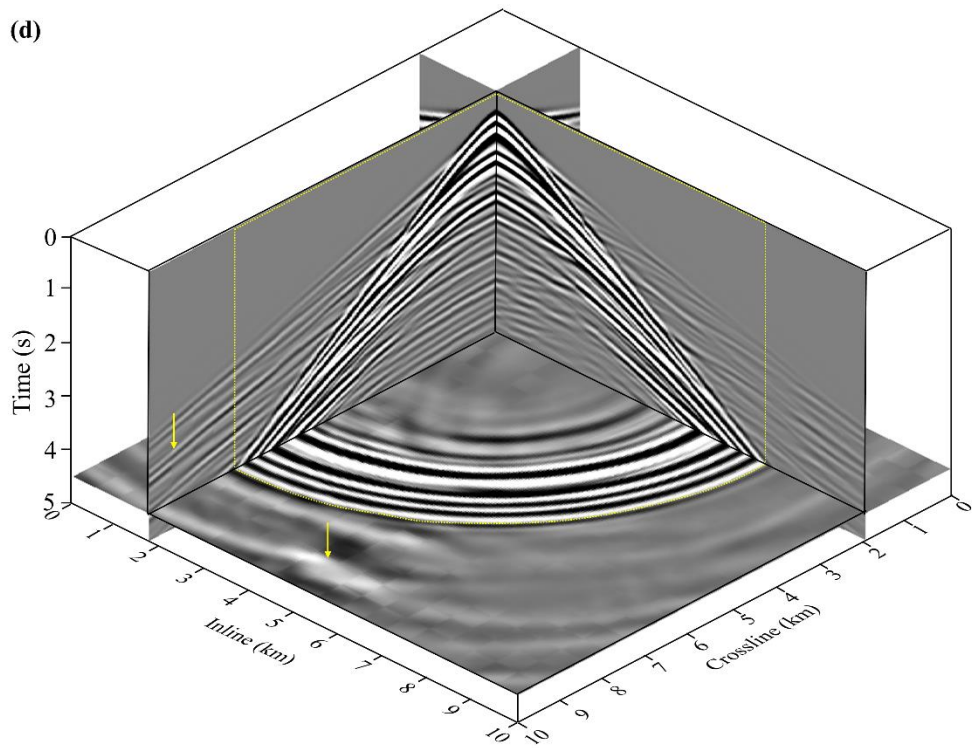

Fig. 4.8. (Continued)

Chapter 5. Application to field data: North Sea Volve oil field 3D OBC data

In Kim et al. (2022), acoustic FWI with the diffraction-angle-filtering-based nested algorithm is applied to the 2D line of the OBC data set acquired in the Volve oil field of the North Sea in 2002 (Szydlik et al. 2007; Fig. 5.1) to assess its applicability (refer to Appendix C). In Chapter 5, the performance and applicability of the proposed nested algorithm for acoustic FWI are examined by applying it to the 3D OBC data acquired in the Volve oil field, located in the North Sea (Szydlik et al. 2007). The preprocessed data (originally conducted in 2002) have officially been released by Equinor and its former Volve partners since October 2018. The field is characterized by a complex subchalk reservoir, which is a small dome-shaped structure (Szydlik et al. 2007; Fu et al. 2019; Singh et al. 2021). Considering the shot geometry of the field, the dimension of the subsurface velocity model for FWI is set to be 12.5 x 6.75 x 4.5 km^3. A 3D P-wave velocity model reconstructed by using layer-stripping-based reflection tomography and incorporating well log data have been released along with the OBC data (Fig. 5.2; Szydlik et al. 2007). The sonic log obtained in the oblique well displayed in Fig. 5.3 is also available for quality control. According to the reconstructed 3D S-wave velocity, anisotropy parameters ε and δ models released along with the 3D P-wave velocity model and the previous studies of FWI of Volve oil field OBC data (Szydlik et al. 2007; Guo and Alkhalifah 2017; Zhang and Alkhalifah 2017; Oh et al. 2018; Fu et al. 2019; Li et al. 2019; Li and Alkhalifah 2020; Singh et al. 2021), the inherent anisotropic and elastic

properties of subsurface media in the Volve oil field can seriously degrade the quality of acoustic FWI result. Because of the inaccurate approximations of physical behaviors of seismic data acquired in real seismic survey, acoustic FWI often generates artifacts or falls into local minima. To demonstrate that appropriate inversion strategies can enhance the background P-wave velocity obtained using 3D acoustic FWI even in case field data are affected by elasticity and anisotropy, acoustic FWI with the diffraction-angle-filtering-based nested algorithm is applied to the Volve oil field 3D OBC data. The inversion parameters and strategies for acoustic FWI of the OBC pressure data are described in Section 5.1. The inversion results are described in Section 5.2. Like in Chapter 4, the inverted models are displayed by the Voxler of Golden Software Inc.

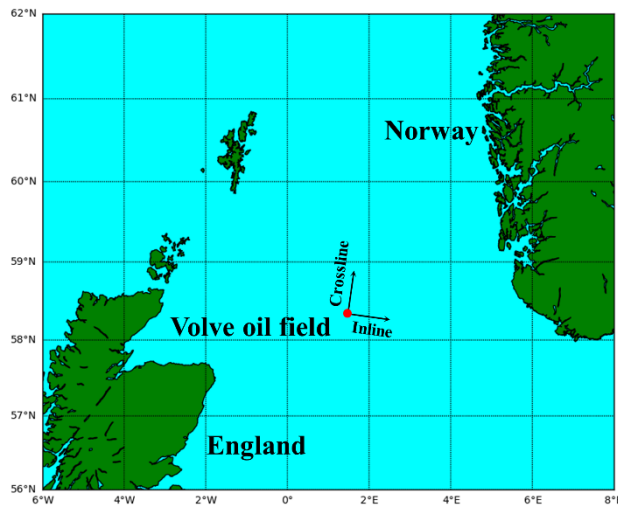

Fig. 5.1. Location of the Volve oil field in the North Sea.

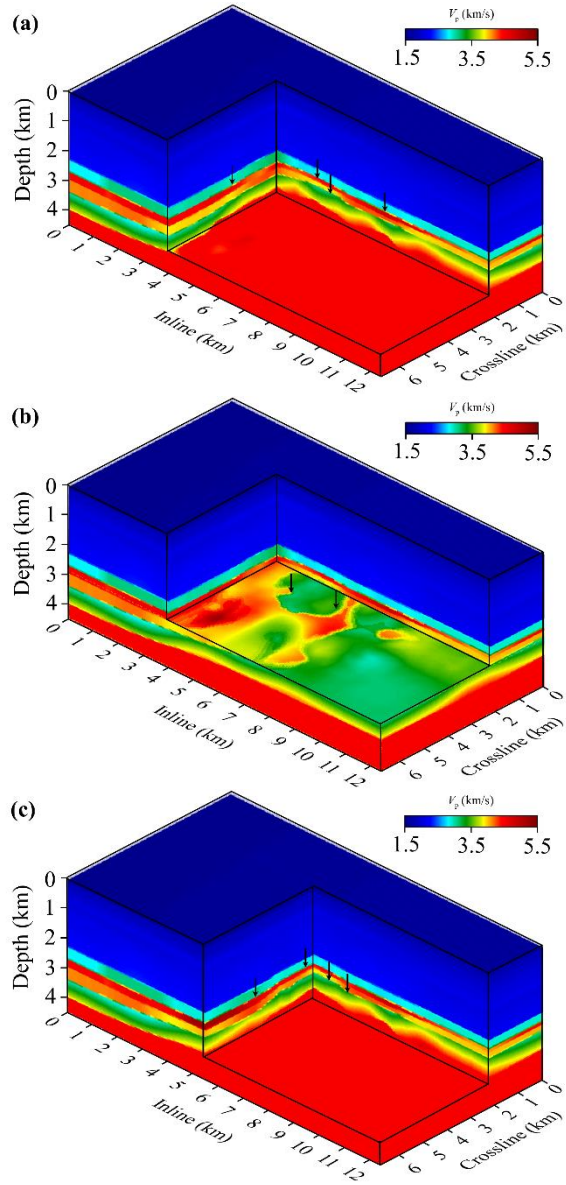

Fig. 5.2. The 3D P-wave velocity model reconstructed by reflection tomography for the Volve OBC data. The inline and crossline vertical slices and the horizontal slices are extracted at (inline, crossline, depth) = (a) (4, 2.25, 3.75) km, (b) (4, 2.25, 2.95) km and (c) (5.5, 2.25, 3.75) km. The black arrows indicate the part that we should pay attention to when comparing inversion results.

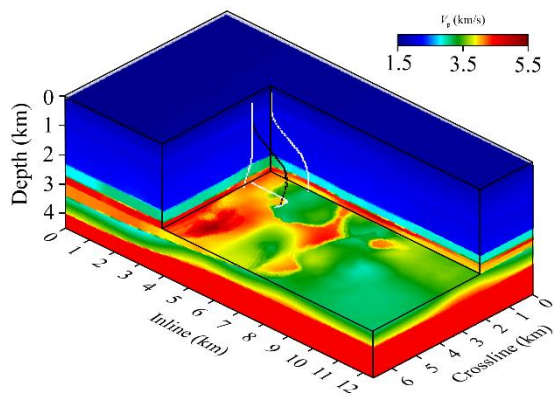

Fig. 5.3. The path of the oblique well in the Volve oil field for quality control. The black dots indicate the trajectory of the well. The white dots indicate the projection of the well onto the inline and crossline vertical slices and the horizontal slice extracted at (inline, crossline, depth) = (4, 2.25, 2.95) km.

5.1. Inversion parameters and strategies

The velocity model for inversion is discretized by 250 x 135 x 90 grid points with a grid interval of 50 m. A total of 12 parallel receiver cables are deployed at the sea bottom with an interval along the crossline direction of 400 m, and each cable consists of 240 receivers at an interval of 25 m along the inline direction. Although the water depth varies from 80 to 100 m, I assume a flat sea bottom with a water depth of 100 m. The pressure sources are excited by flip-flop shooting, whose intervals are 50 m and 25 m along the crossline inline directions, respectively. Note that the sources are assumed to be excited just below the sea surface, but there would be some errors in source positions due to the limitation of the grid interval. Like in Chapter 4, the source-receiver reciprocity theorem is used. Originally, a total of 2876 receivers were deployed over the whole area with intervals of 25 and 400 m along the inline and crossline directions, and among them 144 receivers are used for inversion in this study. The sources are resampled with an interval of 50 m and then the data are sorted to obtain the receiver gathers. Fig. 5.4 shows the locations of the receivers and sources with respect to the first receiver gather. Fig. 5.5(a) shows a representative receiver gather at distances of 4.8 and 3.25 km along the inline and crossline directions. The total recording length is 6 s. The Butterworth filter with a bandwidth of 2 − 5.5 Hz is applied to the data (Fig. 5.5b). Note that preferential use of low-frequency components mitigates the cycle-skipping problem of the least-squares-norm-based local optimization technique (Bunks et al. 1995; Sirgue and Pratt 2004; Virieux and Operto 2009). In the receiver gather (Fig. 5.5b), strong reflected waves are observed around 3 s, which seems to come from the subchalk

reservoir with an overlying seal rock. The source wavelet is estimated by the method described in Section 2.2.2.4. The direct waves at near offsets (<250 m) are used to estimate the source wavelet. The estimated source wavelet and its frequency spectrum are shown in Fig. 5.6. A 1D P-wave velocity model, which is generated from the sonic log obtained in the oblique well in Fig. 5.3, is used as an initial background velocity model (Fig. 5.7a). Following the workflow described in Algorithm 3.1, the reflectivity model δV_{p} is recovered using the near-to-intermediate-offset data with mode V of diffraction-angle filtering in the first inner loop starting from the given background velocity model V_{p0}. The first inner loop is iterated by 4 times for each background velocity model. In the second inner loop, the low-wavenumber updates are computed for the velocity model $\delta V_{\mathrm{p}} + V_{\mathrm{p0}}$ by using mode IV of diffraction-angle filtering. The second inner loop is iterated by 2 times until the zero-offset reflectivity is re-inverted for the newly updated background velocity. Like in Chapter 4, a fixed step-length of 0.05 km/s is used during inversion.

As addressed in the former studies of the Volve oil field, there are strong anisotropic effects at depths of 1 – 2.5 km and reservoir. According to Gholami et al. (2013), Oh and Alkhalifah (2016) and Feng and Schuster (2019), the amplitudes of the scattering patterns of the anisotropy parameters ε and δ are dependent on incident angles of the wavefield with respect to the perturbations of the anisotropy parameters. Because the amplitudes of the scattering patterns of ε are significant when incident angles are nearly 90° (which indicate the direct or diving waves), far-offset data (>5 km) are excluded (Fig. 5.5b) during inversion to mitigate the cross-talk effect between the P-wave velocity and ε. The updates of the background

velocity and detailed velocity structures then mainly rely on the reflected waves and the updates related to the direct and diving waves only provide supplementary information of macro structures at the shallow part in this case.

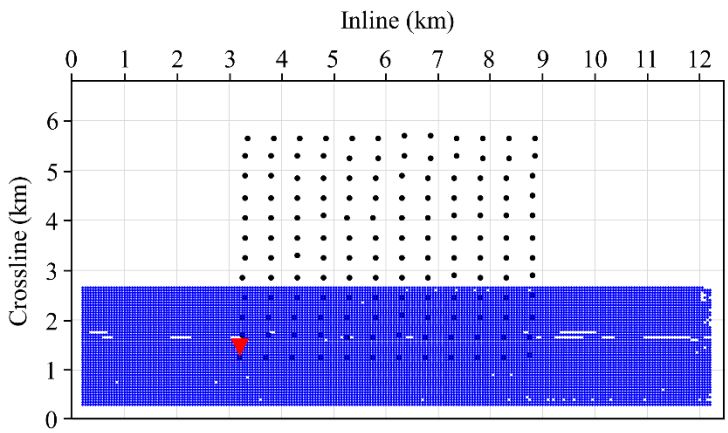

Fig. 5.4. Locations of receivers and sources for the first receiver gather. The black dots indicate the locations of receivers. The blue dots indicate the locations of sources used for the first receiver gather and the red triangle indicates the location of the first receiver.

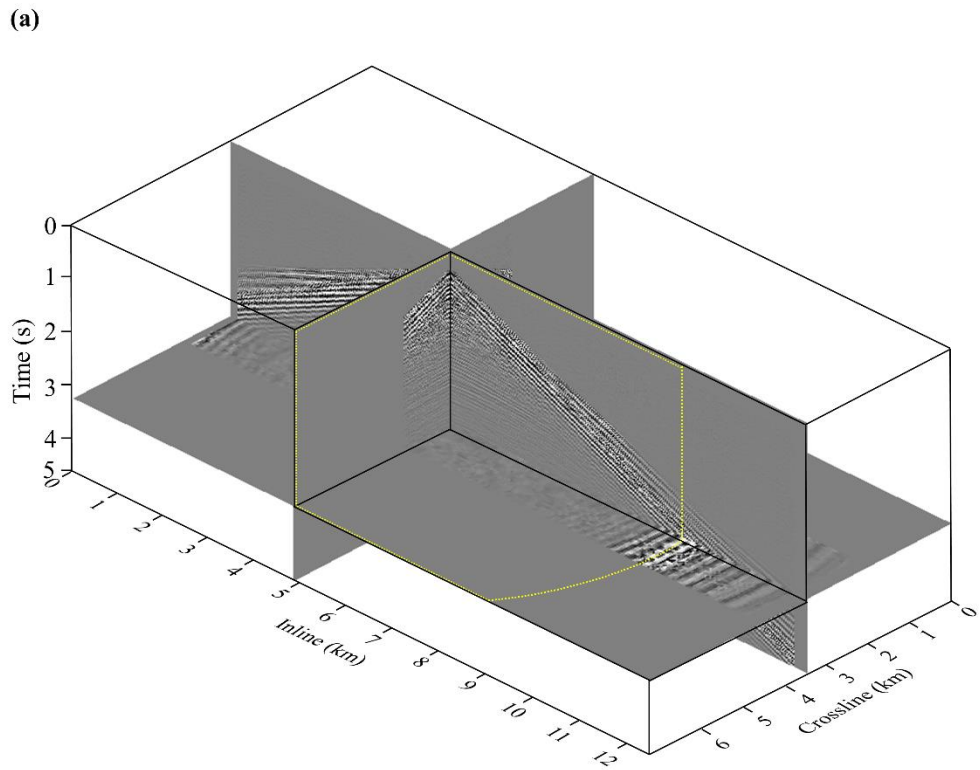

Fig. 5.5. (a) A representative receiver gather and (b) its bandpass-filtered version at distances of 4.8 and 3.25 km along the inline and crossline directions. The time slice is extracted at 4.2 s. The yellow dotted box is used to indicate the near-to-intermediate-offset data (<5 km) used in the nested inversion algorithm.

(b)

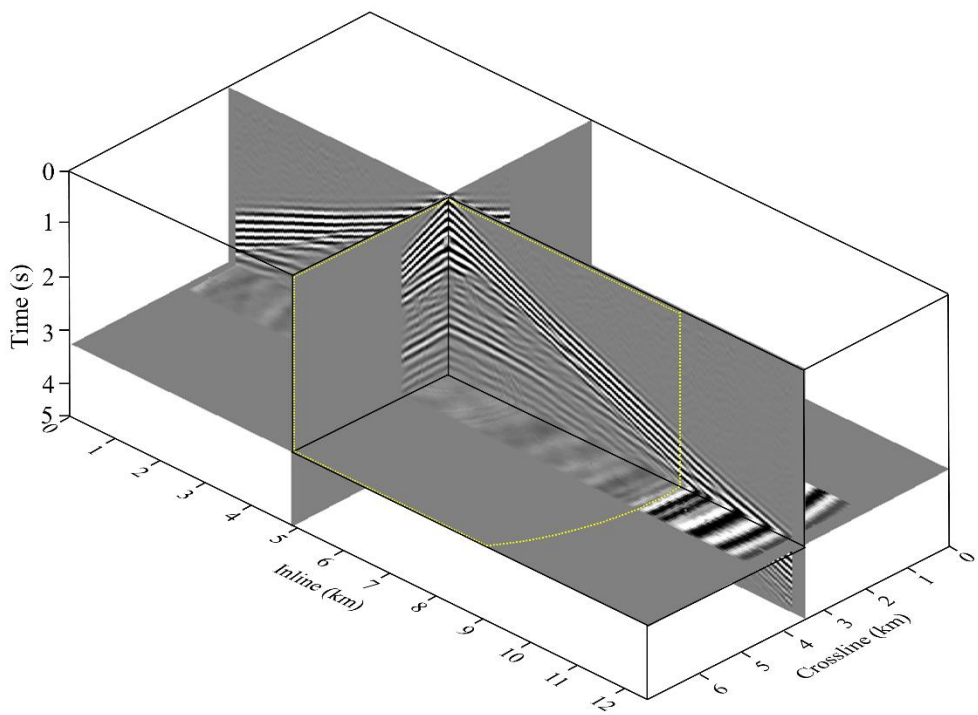

Fig. 5.5. (Continued)

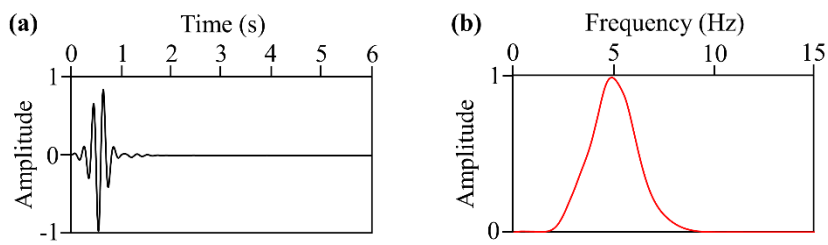

Fig. 5.6. (a) The estimated source wavelet and (b) its frequency spectrum.

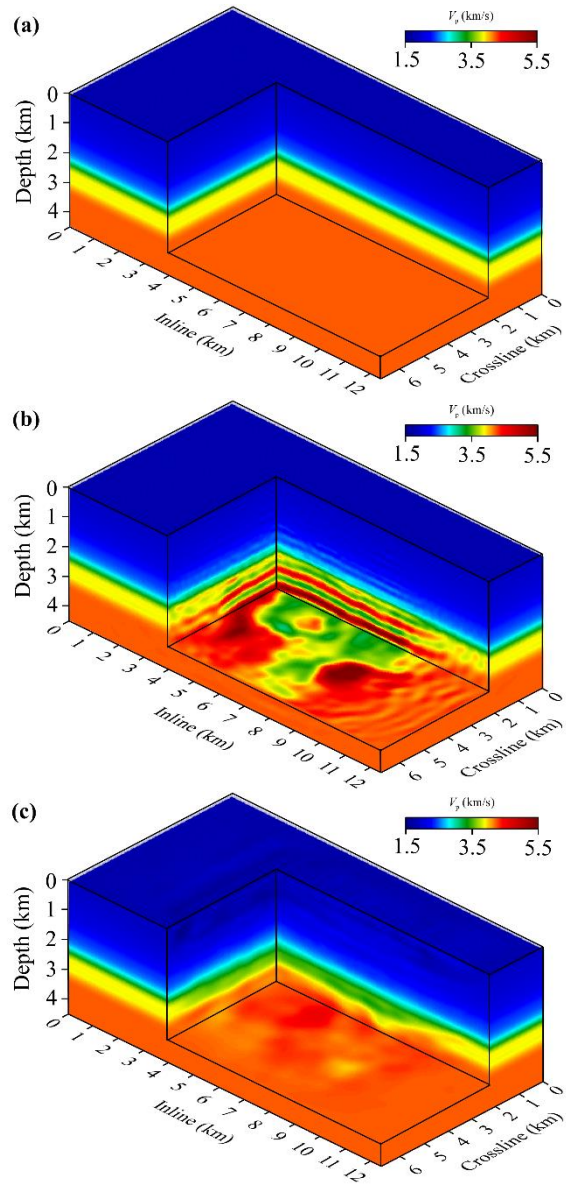

Fig. 5.7. (a) The 1D P-wave velocity model used as an initial guess. (b) The reflectivity model $\delta V_{\mathrm{p}} + V_{\mathrm{p0}}$ recovered by using near-normal-incidence reflections by mode V starting from the initial velocity model. (c) The background velocity model built by using FWI with the nested algorithm. The inline and crossline vertical slices and the horizontal slice are extracted at (inline, crossline, depth) = (4, 2.25, 3.75) km.

5.2. Inversion results

The reflectivity model $\delta V_{\mathrm{p}} + V_{\mathrm{p0}}$ inverted in the first iteration of the outer loop starting from the initial velocity model is shown in Fig. 5.7(b). The horizontal chalk layer appears at depths of 3 – 3.25 km, indicating the location of the reservoir. Note that the chalk layer is mispositioned at deeper depths than in the reference velocity model (Fig. 5.2). Then, the low-wavenumber updates along the wavepaths of the reflected waves generated by the seal rock will adjust the depths of the reservoir structures. Fig. 5.7(c) shows the reconstructed background velocity after 10 iterations of the outer loop of the nested algorithm. Compared with the initial velocity model, the velocities in the overburden at depths of 1.5 – 3 km decreased and the reconstructed background velocity model describes vertical velocity variations above the reservoir. Fig. 5.8 shows the velocity perturbation of the background velocity model in Fig. 5.7(c) from the initial velocity model. The update of FWI with the nested algorithm contains the low-wavenumber components at depths of 1.5 – 3 km, which are driven by the reflections generated from the seal rock. This enables inversion to update the macro structures of the deep target area while excluding the far-offset data. Note that the low-wavenumber components of the update for the reservoir structures are significant due to the large-scattering-angle-related migration isochrones and first Fresnel zones along the reflection wavepaths. At the shallow part, the update of the macro velocity structure is driven by the direct and diving waves.

Next, subsequent FWI is carried out using the background velocity model recovered by using FWI with the nested algorithm (Fig. 5.9) as an initial guess.

Subsequent FWI is carried out by using mode V of diffraction-angle filtering in this case to mainly fit the amplitudes of near-normal-incidence reflections, which is relatively free from the PS mode conversion. Fig. 5.9 shows the velocity model inverted by subsequent FWI. For comparison, the reference tomography velocity model in Fig. 5.2 and velocity model inverted by conventional FWI starting from the initial velocity model in Fig. 5.7(a) are displayed together in Fig. 5.9. The inline and crossline vertical slices and the horizontal slices are extracted like in Fig. 5.2. Note that subsequent FWI recovers the detailed reservoir structures and interfaces of the overburden, but it is difficult to trust the amplitudes and thicknesses of the reflectors because of the inaccurate approximations of physical behaviors in acoustic FWI. Therefore, I mainly focus on the positions of the interfaces rather than the quantitative values to examine the quality of the velocity model reconstructed by the diffraction-angle-filtering-based nested algorithm in this case. Referring to the black arrows depicted in Fig. 5.2, the interface of the seal rock is reconstructed at depths of 2.95 – 3 km in the result of conventional FWI starting from the inaccurate initial velocity model, which are deeper than their presumed depths (Figs. 5.9b and 5.9e). On the other hand, the reservoir structure imaged in the result of FWI with the nested algorithm is shifted to shallower depths, which are presumably its correct position (Figs. 5.9c and 5.9f). The imaged dome-shaped structure in Fig. 5.9(f), which is presumed as a reservoir, is located at its correct position referring to the tomography velocity model shown in Fig. 5.9(d).

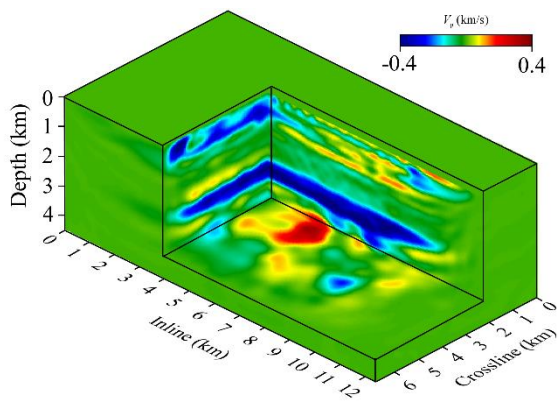

Fig. 5.8. The velocity perturbation of the background velocity model built by using FWI with the diffraction-angle-filtering-based nested algorithm from the initial velocity model. The inline and crossline vertical slices and the horizontal slice are extracted at (inline, crossline, depth) = (4, 2.25, 3.75) km.

The dome-shaped structure appears more clearly in the result of FWI with the nested algorithm compared with that obtained by conventional FWI starting from the initial model (Figs. 5.9h and 5.9i). Fig. 5.10 shows the comparisons among the velocity profiles of the well log, initial velocity model, background velocity model built by FWI with the nested algorithm, and finally inverted velocity models starting from the initial velocity model and background velocity model built by FWI with the nested algorithm along the well path shown in Fig. 5.3. FWI starting from the initial velocity model (the yellow line) locates the reservoir structures at wrong positions (the blue line). In contrast, the background velocity model reconstructed by FWI with the nested algorithm has slower velocities in the overburden (the green line). Accordingly, the result of FWI starting from the reconstructed background velocity model (the red line) matches well with the tendency of the well log and the chalk interface and reservoir structures are shifted to shallower depths. Note that there are still some mismatches at depths of 2.5 – 3 km because some of material properties such as elasticity and anisotropy are not considered, which will be discussed later.

For another quality control, angle-domain common-image gathers (ADCIGs; Sava and Fomel 2003) are computed for the result of FWI starting from the initial velocity model and background velocity model reconstructed by the nested algorithm (Fig. 5.11). Note that an inline profile of data is extracted at a distance of 3.65 km along the crossline direction to compute the ADCIGs. The reflection events in Fig. 5.11(b) are much flatter than those of Fig. 5.11(a), specifically the events at depths of 2.5 – 3 km (in the yellow dashed box in Fig. 5.11), which come from the chalk layer. However, because the vertical P-wave velocity is mainly recovered,

some events at large angles still smile upward, which might be attributed to anisotropy (indicated by the red arrows).

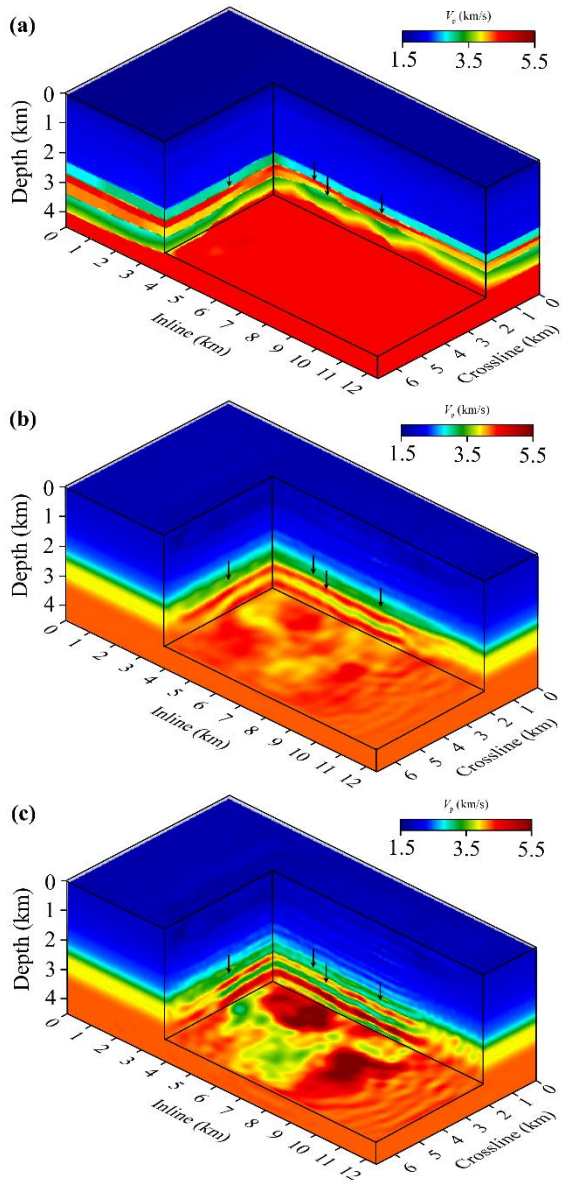

Fig. 5.9. (a, d, g) The true velocity model is displayed for comparison. The inverted velocity models starting from (b, e, h) the initial velocity model and (c, f, i) background velocity model reconstructed by using FWI with the nested algorithm. The inline and crossline vertical slices and the horizontal slices are extracted at (inline, crossline, depth) = (a, b, c) (4, 2.25, 3.75) km, (d, e, f) (4, 2.25, 2.95) km and (g, h, i) (5.5, 2.25, 3.75) km.

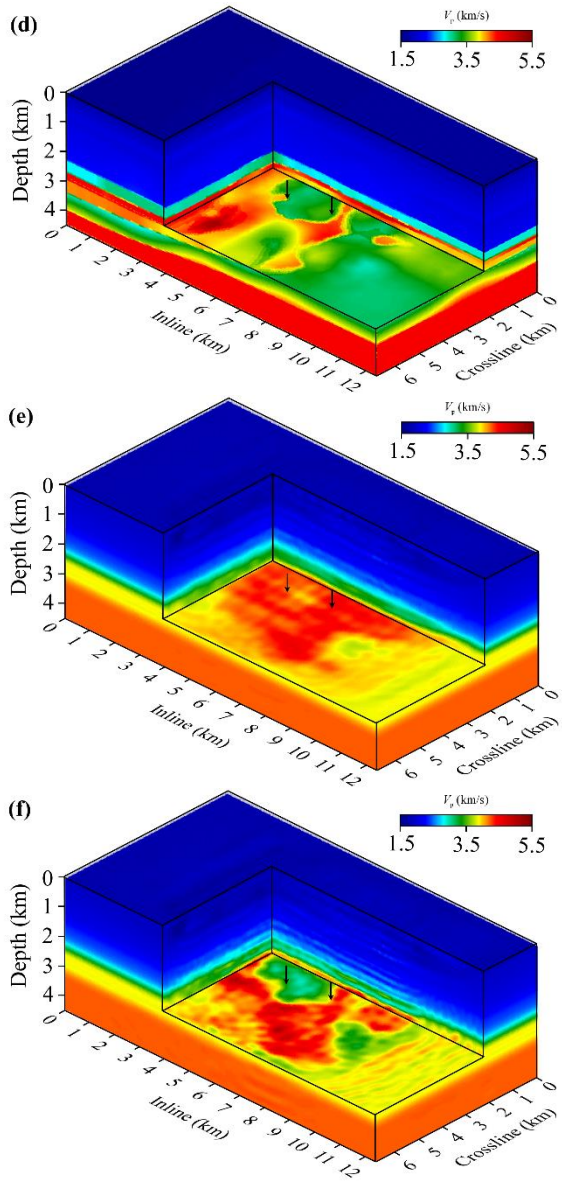

Fig. 5.9. (Continued)

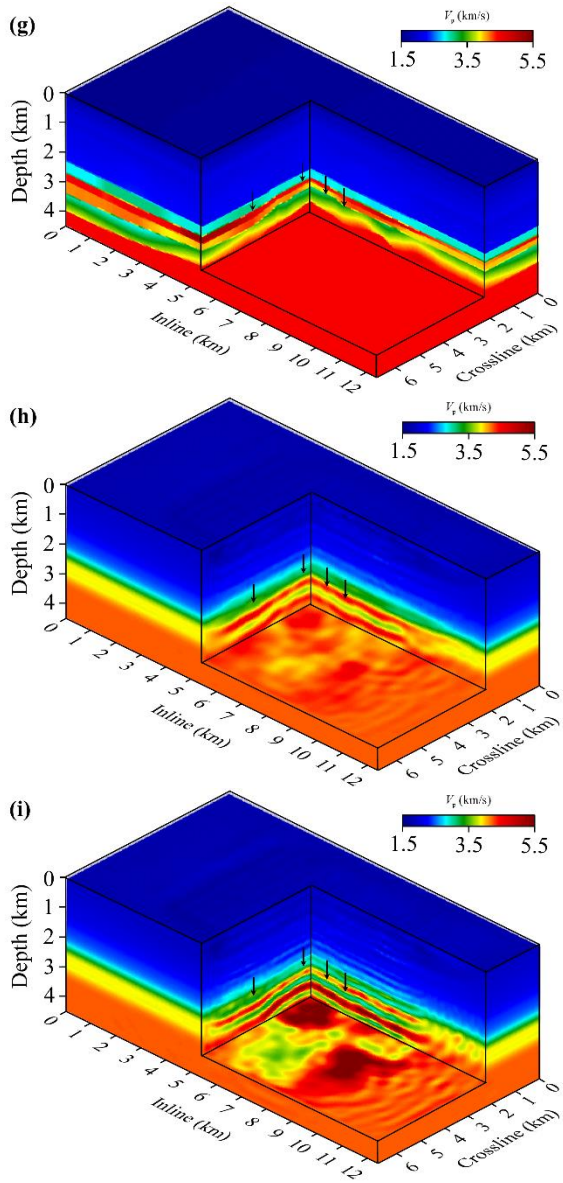

Fig. 5.9. (Continued)

In Fig. 5.12, receiver gathers of the observed and computed data for the initial background velocity model, inverted velocity models starting from the initial velocity model and background velocity model reconstructed by FWI with the nested algorithm are displayed. The phases of refractions and reflections are well-matched at the near-to-intermediate offsets. Note that some amplitude errors still exist over the whole offsets, because acoustic approximation cannot explain the PS mode conversion at the interface of seal rock. From these results, I confirm that the reconstructed P-wave velocity model reasonably describes the traveltime information of the observed pressure data acquired in the Volve oil field at the near-to-intermediate offsets.

Still, there are the incomplete reconstruction of the seal rock and reservoir at depths of 2.5 – 3 km and the amplitude errors in Fig. 5.12. One of the reasons is that the acoustic approximation cannot fully recover large contrasts of the P- and S-wave impedances (e.g., at the chalk interface) due to amplitude mismatches caused by the PS mode conversion (Plessix and Pérez Solano 2015; Agudo et al. 2020). Meanwhile, the traveltime differences caused by the anisotropic effects in the Volve oil field become remarkable at offsets longer than 4 – 5 km (Oh et al. 2018). To minimize the anisotropic effects, the vertical P-wave velocity is recovered using the reflections at the near-to-intermediate offsets in this thesis. However, the exclusion of the far-offset data leads to the absence of the low-vertical-wavenumber updates along the horizontal wavepaths of the diving waves and post-critical reflections. For further improvements, elastic anisotropic FWI should be performed to simultaneously recover the P- and S-wave structures concerning the anisotropy parameters using full

offsets. The reconstructed P-wave background velocity model can then be used as an initial guess.

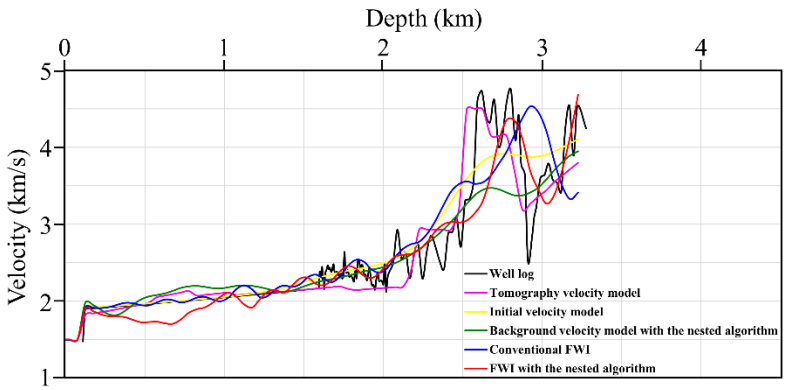

Fig. 5.10. Depth profiles of the well sonic log (the black line), reference tomography velocity model (the pink line), initial velocity model (the yellow line), background velocity model built by FWI with the nested algorithm (the green line), and finally inverted velocity models starting from the initial model (the blue line) and background velocity model reconstructed by FWI with the nested algorithm (the red line) along the well path shown in Fig. 5.3.

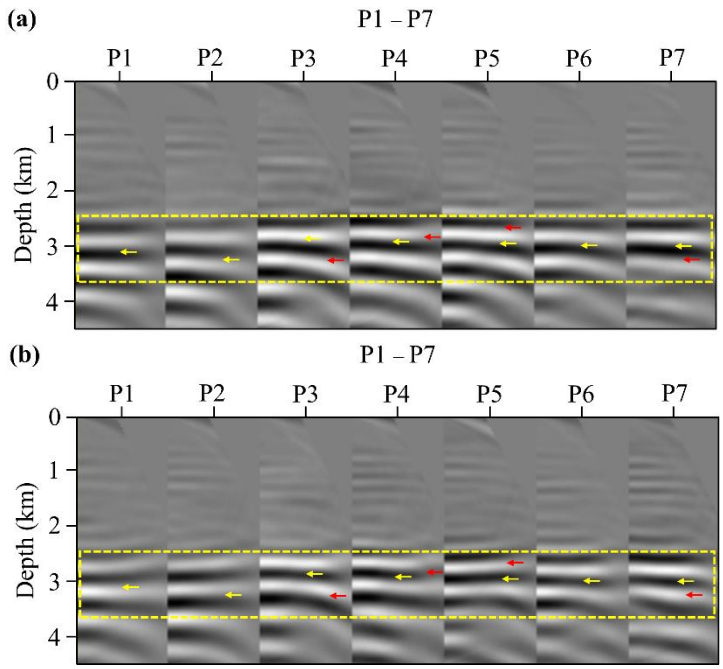

Fig. 5.11. ADCIGs computed in an inline profile of data extracted at a distance along the crossline direction of 3.65 km for the (a) initial velocity model and (b) background velocity model inverted by FWI with the nested algorithm. The angle ranges from 0° to 45°. P1 – P7 are located at (inline, crossline) = (4, 4.5) km, (4, 5) km, (4, 5.5) km, (4, 6) km, (4, 6.5) km, (4, 7) km and (4, 7.5) km.

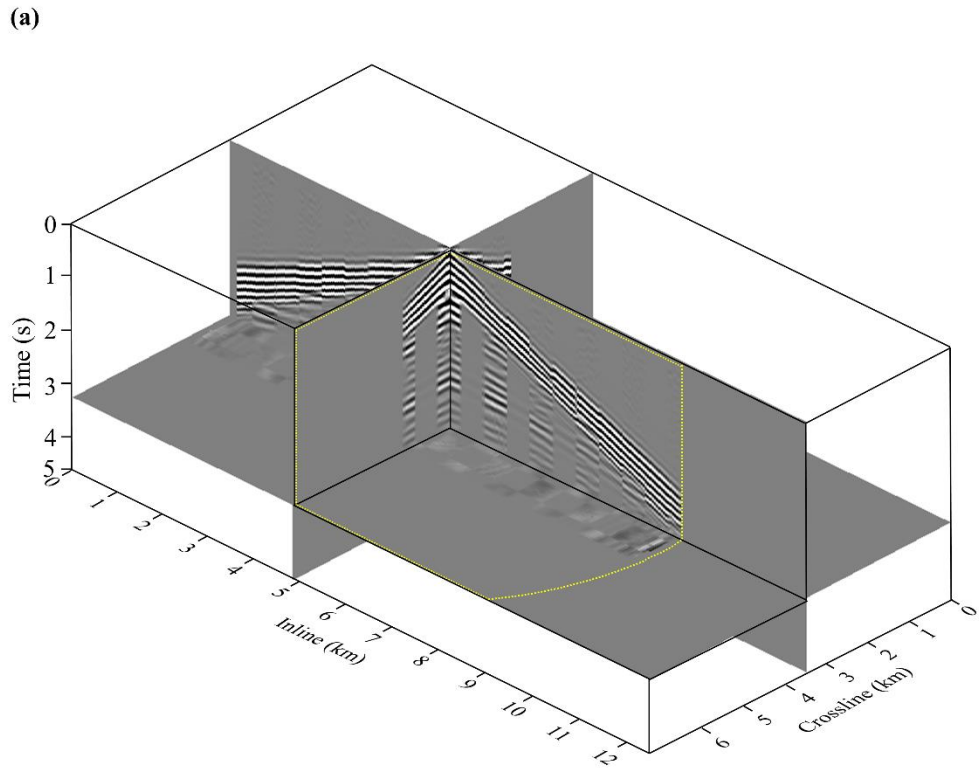

Fig. 5.12. Representative receiver gathers at distances of 4.8 and 3.25 km along the inline and crossline directions displayed by interweaving the observed data with the computed data for the (a) initial velocity model and inverted velocity models starting from the (b) initial velocity model and (c) background velocity model reconstructed by FWI with the nested algorithm every 10 x 10 traces. At the origin, the observed data are first shown followed by the computed data.

(b)

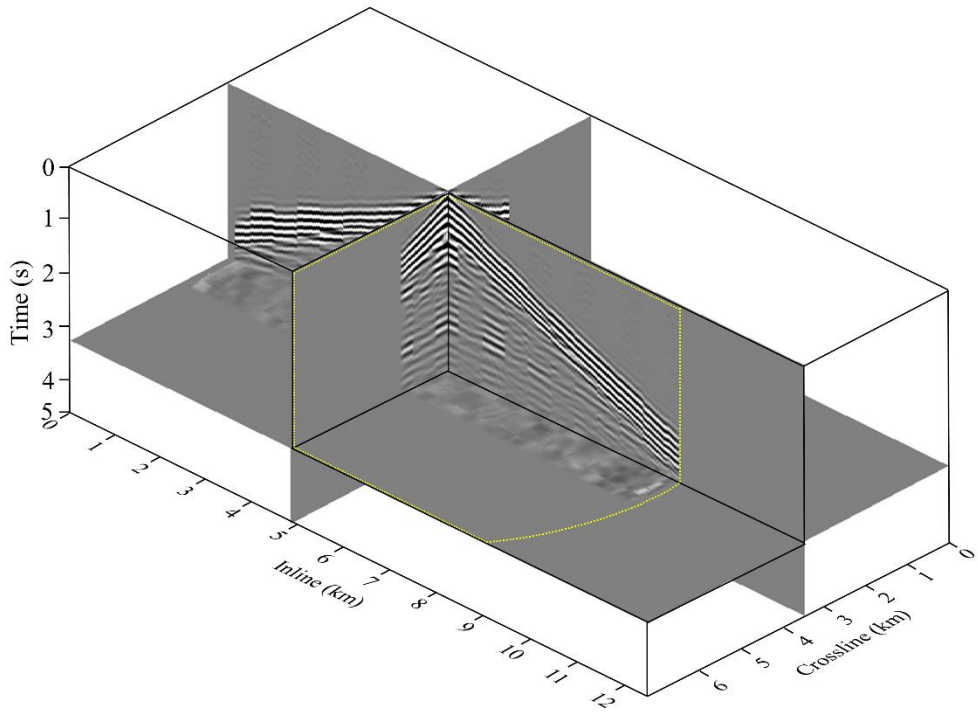

(c)

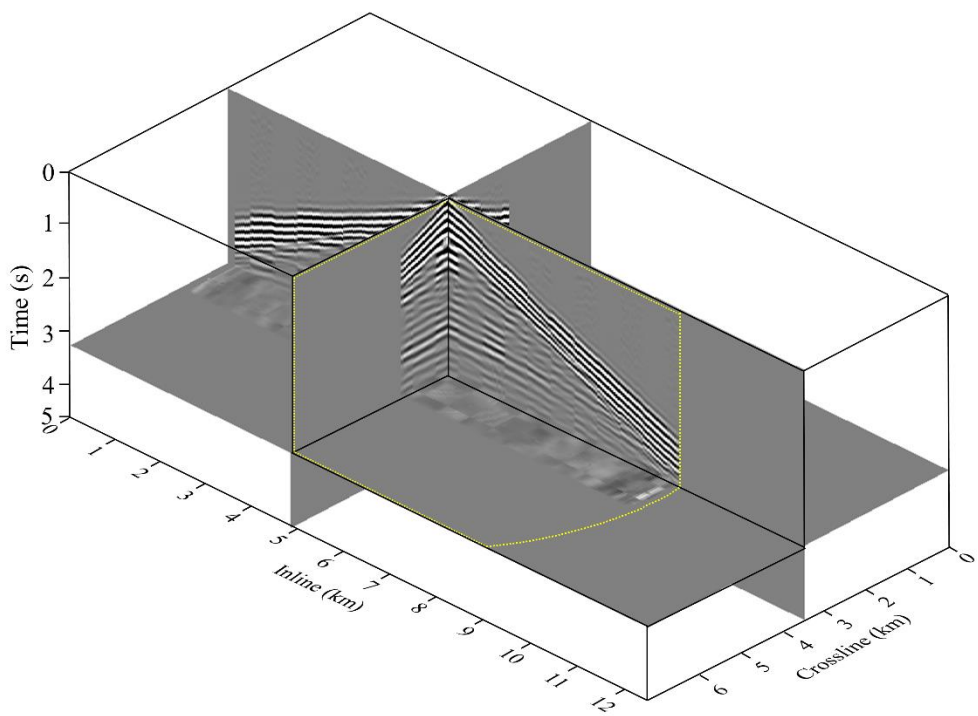

Fig. 5.12. (Continued)

Chapter 6. Conclusions

Acoustic FWI used to build the high-resolution subsurface velocity model from 3D pressure data suffers from the local minima problem without kinematically accurate macro velocity subsurface model. The reconstruction of the macro velocity structures mainly relies on the updates associated with diving waves in conventional FWI. In this study, to obtain the updates for macro velocity structures along the wavepaths of the diving and reflected waves in acoustic FWI, the diffraction-angle-filtering-based nested algorithm was designed and applied for 3D data sets. The diffraction-angle-filtering-based nested algorithm enables one to separate the velocity model into the high-wavenumber reflectivity model and low-wavenumber background velocity model. In the proposed algorithm, the high-wavenumber reflectivity model is first inverted to introduce the wavepaths of the reflected waves. Then, the low-wavenumber updates generated along the wavepaths of the diving and reflected waves provide complementary low-wavenumber coverage, which can reconstruct the background velocity model for subsequent FWI. In 3D acoustic FWI, diffraction-angle filtering can directly extract either the high- or low-wavenumber components of the gradient with reasonable computational efforts. Mode V of diffraction-angle filtering boosts the high-wavenumber migration isochrones related to the near-normal-incidence reflections to build prior reflectivity model, while mode IV of diffraction-angle filtering extracts the low-wavenumber first Fresnel zones along the wavepaths of the diving waves and the wavepaths of the reflected waves (which are generated by the prior reflectivity model) to reconstruct the background

velocity model.

The synthetic data example for the 3D SEG/EAGE overthrust model (which has strong lateral and vertical velocity variations) demonstrated that conventional FWI falls into local minima even when the seismic data is free from the elastic or anisotropic properties, whereas FWI with the proposed nested algorithm can build a reliable background velocity model, which enables FWI to converge toward the global minimum. With the complementary low-wavenumber updates along the reflection wavepaths, the distortion of the imaged fault block and folds caused by the thrust faults, which can lead to misunderstanding of the reservoir structures, is remarkably enhanced and reflectors are well focused. The application to the 3D field data set from the North Sea showed that acoustic FWI with the proposed algorithm can provide kinematically accurate P-wave background velocity model for seismic data with significant elastic and anisotropic effects. Even when the far-offset data are excluded during acoustic inversion because of the cross-talk effects between the P-wave velocity and anisotropy parameters, the nested algorithm enables FWI to recover the correct velocities of the overburden by the macro velocity updates along the reflection wavepaths generated from the seal rock. Although the amplitude errors cannot be fitted by acoustic FWI, the reconstructed background velocity model sufficiently describes the traveltimes of the observed PP refractions and reflections. The reconstructed P-wave background velocity model can be served as the initial guess for further multi-parameter inversion for elastic VTI media.

In general, acoustic FWI using the least-squares-norm-based local optimization is vulnerable to cycle-skipping and often requires proper time windows or offset

ranges to avoid cycle-skipping for a given frequency band. Moreover, acoustic FWI using the least-squares-norm-based local optimization is sensitive to amplitude errors, which can be significant at intermediate-to-far offsets because of the PS mode conversion in field data applications. The diffraction-angle-filtering-based nested algorithm can be easily implemented for other objective functions, which are more convex and robust to amplitude errors. Appropriate model constraints can also enhance the quality of the reconstructed background velocity model. By adopting more appropriate approaches for field data applications, the proposed algorithm can build the background velocity model in a more robust way. Besides, subsequent multi-parameter inversions for elastic anisotropic media should be considered when dealing with field data to quality control the reconstructed P-wave velocity model more precisely and obtain quantitatively reliable high-resolution subsurface velocity structures.

References

Agudo, Ò.C., da Silva, N.V., Stronge, G. & Warner, M., 2020. Mitigating elastic effects in marine 3-D full-waveform inversion, *Geophys. J. Int.*, **220**, 2089–2104.

Albertin, U., Shan, G. & Washbourne, J., 2013. Gradient orthogonalization in adjoint scattering-series inversion, in *SEG Technical Program Expanded Abstracts 2013*, pp. 1058–1062.

Alkhalifah, T., 2015a. Conditioning the full waveform inversion gradient to welcome anisotropy, *Geophysics*, **80**, R111–R122.

Alkhalifah, T., 2015b. Scattering-angle based filtering of the waveform inversion gradients, *Geophys. J. Int.*, **200**(1), 363–373.

Almomin, A. & Biondi, B., 2013. Tomographic full waveform inversion (TFWI) by successive linearizations and scale separations, in *SEG Technical Program Expanded Abstracts 2013*, pp. 1048–1052.

Aminzadeh, F., Brac, J. & Kunz, T., 1997. SEG/EAGE 3-D Salt and Overthrust models, *SEG/EAGE 3-D Modeling Series, No 1: Distribution CD of Salt and Overthrust models*, SEG book series.

Berenger, J.-P., 1994. A perfectly matched layer for the absorption of electromagnetic waves, *J. Comput. Phys.*, **114**(2), 185–200.

Biondi, B. & Almomin, A., 2014. Simultaneous inversion of full data bandwidth by

tomographic full-waveform inversion, *Geophysics*, **79**(3), WA129–WA140.

Bohlen, T., 2002. Parallel 3-D viscoelastic finite difference seismic modelling, *Comput. Geosci.*, **28**(8), 887–899.

Brossier, R., Operto, S. & Virieux, J., 2015. Velocity model building from seismic reflection data by full waveform inversion, *Geophys. Prospect.*, **63**, 354–367.

Bunks, C., Saleck, F.M., Zaleski, S. & Chavent, G., 1995. Multiscale seismic waveform inversion, *Geophysics*, **60**(5), 1457–1473.

Chavent, G., Clément, F. & Gómez, S., 1994. Automatic determination of velocities via migration-based traveltime waveform inversion: a synthetic data example, in *SEG Technical Program Expanded Abstracts 1994*, pp. 1179–1182.

Chen, Y., Feng, Z., Fu, L., AlTheyab, A., Feng, S. & Schuster, G., 2020. Multiscale reflection phase inversion with migration deconvolution, *Geophysics*, **85**(1), R55–R73.

Choi, Y. & Alkhalifah, T., 2012. Application of multi-source waveform inversion to marine streamer data using the global correlation norm, *Geophys. Prospect.*, **60**(4), 748–758.

Clément, F., Chavent, G. & Gómez, S., 2001. Migration-based traveltime waveform inversion of 2-D simple structures: a synthetic example, *Geophysics*, **66**,

845–860.

Collino, F. & Tsogka, C., 2001. Application of the perfectly matched absorbing layer model to the linear elastodynamic problem in anisotropic heterogeneous media, *Geophysics*, **66**, 294–307.

Crase, E., Pica, A., Noble, M., McDonald, J. & Tarantola, A., 1990. Robust elastic non-linear waveform inversion: application to real data, *Geophysics*, **55**, 527–538.

Dussaud, E., Symes, W.W., Williamson, P., Lemaistre, L., Singer, P., Denel, B. & Cherrett, A., 2008. Computational strategies for reverse-time migration, in *SEG Technical Program Expanded Abstracts 2008*, pp. 2267–2271.

Feng, S. & Schuster, G.T., 2019. Transmission + reflection anisotropic wave-equation traveltime and waveform inversion, *Geophys. Prospect.*, **67**, 423–442.

Fornberg, B., 1988. Generation of finite-difference formulas on arbitrary spaced grids, *Math. Comput.*, **51**, 699–706.

Fu, L., Feng, Z. & Schuster, G.T., 2019. Multiscale phase inversion for 3D ocean-bottom cable data, *Geophys. Prospect.*, **68**, 786–801.

Gholami, Y., Brossier, R., Operto, S., Ribodetti, A. & Virieux, J., 2013. Which parameterization is suitable for acoustic vertical transverse isotropic media full waveform inversion? Part 1: Sensitivity and trade-off analysis, *Geophysics*, **78**, R81–R105.

Grave, R., 1996. Simulating seismic wave propagation in 3D elastic media using staggered-grid finite differences, *Bull. Seismol. Soc. Am.*, **86**, 1091–1106.

Guo, Q. & Alkhalifah, T., 2017. Elastic reflection-based waveform inversion with a nonlinear approach, *Geophysics*, **82**(6), R309–R321.

Guitton, A., Ayeni, G. & Díaz, E., 2012. Constrained full-waveform inversion by model reparameterization, *Geophysics*, **77**(2), R117–R127.

Huang, Y. & Schuster, G., 2018. Full-waveform inversion with multisource frequency selection of marine streamer data, *Geophys. Prospect.*, **66**, 1243–1257.

Jeong, G., Hwang, J. & Min, D.-J., 2017. Comparison of weighting techniques for acoustic full waveform inversion, *J. Appl. Geophy.*, **147**, 16–27.

Kim, D., Hwang, J., Min, D.-J., Oh, J.-W. & Alkhalifah, T., 2022. Two-step full waveform inversion of diving and reflected waves with the diffraction-angle-filtering-based scale-separation technique, *Geophys. J. Int.*, **229**(2), 880–897.

Komatitsch, D. & Martin, R., 2007. An unsplit convolutional Perfectly Matched Layer improved at grazing incidence for the seismic wave equation, *Geophysics*, **72**(5), SM155–SM167.

Komatitsch, D. & Tromp, J., 1999. Introduction to the spectral element method for three-dimensional seismic wave propagation, *Geophys. J. Int.*, **139**(3), 806–822.

Lailly, P., 1983. The seismic inverse problem as a sequence of before stack migrations, in *Conference on Inverse Scattering: Theory and Application*, SIAM, 206–220.

Levander, A.R., 1988. Fourth-order finite-difference P-SV seismograms, *Geophysics*, **53**, 1425–1436.

Li, Y., Guo, Q., Li, Z. & Alkhalifah, T., 2019. Elastic reflection waveform inversion with variable density, *Geophysics*, **84**(4), R553–R567.

Li, Y. & Alkhalifah, T., 2020. Multi-parameter reflection waveform inversion for acoustic transversely isotropic media with a vertical symmetry axis, *Geophys. Prospect.*, **68**, 1878–1892.

Marfurt, K.J., 1984. Accuracy of finite-difference and finite-element modeling of the scalar and elastic wave equations, *Geophysics*, **49**(5), 533–549.

Martin, G.S., Wiley, R. & Marfurt, K.J., 2006. Marmousi2: An elastic upgrade for Marmousi, *Leading Edge*, **25**, 156–166.

Miller, D., Oristaglio, M. & Beylkin, G., 1987. A new slant on seismic imaging: migration and integral geometry, *Geophysics*, **52**(7), 943–964.

Mittet, R., 2002. Free-surface boundary conditions for elastic staggered-grid modeling schemes, *Geophysics*, **67**(5), 1616–1623.

Moczo, P., Kristek, J. & Halada, L., 2000. 3D fourth-order staggered-grid finite-difference schemes: stability and grid dispersion, *Bull. Seismol. Soc. Am.*, **90**, 587–603.

Mora, P.R., 1989. Inversion = migration + tomography, *Geophysics*, **54**(12), 1575–1586.

Oh, J.-W. & Alkhalifah, T., 2016. The scattering potential of partial derivative wavefields in 3D elastic orthorhombic media: An inversion prospective, *Geophys. J. Int.*, **206**, 1740–1760.

Oh, J.-W. & Min, D.-J., 2017. Multi-parameter full waveform inversion using Poisson's ratio for elastic media, *Explor. Geophys.*, **48**(4), 456–475.

Oh, J.-W., Kalita, M. & Alkhalifah, T., 2018. 3D elastic full-waveform inversion using P-wave excitation amplitude: Application to ocean bottom cable field data, *Geophysics*, **83**(2), R129–R140.

Oh, J.-W. & Alkhalifah, T., 2019. Study on the full-waveform inversion strategy for 3D elastic orthorhombic anisotropic media: application to ocean bottom cable data, *Geophys. Prospect.*, **67**, 1219–1242.

Oh, J.-W., Cheng, J. & Min, D.-J., 2021. Diffraction-angle filtering of gradient for acoustic full-waveform inversion, *Geophysics*, **86**(2), R173–R185.

Plessix, R.-E., 2006. A review of the adjoint-state method for computing the gradient of a functional with geophysical applications, *Geophys. J. Int.*, **167**(2), 495–503.

Plessix, R.-E., Baeten, G., de Maag, J.W., Klaassen, M., Zhang, R. & Tao, Z., 2010. Application of acoustic full waveform inversion to a low-frequency large-offset land data set, in *SEG Technical Program Expanded Abstracts 2010*,

pp. 930–934.

Plessix, R.-E. & Solano, C.P., 2015. Modified surface boundary conditions for elastic waveform inversion of low-frequency wide-angle active land seismic data, *Geophys. J. Int.*, **201**, 1324–1334.

Pratt, R.G., 1999. Seismic waveform inversion in the frequency domain, Part 1: Theory and verification in a physical scale model, *Geophysics*, **64**(3), 888–901.

Pratt, R.G., Song, Z.-M., Williamson, P. & Warner, M., 1996. Two-dimensional velocity models from wide-angle seismic data by wavefield inversion, *Geophys. J. Int.*, **124**, 323–340.

Pratt, R.G., Shin, C. & Hick, G., 1998. Gauss-Newton and full newton methods in frequency–space seismic waveform inversion, *Geophys. J. Int.*, **133**(2), 341–362.

Ramos-Martinez, J., Crawly, S., Zou, Z., Valenciano, A.A., Qiu, L. & Chemingui, N., 2016. A robust gradient for long wavelength FWI updates, in *78th Conference and Exhibition*, EAGE, Extended Abstracts.

Rocha, D., Tanushev, N. & Sava, P., 2016. Acoustic wavefield imaging using the energy norm, *Geophysics*, **81**(4), S151–S163.

Sava, P.C. & Fomel, S., 2003. Angle-domain common-image gathers by wavefield continuation methods, *Geophysics*, **68**(3), 1065–1074.

Sava, P.C. & Biondi, B., 2004. Wave-equation migration velocity analysis – 1:

Theory, *Geophys. Prospect.*, **52**(6), 593–606.

Sava, P.C. & Vasconcelos, I., 2011. Extended imaging conditions for wave-equation migration, *Geophys. Prospect.*, **59**(1), 35–55.

Shen, P. & Symes, W.W., 2008. Automatic velocity analysis via shot profile migration, *Geophysics*, **73**(5), VE49–VE59.

Shen, X., 2010. Near-surface velocity estimation by weighted early-arrival waveform inversion, *SEG Technical Program Expanded Abstracts 2010,* pp. 1975–1979.

Shin, C., Jang, S. & Min, D.-J., 2001. Improved amplitude preservation for prestack depth migration by inverse scattering theory, *Geophys. Prospect.*, **49**(5), 592–606.

Singh, S., Tsvankin, I. & Naeini, E.Z., 2021. Facies-based full-waveform inversion for anisotropic media: a North Sea case study, *Geophys. Prospect.*, **69**, 1650–1663.

Sirgue, L. & Pratt, R.G., 2004. Efficient waveform inversion and imaging: A strategy for selecting temporal frequencies, *Geophysics*, **69**(1), 231–248.

Symes, W.W., 2008. Migration velocity analysis and waveform inversion, *Geophys. Prospect.*, **56**, 765–790.

Symes, W.W. & Carazzone, J., 1991. Velocity inversion by differential semblance optimization, *Geophysics*, **56**, 654–663.

Szydlik, T., Smith, P., Way, S., Aamodt, L. & Friedrich, C., 2007. 3D PP/PS prestack

depth migration on the Volve field, *First Break*, **25**, 43–47.

Tang, Y., Lee, S., Baumstein, A. & Hinkley, D., 2013. Tomographically enhanced full wavefield inversion, in *SEG Technical Program Expanded Abstracts 2013*, pp. 1037–1041.

Tarantola, A., 1984. Inversion of seismic reflection data in the acoustic approximation, *Geophysics*, **49**(8), 1259–1266.

Tarantola, A., 1986. A strategy for nonlinear elastic inversion of seismic reflection data, *Geophysics*, **51**, 1893–1903.

Thiel, N., Hertweck, T. & Bohlen, T., 2019. Comparison of acoustic and elastic full-waveform inversion of 2D towed-streamer data in the presence of salt, *Geophys. Prospect.*, **67**(2), 349–361.

Trinh, P.T., Brossier, R., Métivier, L., Tavard, L. & Virieux, J., 2019. Efficient time-domain 3D elastic and viscoelastic full-waveform inversion using a spectral-element method on flexible Cartesian-based mesh, *Geophysics*, **84**(1), R61–R83.

Virieux, J., 1984. SH-wave propagation in heterogeneous media: Velocity-stress finite-difference method, *Geophysics*, **49**(11), 1933–1942.

Virieux, J. & Operto, S., 2009. An overview of full-waveform inversion in exploration geophysics, *Geophysics*, **74**(6), WCC1–WCC26.

Wang, F., Chauris, H., Donno, D. & Calandra, H., 2013. Taking advantage of wave field decomposition in full waveform inversion, in *EAGE Technical*

Program Expanded Abstracts 2013, p. Tu0708.

Wang, F., Donno, D., Chauris, H., Calandra, H. & Audebert, F., 2016. Waveform inversion based on wavefield decomposition, *Geophysics*, **81**(6), R457–R470.

Warner, M., Ratcliffe, A., Nangoo, T., Morgan, J., Umpleby, A., Shah, N., Vinje, V., Štekl, I., Guasch, L., Win, C., Conroy, G. & Bertrand, A., 2013. Anisotropic 3D full-waveform inversion, *Geophysics*, **78**(2), R59–R80.

Wellington, P., Brossier, R., Garambois, S. & Virieux, J., 2015. 2D acoustic time domain full waveform inversion-a broadband application in the Carnarvon basin, Australia, in *EAGE Technical Program Expanded Abstracts 2015*, p. WeP116.

Wellington, P., Brossier, R. & Virieux, J., 2019. Preconditioning full-waveform inversion with efficient local correlation operators, *Geophysics*, **84**(3), R321–R332.

Whitmore, N.D. & Crawley, S., 2012. Applications of RTM inverse scattering imaging conditions, in *SEG Technical Program Expanded Abstracts 2012*, pp. 1–6.

Woodward, M.J., 1992. Wave-equation tomography, *Geophysics*, **57**, 15–26.

Wu, Z. & Alkhalifah, T., 2015. Simultaneous inversion of the background velocity and the perturbation in full-waveform inversion, *Geophysics*, **80**(6), R317–R329.

Wu, Z. & Alkhalifah, T., 2017. Efficient scattering-angle enrichment for a nonlinear inversion of the background and perturbations components of a velocity model, *Geophys. J. Int.*, **210**, 1981–1992.

Xu, S., Wang, D., Chen, F., Lambare, G. & Zhang, Y., 2012. Inversion on reflected seismic wave, in *82nd Ann. Internat. Mtg.*, pp. 1–7, Soc. Expl. Geophys.

Yao, G., da Silva, N.V., Warner, M. & Kalinicheva, T., 2018. Separation of migration and tomography modes of full-waveform inversion in the plane wave domain, *J. Geophys. Res. Solid Earth*, **123**, 1486–1501.

Yao, G., Wu, D. & Wang, S.-X., 2020. A review on reflection-waveform inversion, *Pet. Sci.*, **17**, 334–351.

Zhang, Z.-d. & Alkhalifah, T., 2017. Full waveform inversion using oriented time-domain imaging method for vertical transverse isotropic media, *Geophys. Prospect.*, **65**, 166–180.

Zhou, W., Brossier, R., Operto, S. & Virieux, J., 2015. Full waveform inversion of diving and reflected waves for velocity model building with impedance inversion based on scale separation, *Geophys. J. Int.*, **202**(3), 1535–1554.

Zhou, W., Brossier, R., Operto, S., Virieux, J. & Yang, P., 2018. Velocity model building by waveform inversion of early arrivals and reflections: A 2D case study with gas-cloud effects, *Geophysics*, **83**(2), R141–R157.

Appendix A. Derivation of the gradient using the adjoint-state method

In this appendix, the gradient of FWI is derived using the adjoint-state method following Plessix (2006). The acoustic wave equation with the second-order derivatives of wavefields in the temporal and spatial coordinates in terms of pressure and its initial and radiation boundary conditions are written as:

$$\frac{1}{V_{\mathrm{p}}(\mathbf{x})^2}\frac{\partial^2 P(\mathbf{x}_s, \mathbf{x}, t)}{\partial t^2} = \nabla^2 P(\mathbf{x}_s, \mathbf{x}, t) + f_P(\mathbf{x}_s, t)$$

$$\begin{cases} P(\mathbf{x}_s, \mathbf{x}, 0) = 0 \\ \left.\dfrac{\partial P(\mathbf{x}_s, \mathbf{x}, t)}{\partial t}\right|_{t=0} = 0 \\ \lim\limits_{\mathbf{x}\to\infty} P(\mathbf{x}_s, \mathbf{x}, t) = 0 \end{cases} . \qquad \text{(A-1)}$$

Then, the objective function for one source-receiver pair with the governing equation (the acoustic wave equation) is written as follows:

$$E(V_{\mathrm{p}}(\mathbf{x})) = \frac{1}{2}\iint \left[P^c(\mathbf{x}_s, \mathbf{x}_r, t) - P^o(\mathbf{x}_s, \mathbf{x}_r, t)\right]^2 d\mathbf{x}dt - \iint q(\mathbf{x}_s, \mathbf{x}, t)\left(\frac{1}{V_{\mathrm{p}}(\mathbf{x})^2}\frac{\partial^2 P^c(\mathbf{x}_s, \mathbf{x}, t)}{\partial t^2} - \nabla^2 P^c(\mathbf{x}_s, \mathbf{x}, t) - f_P(\mathbf{x}_s, t)\right) d\mathbf{x}dt \,, \qquad \text{(A-2)}$$

where

$$\begin{aligned}&\frac{1}{2}\iint\left[P^c(\mathbf{x}_s,\mathbf{x}_r,t)-P^o(\mathbf{x}_s,\mathbf{x}_r,t)\right]^2 d\mathbf{x}dt\\&=\frac{1}{2}\iint\left[P^c(\mathbf{x}_s,\mathbf{x},t)-P^o(\mathbf{x}_s,\mathbf{x},t)\right]^2\delta(\mathbf{x}-\mathbf{x}_r)d\mathbf{x}dt\end{aligned}. \tag{A-3}$$

Because the second term in equation (A-2) is always zero for any wavefield q, the objective function is exactly the same as that in equation (2-10). According to the integration by parts and Gauss divergence theorem, each part of the second term is rearranged as follows:

$$\begin{aligned}&\iint q(\mathbf{x}_s,\mathbf{x},t)\left(\frac{1}{V_p(\mathbf{x})^2}\frac{\partial^2 P^c(\mathbf{x}_s,\mathbf{x},t)}{\partial t^2}\right)d\mathbf{x}dt\\&=\int\left\{q(\mathbf{x}_s,\mathbf{x},t)\frac{1}{V_p(\mathbf{x})^2}\frac{\partial P^c(\mathbf{x}_s,\mathbf{x},t)}{\partial t}\bigg|_0^T-\int\frac{\partial q(\mathbf{x}_s,\mathbf{x},t)}{\partial t}\frac{1}{V_p(\mathbf{x})^2}\frac{\partial P^c(\mathbf{x}_s,\mathbf{x},t)}{\partial t}dt\right\}d\mathbf{x}\\&=\int-\left\{\frac{\partial q(\mathbf{x}_s,\mathbf{x},t)}{\partial t}\frac{1}{V_p(\mathbf{x})^2}\frac{\partial P^c(\mathbf{x}_s,\mathbf{x},t)}{\partial t}\bigg|_0^T+\int\frac{\partial^2 q(\mathbf{x}_s,\mathbf{x},t)}{\partial t^2}\frac{1}{V_p(\mathbf{x})^2}P^c(\mathbf{x}_s,\mathbf{x},t)dt\right\}d\mathbf{x}\\&=\iint\frac{\partial^2 q(\mathbf{x}_s,\mathbf{x},t)}{\partial t^2}\frac{1}{V_p(\mathbf{x})^2}P^c(\mathbf{x}_s,\mathbf{x},t)d\mathbf{x}dt\end{aligned}, \tag{A-4}$$

and

$$\begin{aligned}&\iint q(\mathbf{x}_s,\mathbf{x},t)\left(\nabla^2 P^c(\mathbf{x}_s,\mathbf{x},t)\right)d\mathbf{x}dt\\&=\iint\nabla\cdot\left(q(\mathbf{x}_s,\mathbf{x},t)\nabla P^c(\mathbf{x}_s,\mathbf{x},t)\right)-\nabla q(\mathbf{x}_s,\mathbf{x},t)\cdot\nabla P^c(\mathbf{x}_s,\mathbf{x},t)d\mathbf{x}dt,\\&=\iint-\nabla q(\mathbf{x}_s,\mathbf{x},t)\cdot\nabla P^c(\mathbf{x}_s,\mathbf{x},t)d\mathbf{x}dt\end{aligned} \tag{A-5}$$

which are satisfied under the termination and radiation boundary condition for q as follows:

$$\begin{cases} q(\mathbf{x}_s, \mathbf{x}, T) = 0 \\ \left.\dfrac{\partial q(\mathbf{x}_s, \mathbf{x}, t)}{\partial t}\right|_{t=T} = 0 \end{cases}, \tag{A-6}$$

and

$$\lim_{\mathbf{x}\to\infty} q(\mathbf{x}_s, \mathbf{x}, t) = 0\,, \tag{A-7}$$

where T is the total recording length. Therefore, equation (A-2) is rewritten as:

$$\begin{aligned} E(V_{\mathrm{p}}(\mathbf{x})) = & \frac{1}{2}\iint \left[P^c(\mathbf{x}_s, \mathbf{x}_r, t) - P^o(\mathbf{x}_s, \mathbf{x}_r, t)\right]^2 d\mathbf{x}dt \\ & - \iint \frac{\partial^2 q(\mathbf{x}_s, \mathbf{x}, t)}{\partial t^2} \frac{1}{V_{\mathrm{p}}(\mathbf{x})^2} P^c(\mathbf{x}_s, \mathbf{x}, t) d\mathbf{x}dt \\ & - \iint \nabla q(\mathbf{x}_s, \mathbf{x}, t) \cdot \nabla P^c(\mathbf{x}_s, \mathbf{x}, t) d\mathbf{x}dt + \iint f_P(\mathbf{x}_s, t) q(\mathbf{x}_s, \mathbf{x}, t) d\mathbf{x}dt \end{aligned} . \tag{A-8}$$

Then, the total derivative of Equation (A-8) is

$$\begin{aligned} \partial E(V_{\mathrm{p}}(\mathbf{x})) = & \iint \partial P^c(\mathbf{x}_s, \mathbf{x}, t)\left[P^c(\mathbf{x}_s, \mathbf{x}_r, t) - P^o(\mathbf{x}_s, \mathbf{x}_r, t)\right] d\mathbf{x}dt \\ & - \iint \partial P^c(\mathbf{x}_s, \mathbf{x}, t) \frac{1}{V_{\mathrm{p}}(\mathbf{x})^2} \frac{\partial^2 q(\mathbf{x}_s, \mathbf{x}, t)}{\partial t^2} d\mathbf{x}dt \\ & + \iint \partial P^c(\mathbf{x}_s, \mathbf{x}, t) \nabla^2 q(\mathbf{x}_s, \mathbf{x}, t)\, d\mathbf{x}dt \\ & - \iint \partial V_{\mathrm{p}}(\mathbf{x}) \left(P^c(\mathbf{x}_s, \mathbf{x}, t) \frac{2}{V_{\mathrm{p}}(\mathbf{x})^3} \frac{\partial^2 q(\mathbf{x}_s, \mathbf{x}, t)}{\partial t^2} \right) d\mathbf{x}dt \end{aligned} . \tag{A-9}$$

The adjoint wavefield is defined as:

$$P_s^b(\mathbf{x}_s, \mathbf{x}, t) = q(\mathbf{x}_s, \mathbf{x}, T - t)\,. \tag{A-10}$$

In summary, for the adjoint wavefield that satisfies the following conditions:

$$\begin{aligned}&\frac{1}{V_{\mathrm{p}}(\mathbf{x})^2}\frac{\partial^2 P_s^b(\mathbf{x}_s,\mathbf{x},t)}{\partial t^2}-\nabla^2 P_s^b(\mathbf{x}_s,\mathbf{x},t)\\&=\left[P^c(\mathbf{x}_s,\mathbf{x}_r,T-t)-P^o(\mathbf{x}_s,\mathbf{x}_r,T-t)\right]\end{aligned}$$

$$\begin{cases}P_s^b(\mathbf{x}_s,\mathbf{x},0)=0\\ \left.\dfrac{\partial P_s^b(\mathbf{x}_s,\mathbf{x},t)}{\partial t}\right|_{t=0}=0\\ \lim\limits_{\mathbf{x}\to\infty}P_s^b(\mathbf{x}_s,\mathbf{x},t)=0\end{cases}, \qquad \text{(A-11)}$$

the gradient can be computed as:

$$\frac{\partial E(V_{\mathrm{p}}(\mathbf{x}))}{\partial V_{\mathrm{p}}(\mathbf{x})}=-\iint\left(P^c(\mathbf{x}_s,\mathbf{x},t)\frac{2}{V_{\mathrm{p}}(\mathbf{x})^3}\frac{\partial^2 P_s^b(\mathbf{x}_s,\mathbf{x},T-t)}{\partial t^2}\right)d\mathbf{x}dt\,, \qquad \text{(A-12)}$$

which is identical to the equation (2-12).

Appendix B. Application to synthetic data: 2D Marmousi-II model

B.1. Modeling and inversion parameters

In this appendix, the application of the nested algorithm to the synthetic 2D pressure data computed for the Marmousi-II model (Fig. B.1; Martin et al. 2006) is introduced. Appendix B is extracted from the works in Kim et al. (2022). The model is discretized by 460 x 153 grid points with a grid interval of 20 m. It is assumed that 46 shots and 460 receivers are applied with an even interval at a depth of 20 m, and that the shot and receiver intervals are 200 and 20 m, respectively. A linearly-increasing 1-D velocity model is used for an initial model as shown in Fig. B.2(a). For the source function, a Ricker wavelet with a peak frequency of 6.5 Hz is used. The total recording length is 5.2 s. The zero-phase Butterworth filters with bandwidths of $3-6$, $3-9$ and $3-12$ Hz is applied to the observed and modeled data for the multiscale strategy (Bunks et al. 1995). For numerical modeling, I use the 4th-order staggered-grid finite-difference method (Virieux 1984) and convolutional perfectly matched layers (Komatitsch and Martin 2007) are added to avoid artificial boundary reflections. Fig. B.3 shows a representative shot gather at a distance of 1.9 km. We can observe the pre-critical reflected waves at near-to-intermediate offsets (in the red box) and the diving and post-critical reflected waves at far offsets (outside the red box). Following the workflow described in Algorithm 3.1, I invert the reflectivity model δV_{p} using near-offset data in the first inner loop starting from the given background velocity model V_{p0}. Then, in the second inner

loop, the low-wavenumber updates are computed in the velocity model $\delta V_{\mathrm{p}} + V_{\mathrm{p0}}$ using the full-offset data. The preconditioned steepest-descent method is applied for the two inner loops. The gradient is preconditioned by the pseudo-Hessian matrix (Shin et al. 2001). Considering that incompletely inverted reflectivity model boosts the high-wavenumber artifacts and hinders the contribution of the reflected waves to the update of the background velocity model, I iterate the first inner loop by 10 times for each background velocity model so that the amplitudes and phases of reflected waves can be well matched with those of the observed data at near offsets. The second inner loop is just performed by single time. I iterate the outer loop by 10 times for each frequency band. I use a fixed step-length of 0.05 km/s for the two inner loops.

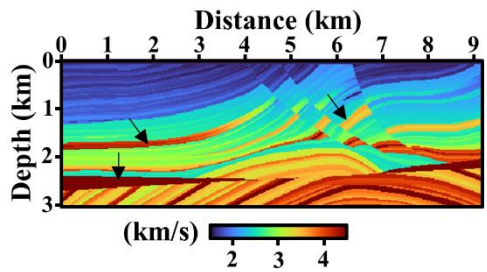

Fig. B.1. The true 2D Marmousi-II P-wave velocity model. The black arrows indicate the part that we should pay attention to when comparing inversion results.

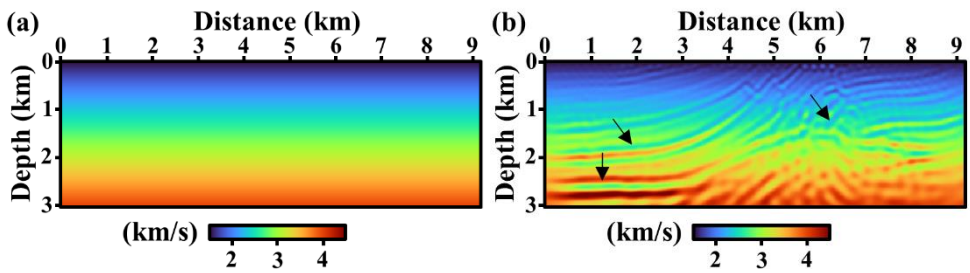

Fig. B.2. (a) The linearly-increasing background velocity model used as an initial guess and (b) the reflectivity model $\delta V_{\mathrm{p}} + V_{\mathrm{p0}}$ recovered by using near-normal-incidence reflections by mode V of diffraction-angle filtering starting from the initial background velocity model.

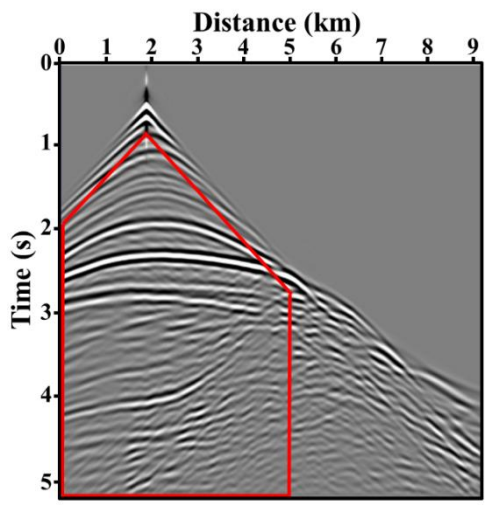

Fig. B.3. A representative shot gather at a distance of 1.9 km of the Marmousi-II model. The seismic data contain the pre-critical reflections (in the red box), diving waves and post-critical reflections (outside the red box).

B.2. Inversion results

Fig. B.2(b) shows the resultant model $\delta V_p + V_{p0}$ after 10 iterations of the first inner loop. We observe that some reflectors are mispositioned (pointed by the black arrows), which can be moved to the correct positions by using additional low-wavenumber information along the reflection wavepaths. Recall that mode V suppresses the low-wavenumber components of the gradient and boosts the contribution of the near-normal-incidence data. Fig. B.4 shows filtered versions of the gradients computed at the first iteration of the second inner loop for the reconstruction of the background velocity model. To examine if the pre-critical reflections can provide complementary low-wavenumber coverage for the background velocity model reconstruction, which cannot be covered by only the diving waves, I separate the pre-critical reflections and early-arrivals (the diving waves and post-critical reflections) by using a linear time-offset window (the red box in Fig. B.3). To demonstrate if energy at intermediate diffraction angles is suppressed by mode IV, the gradients filtered by mode IV are compared to those filtered by mode II (whose mechanism is identical to the ENIC proposed by Rocha et al. 2016). Because mode IV applied in the second inner loop additionally suppresses the energy at intermediate diffraction angles, the gradient filtered by mode IV in Fig. B.4(b) reveals macro-structures of the velocity model without high-wavenumber artifacts compared with that filtered by mode II in Fig. B.4(a). The gradients computed using only the early-arrival data are shown in Figs. B.4(c) and B.4(d).

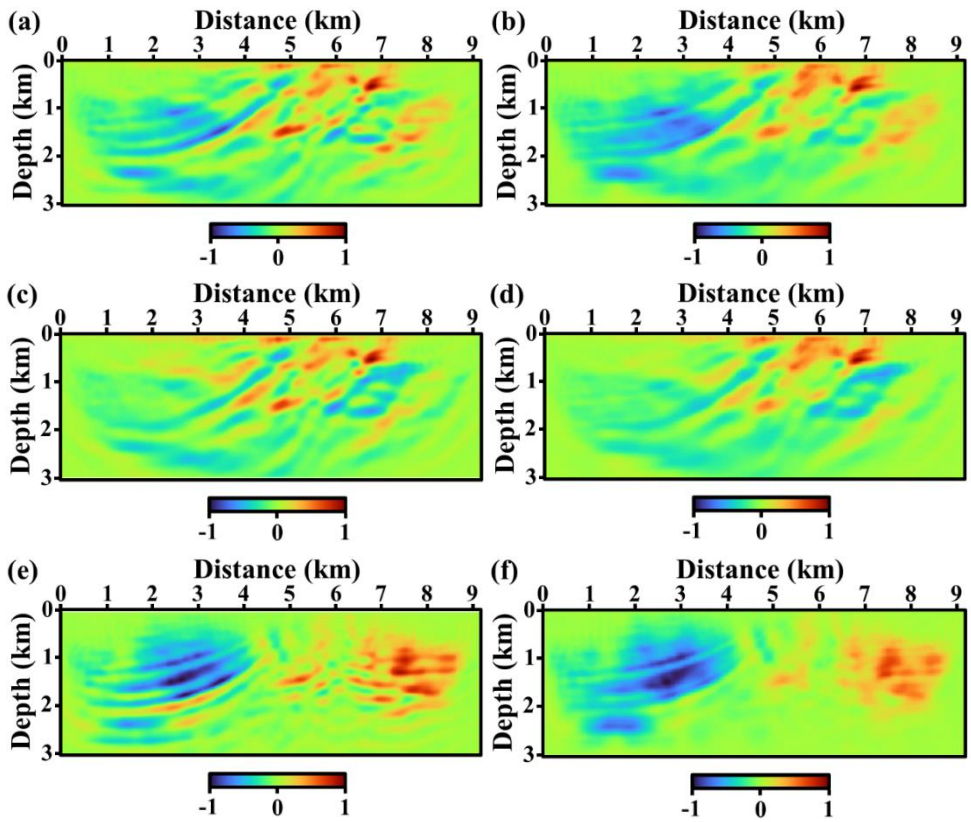

Fig. B.4. The gradients computed at the first iteration of the second inner loop of the nested algorithm using (a, b) the full data, (c, d) the early arrival data and (e, f) the pre-critical reflection data. The left panels (a, c, e) are filtered by mode II and the right panels (b, d, e) are filtered by mode IV.

In Figs. B.4(c) and B.4(d), the gradients mainly derived by the diving-wave-related first Fresnel zones reveal the low-wavenumber structures up to a depth of 2.5 km along the paths of the diving waves. However, due to the limitation of acquisition geometry, the left-hand and right-hand sides of the model are hardly delineated. Likewise, mode IV shows better performance compared with mode II. In contrast, the gradients computed using only the pre-critical reflection data provide the information of macro-structures at distances of 0 – 3 km and 7 – 9 km in Figs. B.4(e) and B.4(f). Because strong reflectors are located at depths of 2 – 2.5 km, the gradients in Figs. B.4(e) and B.4(f) mainly delineate the structures above a depth of 2 km. The migration isochrones at intermediate diffraction angles are dominant in this case and thus high-wavenumber artifacts severely occur in the gradient filtered by mode II compared with that filtered by mode IV, which shows the performance of mode IV in dealing with pre-critical reflection data. In Fig. B.5, I present the background velocity models corresponding to the gradients in Fig. B.4. Figs. B.5(a) and B.5(b) demonstrate that FWI with the nested algorithm using both the diving and reflected waves yields the best low-wavenumber coverage, which describes macro-structures of the Marmousi-II model, compared with Figs. B.5(c) – B.5(f). In Figs. B.5(c) and B.5(d), while the shallow parts of the background velocity are improved by the contribution of the diving waves, the left-hand side of the model (at distances of 0 – 3 km) and macro-structures at depths of 1 – 2 km are not recovered well even though the diving waves can reach the deepest part of the model. This is probably due to the limited wavenumber coverage of the diving-wave-related first Fresnel zones and cycle skipping of far-offset data containing the diving waves.

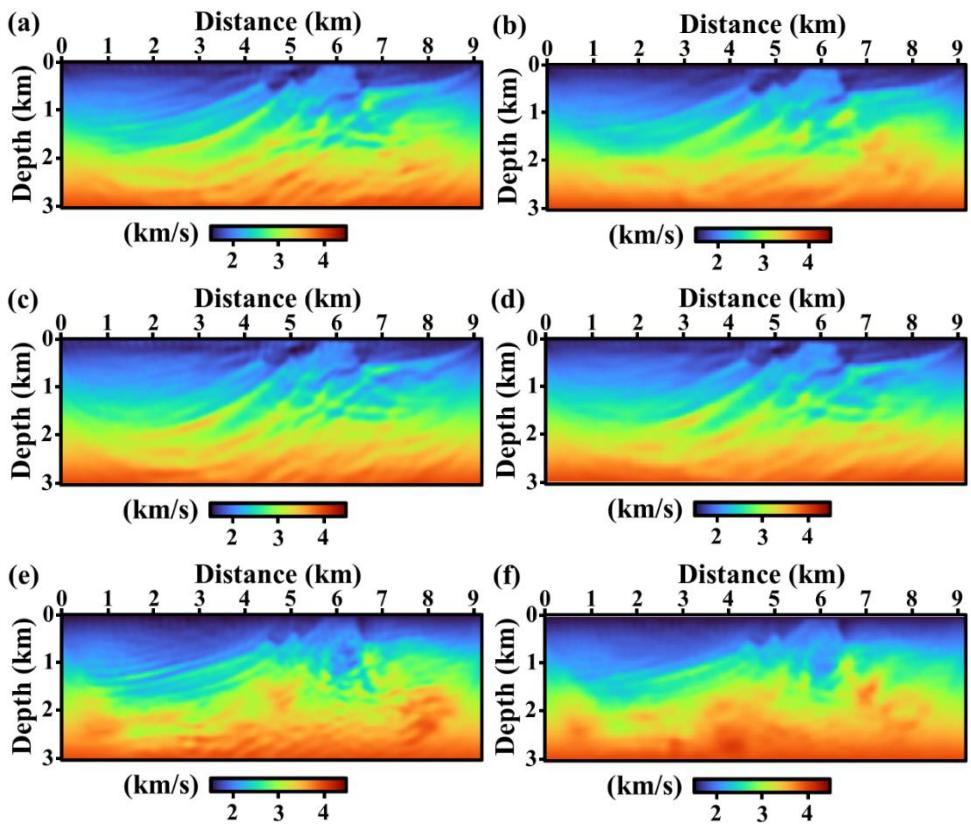

Fig. B.5. The background velocity models built by FWI with the nested algorithm using (a, b) the full data, (c, d) the early arrival data and (e, f) the pre-critical reflection data. The left panels (a, c, e) are filtered by mode II and the right panels (b, d, e) are filtered by mode IV in the second inner loop.

When an initial velocity model deviates from the true velocity model, far-offset data required to retrieve low-wavenumber information of the deep parts are prone to be cycle-skipped, which causes the local minima problem. On the other hand, Figs. B.5(e) and B.5(f) show that FWI with the nested algorithm using the pre-critical reflection data resolves macro-structures different from those delineated by FWI with the nested algorithm using the early-arrival data, specifically above a depth of 2 km, which leads to wider coverage of low-wavenumber structures in Figs B.5(a) and B.5(b). Note that the background velocity models obtained by FWI with the nested algorithm filtered by mode II (Figs. B.5a, B.5c and B.5e) contain some high-wavenumber artifacts and do not fully resolve macro-structures compared with those filtered by mode IV (Figs. B.5b, B.5d and B.5f).

To compare these results with those of Oh et al. (2021), I display the gradient at the first iteration and the final model obtained by applying mode IV in conventional FWI in Figs. B.6 and B.7. By comparing Fig. B.6 with Fig. B.4, we see that the gradient of Fig. B.6 looks similar to that of Fig. B.4(d), which indicates that mode IV plays a role in recovering low-wavenumber information carried by the diving waves in the conventional FWI framework. Accordingly, the resultant background velocity in Fig. B.7 cannot recover reliable macro-structures as in the inverted background velocity in Fig. B.5(d). From these results, we can confirm that FWI with the nested algorithm boosts up the contribution of the reflected waves to the low-wavenumber update, which provides complementary low-wavenumber information in addition to the low-wavenumber update from the diving waves and post-critical reflections.

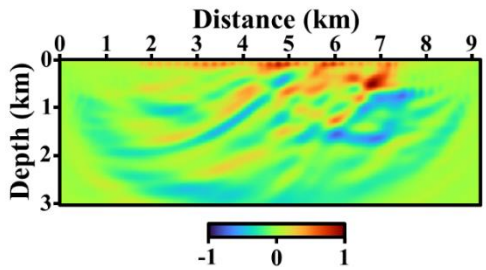

Fig. B.6. The gradient obtained by applying mode IV at the first iteration of conventional FWI.

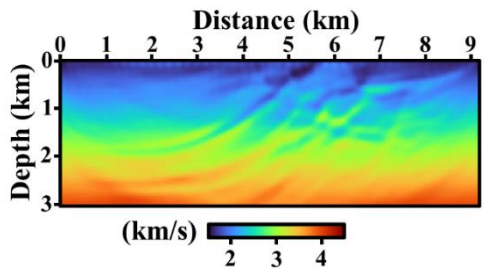

Fig. B.7. The background velocity model obtained by applying mode IV in conventional FWI.

The background velocity model can be used as an initial model in subsequent FWI performed to recover detailed velocity structures. Figs. B.8(a) and B.8(b) show the final velocity models inverted by subsequent FWI starting from the linearly-increasing velocity model (i.e., initial model) and the background velocity model recovered by FWI with the nested algorithm, respectively. When I start from the linearly-increasing model, I fail to recover the accurate velocity model because of the severe traveltime errors due to the inaccurate initial model (Fig. B.8a). In contrast, when I start from the background velocity model reconstructed by FWI with the nested algorithm, I obtain inversion result comparable to the true velocity model (Fig. B.8b).

In Fig. B.9, I show absolute differences between the inverted models and the true velocity model. For reference, I also display the difference between the linearly-increasing velocity model and true velocity model. We observe that the differences for the case of starting from the background velocity obtained by FWI with the nested algorithm (Fig. B.9b) are smaller than those for both the linearly-increasing velocity model (Fig. B.9c) and the final velocity model starting from the linearly-increasing velocity model (Fig. B.9a), specifically at depths of $0 - 2$ km. Fig. B.10(a) shows shot gathers of the observed and modeled data generated for the finally inverted model (e.g., Fig. B.8b), which indicate that the amplitudes and phases of refractions and reflections are also well-recovered. Fig. B.10(b) also supports that traces of the observed and modeled data match well with each other. These results convince us that the success of FWI depends on the recovery of reliable background velocity,

which can be accomplished by effectively extracting low-wavenumber information from both the diving and pre-/post-critical reflected waves.

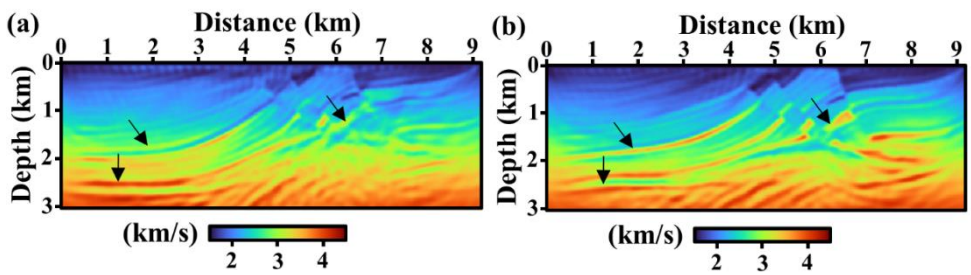

Fig. B.8. Final inversion results obtained by subsequent FWI starting from (a) the linearly-increasing velocity model and (b) the background velocity model obtained by FWI with the nested algorithm.

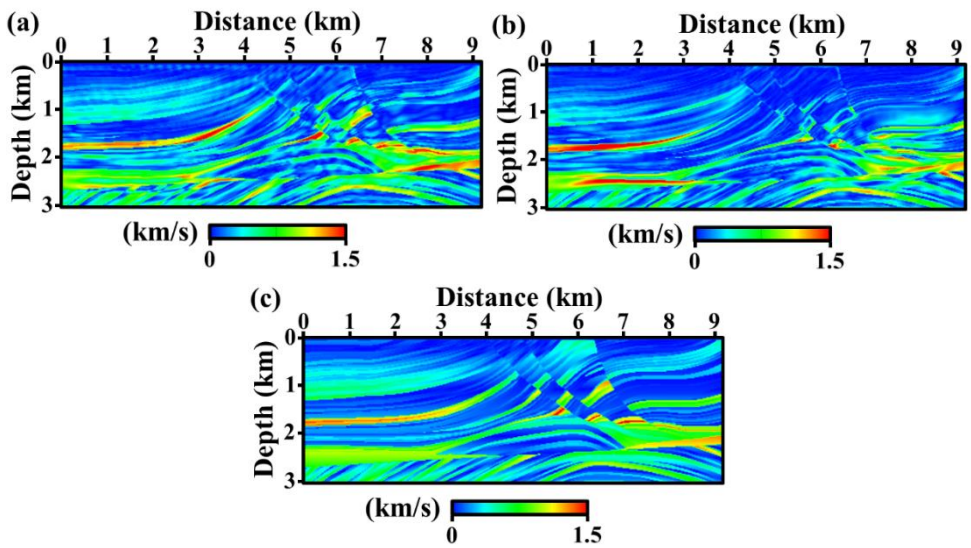

Fig. B.9. Absolute differences between the true Marmousi-II velocity model and the final velocity models inverted by subsequent FWI starting from (a) the linearly-increasing velocity model and (b) the background velocity model obtained by FWI with the nested algorithm. For reference, the differences between the true and linearly-increasing velocity models are also displayed in (c).

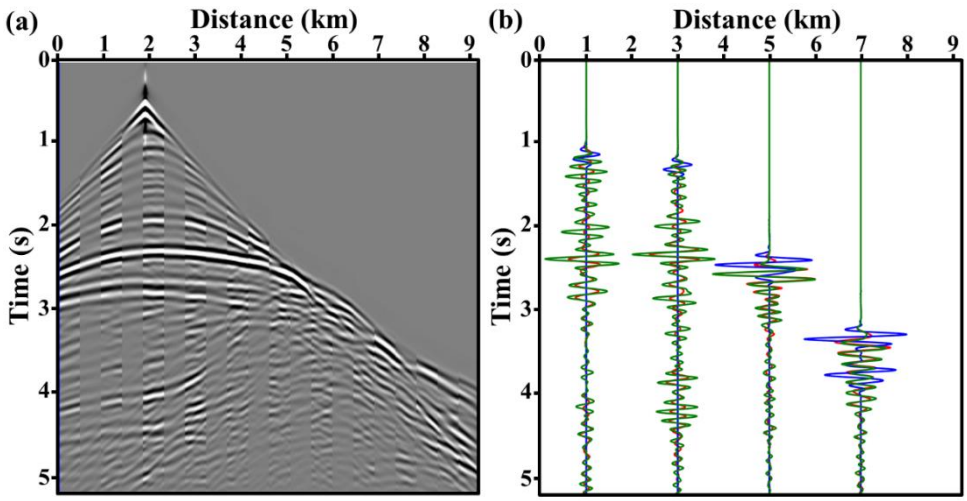

Fig. B.10. (a) A representative shot gather at a distance of 1.9 km displayed by interweaving the observed data with the modeled data for the final inversion result (shown in Fig. B.8b) every 23 traces. From left to right in the panel, the observed data are shown first followed by the modeled data. (b) The comparison of the traces of the observed (green) and modeled data for the linearly-increasing (blue) and final velocity models (red).

Appendix C. Application to field data: North Sea Volve oil field 2D OBC data

C.1. Inversion parameters and strategies

In this appendix, the application of the nested algorithm to the 2D line of the OBC data set acquired in the Volve oil field of the North Sea in 2002 (Szydlik et al. 2007) is introduced. Appendix C is extracted from the works in Kim et al. (2022).

For 2D acoustic inversion, I choose a single cable line containing 240 receivers with an interval of 25 m from the 3D OBC data set. The preprocessed data have officially been released by Equinor and its former Volve partners since October 2018. I additionally apply a simple procedure of 3D-to-2D conversion to compensate for the amplitude and phase errors caused by 2D approximation (Crase et al. 1990). The dimension of model is 12 km x 4.5 km with a grid spacing of 25 m. 60 pressure sources were applied with an interval of 200 m at a depth of 25 m, and 240 receivers were deployed at the sea bottom ranging from 3.175 to 9.15 km of the model. Although the water depth varies from 80 to 100 m, I assume a flat sea bottom with a water depth of 100 m. Because inversion is mainly performed with low-frequency data, the depth variation is less than one grid point. The recording length is 6.4 s. For stable FWI, the zero-phase Butterworth filter with corner frequencies of 2.5 and 5.6 Hz is applied to the data.

For forward modeling, I use the same technique that was used in Appendix B. A representative shot gather and its band-pass filtered version are shown in Figs. C.1(a) and C.1(b), respectively.

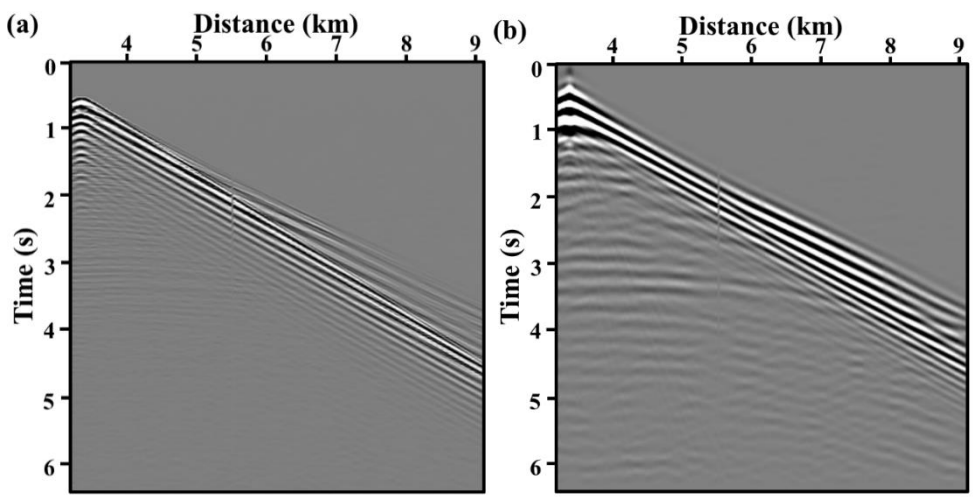

Fig. C.1. (a) A representative shot gather of the Volve OBC data set at a distance of 3.35 km and (b) its filtered version obtained by the band-pass filter ranging from 2.5 to 5.6 Hz.

For reference, I display the 3D tomography model released along with the data in Fig. C.2. The black solid lines indicate the path of the well and the yellow dashed lines indicate the 2D line extracted for acoustic inversion. For an initial velocity model, I use a linearly-increasing model as shown in Fig. C.3(a). As I did for the Marmousi-II model, I iterate the first inner loop by 10 times for each background velocity model to invert the reflectivity model. The total iteration number for the outer loop is 12. For simplicity, I use a fixed step length of 0.05 km/s for the two inner loops.

To minimize amplitude mismatches caused by inaccurate physical approximations (i.e., acoustic approximation of elastic media) and geometrical spreading effects remaining after 3D-to-2D conversion, I use the least-squares norm with trace-by-trace-normalized data (i.e., global correlation norm) as an objective function (Shen 2010; Choi and Alkhalifah 2012; Warner et al. 2013). I estimate the source wavelet by matching near-offset direct arrivals of the trace-by-trace-normalized observed and modeled data using the filter-based method (Pratt, 1999). Compared to the synthetic example, the Volve data have weak reflections as shown in Fig. C.1. Therefore, I scale the gradient with the depth-variable weighting factor (e^{2z}, where z indicates the depth) to amplify the deeper parts in the two inner loops. As addressed in the former studies, there are strong anisotropic effects at depths of $1 - 2.5$ km in the Volve oil field (Oh et al. 2018; Oh and Alkhalifah 2019; Li and Alkhalifah 2020). According to Zhang and Alkhalifah (2017) and Feng and Schuster (2019), I do not use the far-offset data to mitigate anisotropic effects. The maximum offset was adjusted from 9 km to 3 km. Then, the gradient is mainly affected by the

low-wavenumber components along the short-spread reflection wavepaths, which is relatively free from trade-off effects due to the anisotropic parameters.

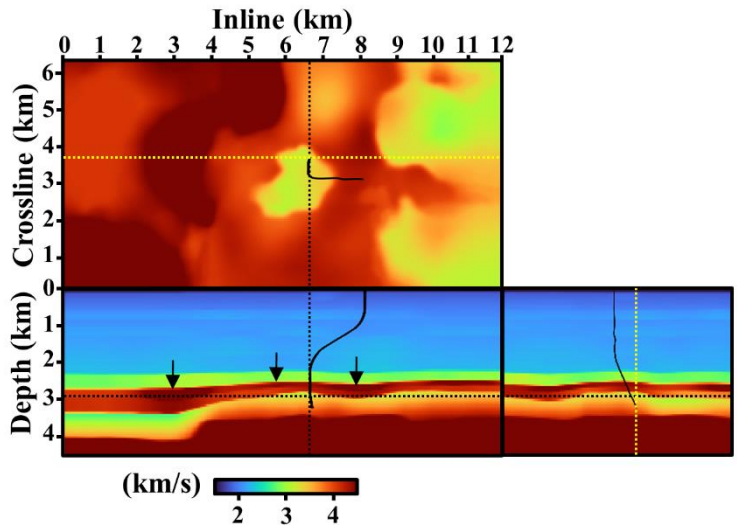

Fig. C.2. The 3D tomography P-wave velocity model released along with the Volve data. The yellow dashed lines indicate the section used for 2D acoustic FWI. The black solid lines indicate the path of the well. The black arrows indicate the top interface of the chalk layer in the tomography model.

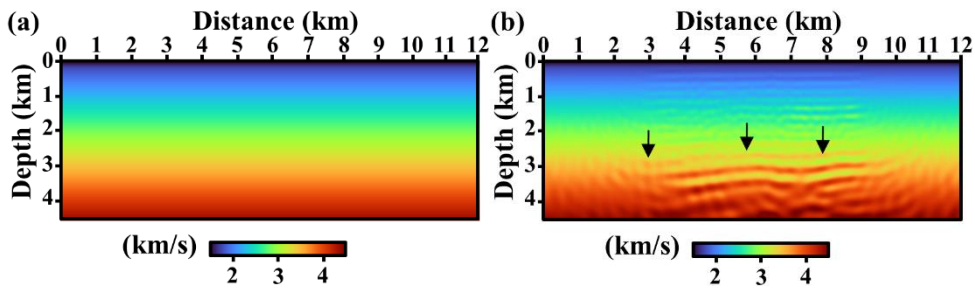

Fig. C.3. (a) The linearly-increasing background velocity model used as an initial guess and (b) the reflectivity model $\delta V_{\mathrm{p}} + V_{\mathrm{p0}}$ recovered by using near-normal-incidence reflections by mode V of diffraction-angle filtering starting from the initial background velocity model.

C.2. Inversion results

Fig. C.3(b) shows the resultant reflectivity model $\delta V_{\mathrm{p}} + V_{\mathrm{p0}}$ obtained by applying mode V after 10 iterations of the first inner loop. We observe that the horizontal chalk layer is inverted indicating the location of reservoir, as in the former studies (Szydlik et al. 2007; Guo and Alkhalifah 2017; Oh et al. 2018; Li et al. 2019). This horizontal reflector will play a role in providing the reflection wavepaths at depths of 0 – 3 km during inversion of the background velocity model in the second inner loop. The background velocity model is updated by applying mode IV to the gradient corresponding to the velocity model $\delta V_{\mathrm{p}} + V_{\mathrm{p0}}$. Figs. C.4 and C.5 show the scaled gradient and the background velocity model obtained by FWI with the nested algorithm, respectively. In Fig. C.4, the gradient contains the low-wavenumber components at depths of 1.5 – 3 km, which are carried by the first Fresnel zones associated with the pre-critical reflections. Even though I only use the near-to-intermediate-offset data, I was able to update the low-wavenumber structures at the deeper depths of 1.5 – 3 km. Fig. C.5 shows the background velocity model after 12 iterations of the outer loop, where we can also confirm that macro-structures at depths shallower than 3 km are well recovered. This low-wavenumber update will play a role in locating the chalk layer in its correct position.

I subsequently carry out conventional FWI for the Volve data using the background velocity model recovered by FWI with the nested algorithm as an initial guess. For comparison, I also perform FWI starting from the linearly-increasing initial velocity model.

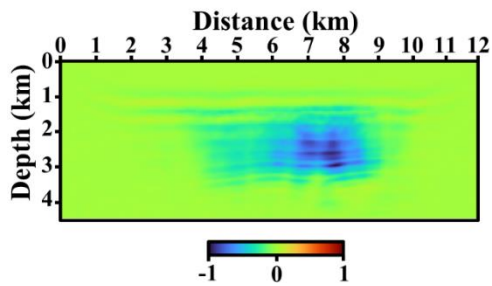

Fig. C.4. The scaled gradient obtained at the first iteration of the second inner loop of the nested algorithm.

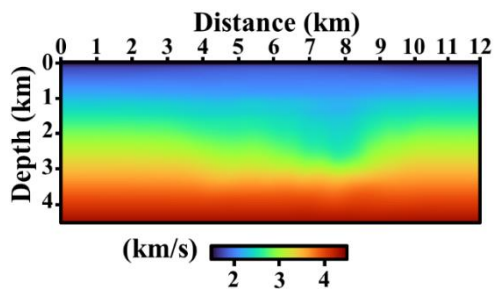

Fig. C.5. The background velocity model obtained by FWI with the nested algorithm.

Fig. C.6 shows the final inversion results and the corresponding depth profiles along the well path starting from the linearly-increasing velocity model and the background velocity model obtained by FWI with the nested algorithm. The well is oblique and deviates from the 2D line for inversion. Therefore, I project the well path along the 2D line. The prominent reflector due to horizontal chalk interface in the left panel of Fig. C.6(a) is located at depths deeper than 3 km and not focused well. In the right panel of Fig. C.6(a), I observe that the linearly-increasing velocity model (represented by the green line) is far from the well log (black) and the final inversion result starting from the linearly-increasing velocity model (red) deviates from the tendency of the well log and does not match well with the P-wave velocity contrast due to chalk interface. In contrast, the reflector in the left panel of Fig. C.6(b) is shifted to a shallower depth which is presumably its correct position (refer to the black arrows that indicates the top of the chalk layer in tomography model). In the right panel of Fig. C.6(b), we observe that the background velocity model inverted by FWI with the nested algorithm (green) has lower velocities than those of the linearly-increasing velocity model (green in Fig. C.6a). Accordingly, the final inversion result starting from the background velocity (red) matches well with the tendency of the well log compared with that starting from the linearly-increasing velocity model (red in Fig. C.6a), specifically above a depth of 2.3 km. The upper boundary of the cap rock is shifted up to some extent. Still, the locations of the cap rock and reservoir are slightly different from the well log. Considering that the depth of the chalk layer varies from 2.5 to 3 km along the inline or crossline directions, which forms a small dome-shaped structure (Szydlik et al. 2007; refer to the

reference 3D tomography model in Fig. C.2), these mismatches might be caused by the errors due to the projection of the oblique well deviated from our 2D line.

For another quality control, angle-domain common-image gathers (ADCIGs; Sava and Fomel 2003) are computed for the final FWI results starting from the linearly-increasing velocity model and the background velocity model inverted by FWI with the nested algorithm, which are displayed in Figs. C.7(a) and C.7(b), respectively. The events in Fig. C.7(b) are much flatter than those of Fig. C.7(a). As strong reflections generated by the chalk layer mainly contribute to low-wavenumber update like RWI, the events at depths of 2.5 – 3 km (in the yellow dashed box in Fig. C.7) are flattened well. However, because I mainly recovered the vertical P-wave velocity, some events at large angles still smile upward, which might be attributed to anisotropy (indicated by the red arrows). In Fig. C.8, I compare shot gathers of the trace-by-trace-normalized observed and the modeled data for the finally inverted model (e.g., Fig. C.6b). In Fig. C.8, we observe that the phases of refractions and reflections are well-matched at the near-to-intermediate offsets (shorter than 4 – 5 km). From these results, we confirm that the reconstructed P-wave velocity model reasonably describes the observed pressure data acquired in the Volve oil field.

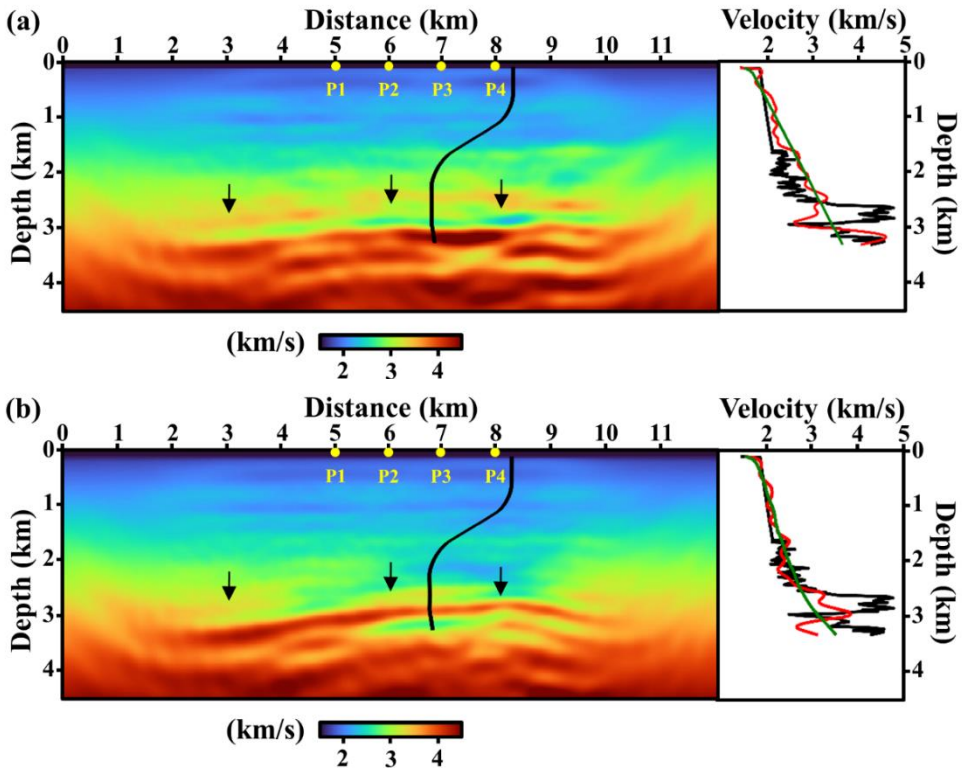

Fig. C.6. Final inversion results and depth profiles along the well path obtained by subsequent FWI starting from (a) the linearly-increasing velocity model and (b) the background velocity model obtained by FWI with the nested algorithm. In the right panels of (a) and (b), the depth profiles of starting (the green lines) and inverted velocity models (the red lines) are displayed with the well log (the black lines). The well log velocities above a depth of 1.6 km are not available and thus they are interpolated. The black lines in the left panels of (a) and (b) indicate the well path. The yellow dots indicate the locations for ADCIG in Fig. C.7.

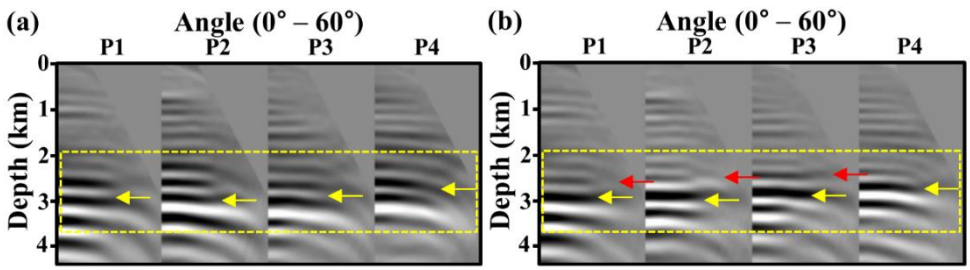

Fig. C.7. ADCIGs for the final inversion results obtained starting from (a) the linearly-increasing velocity model and (b) the background velocity model obtained by FWI with the nested algorithm. The angle ranges from 0° to 60°. Locations of P1 – P4 are shown in Fig. C.6.

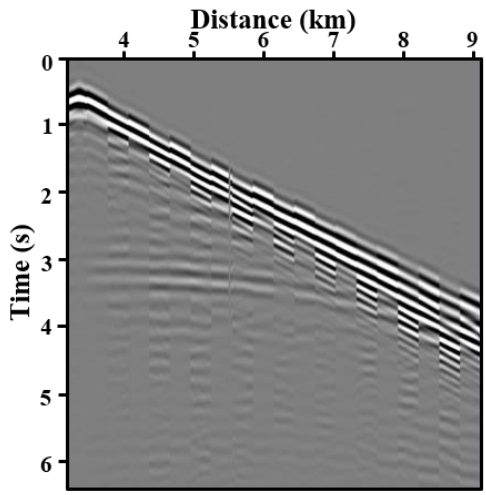

Fig. C.8. A representative shot gather at a distance of 3.35 km displayed by interweaving the trace-by-trace-normalized Volve field data with the modelled data computed for the final inversion model (shown in Fig. C.6b) every 12 traces. From left to right in the panel, the Volve field data are shown first followed by the modelled data.

초 록

회절각 필터링 기반 중첩 알고리듬을 사용한 음향파 완전파형역산: 3차원 탄성파 자료에서의 적용

김 동 건
에너지시스템공학부
서울대학교 대학원

정량적 고해상도 지하 속도구조 모델을 구축하기 위한 자료 적합 접근 방식인 완전파형역산(full waveform inversion; FWI)은 광대역/광각 탄성파 자료를 다루기 위해 널리 사용되는 수단들 중 하나가 되었다. 완전파형역산은 탄성파 자료에 포함된 전체 파동의 운동학적·동역학적 성질을 함께 고려하게 되는데, 이는 완전파형역산을 매우 비선형적으로 만들게 된다. 그러나 완전파형역산은 선형 국부 최적화 기법을 사용하기 때문에 초기 속도구조 모델이 부정확할 경우 국부 최솟값에 빠지게 된다. 완전파형역산의 비선형성 문제를 해결하기 위해서는 우선적으로 장파장 배경 속도구조 모델을 구축한 뒤, 순차적으로 단파장 반사층구조 모델을 복원하는 과정이 필요하다. 그러나 완전파형역산의 초기 단계에서 반사파에 의한 장파장 배경 속도구조의 갱신은 거의 발생하지 않으며, 반사파는 단파장 반사층구조만을 갱신하게 된다. 따라서 “완전파형역산”이라는 명칭과는 달리, 기존 완전파형역산은 주로 다이빙파에 의존하여

배경 속도구조 모델을 구축하며 반사파의 주시 정보는 역산 과정에서 거의 반영되지 않는다.

추가적으로 반사파를 활용해 초기 역산단계에서 장파장 배경 속도구조 모델을 갱신하기 위해서, 속도구조 모델을 배경 속도구조 모델과 반사층구조 모델로 분리하여 역산을 수행하는 반사파 파형역산이 제시되었다. 반사층구조 모델을 직접적으로 사용함으로써, 반사파의 파동경로를 따라 추가적으로 장파장 속도구조를 갱신할 수 있게 된다. 반사층구조 모델은 새롭게 갱신된 배경 속도구조 모델에 대해 반복적으로 구축되어야 하며, 이러한 일련의 과정을 통해 장파장 속도구조 모델과 단파장 반사층구조 모델이 번갈아가며 역산된다.

이를 큰 규모의 실제 탐사 자료에 적용하기 위해서는 속도구조 모델을 장파장 배경 속도구조 모델과 단파장 반사층구조 모델로 분리하기 위한 계산효율적인 방법이 필요하다. 또한, 배경 속도구조를 구축하는 과정에서 다이빙파와 반사파에 의한 정보가 함께 효율적으로 고려되어야 한다.

본 논문에서는 먼저 탄성파 반사법탐사에서 탄성파 자료에 포함된 다이빙파와 반사파가 완전파형역산 그래디언트의 파장 성분에 어떻게 영향을 미치는지 분석한다. 그 후, 완전파형역산 그래디언트의 파장 성분을 조절하기 위해 회절각 필터링 기법을 도입하고, 5개의 회절각 필터링 모드로 인해 다이빙파와 반사파가 그래디언트에 미치는 영향이 어떻게 변화하는지 살펴본다.

완전파형역산 그래디언트와 회절각 필터링 기법에 대한 분석을 기반으로, 다이빙파와 반사파를 함께 활용하여 신뢰할 수 있는 배경

속도구조를 구축할 수 있는 회절각 필터링 기반 중첩 알고리듬을 사용한 음향파 완전파형역산 기술을 제시하였다. 알고리듬상에서, 회절각 필터링은 반사파 파형역산과 같이 속도구조 모델을 배경 속도구조 모델과 반사층구조 모델로 분리하기 위해 사용된다. 회절각 필터링은 큰 연산량의 증가 없이 계산효율적으로 구현될 수 있으며, 3차원 탄성파 탐사 자료와 같은 큰 규모의 탐사 자료에 대해서도 알고리듬을 적용할 수 있도록 해준다. 5개의 회절각 필터링 모드 중, 모드 IV와 V가 각각 배경 속도구조 모델과 반사층구조 모델을 갱신하기 위해 사용된다. 모드 V를 통해 구축된 반사층구조 모델은 반사파 파동경로를 따라 추가적인 장파장 속도구조 갱신을 발생시킨다. 모드 IV는 직접적으로 다이빙파와 반사파의 파동경로를 따라 발생하는 장파장 완전파형역산 그래디언트 성분을 추출하여 배경 속도구조 구축에 사용할 수 있다. 개선된 장파장 속도구조 갱신 범위를 기반으로 관측 다이빙파와 반사파의 주시 정보를 더 정확히 묘사할 수 있는 배경 속도구조를 구축할 수 있다.

3차원 SEG/EAGE 오버스러스트 모델을 이용해 만든 합성 자료 및 북해 볼브(Volve) 지역의 3차원 해저케이블(ocean-bottom cable) 자료에 회절각 필터링 기반 중첩 알고리듬을 적용해봄으로써 지하구조가 매우 복잡하거나, 탄성파 자료에 탄성 및 이방성 효과가 나타나는 경우에 대해서도 알고리듬이 신뢰할 수 있는 배경 속도구조 모델을 구축할 수 있음을 보여주었다. 회절각 필터링의 모드 IV와 모드 V를 통해 성공적으로 속도구조 모델을 배경 속도구조 모델과 반사층구조 모델로 분리할 수 있음을 확인할 수 있었다. 구축된 배경 속도구조 모델은 더 정확한 고해상도 속도구조를 구축하기 위한 차후 음향파 및 탄성파

완전파형역산을 위한 초기 속도모델로 사용될 수 있을 것으로 기대된다.

주요어: 역문제 이론, 파형역산, 지진파 토모그래피, 실체파, 음향 특성, 파동 산란 및 굴절

학번: 2017-21684